MODELING OF DROPLET EVAPORATION, FLASH-BOILING, AND MIXTURE PREPARATION IN INTERNAL COMBUSTION ENGINES

BY

MIANZHI WANG

DISSERTATION

Submitted in partial fulfillment of the requirements
for the degree of Doctor of Philosophy in Mechanical Engineering
in the Graduate College of the
University of Illinois at Urbana-Champaign, 2018

Urbana, Illinois

Doctoral Committee:

Professor Chia-fon F. Lee, Chair
Professor Xinlei Wang
Professor Moshe Matalon
Professor Surya Pratap Vanka

Abstract

The evolving regulation on internal combustion engine emissions as well as the rising expectation on the engine efficiency and performance pose challenges in the development of the future engine technology. Computational methods are needed to understand the mechanism of the advanced engine combustion concepts and to facilitate the development of the future clean and efficient engine technology. This study examines numerical models essential to the simulation of mixture preparation, a vital process that determines the combustion outcome. Combustion models are also developed for compression-ignition and spark-ignition engines, and are used to simulate the advanced engine operation concepts.

In this study, a modular multi-component droplet evaporation model is developed based on the existing model by the author's lab. The updated model is capable of estimating the thermal and transport properties of real mixture of known compositions. Also added is a vapor-liquid equilibrium solver based on the fugacity coefficient of the Peng-Robinson equation of state. The modular droplet evaporation model is integrated into a customized engine CFD software, KIVA, to simulate the droplet evaporation in fuel spray.

Flash-boiling of spray generates ultra-fine fuel mist and is potentially beneficial to the mixture preparation. The author examines the existing model for the droplet flashing breakup. The existing model is reformulated and merged with the Taylor analogy breakup model, an aerodynamic droplet breakup model. The unified droplet breakup model is capable of simulating the droplet breakup under the combined effects of aerodynamic excitation and internal flashing bubble growth. Flashing spray simulations are conducted with the unified droplet breakup model.

For the compression-ignition engine operation, the chemical kinetics translates the result of mixture preparation into combustion outcome. An efficient chemical kinetics solver is developed for the chemical reaction calculation in engine CFD. The solver exploits an estimated Jacobian

matrix of the chemical kinetics problem and reduces the computational time without compromising the accuracy of the solution. Studies of various advanced compression-ignition engine concepts are conducted with the efficient chemical kinetics solver.

Spark-ignition engine simulation requires accurate flame propagation prediction. In this study, an efficient G-equation model is developed to model the flame propagation without resolving the flame structure. An advantage over the existing G-equation models is the addition of a knock prediction method inspired by the Livengood-Wu integral. The combination of the G-equation model and the spontaneous ignition calculation results in an unified combustion model for the simulation of spark-ignition engine operation with end-gas ignition, *a.k.a.*, knocking. The model is tested by simulating the operation of a swirl-dominant gasoline direct-injection engine.

As the concluding remark, this study develops not only mixture preparation models that predict the mixture preparation outcome, but also combustion models that assess the combustion's dependency on the mixture preparation. CFD simulations demonstrate the usefulness of these models in the discovery of the future engine technologies.

Acknowledgments

This dissertation is the result of efforts made by many people. First and foremost, I would like to thank my advisor Professor Chia-Fon Lee for the opportunity to be a member of your team. Your inspirational mentorship as well as the diverse project experiences provided by your lab have transformed me into a capable engine researcher. I would like to thank Professor Moshe Matalon, Professor Surya Pratap Vanka, and Professor Xinlei Wang for being my doctoral committee members. Your invaluable feedbacks and fresh opinions made it possible for me to reexamine my work in a different angle and gain deeper understanding of the subjects.

I am grateful to the students and visiting scholars in Professor Lee's engine lab. Dr. Cai Shen, Dr. Juncheng Li, Dr. Ming Huo, Dr. Nan Zhou, and Guo Li helped me transiting smoothly into the work and life at UIUC. The research would not be complete without the experimental results provided by Dr. Karthik Nithyanandan, Professor Han Wu, Yilu Lin, Xiangyu Meng, Dr. Yuqiang Li, Dr. Jiaxiang Zhang, Timothy Lee, Bob Donahue, Yuanxu Li, and Junhao Yan. Dr. Zhichao Zhao, Zhengxin Xu, and Menghan Li helped me numerous times with the KIVA grids of complex geometries, as well as the reaction mechanisms. I appreciate the valuable discussions with Saifei Zhang, Professor Hong Liu, Professor Ying Wang, Professor Zhaolei Zheng, Jie Hou, Peng Yin, Deng Li, Yu Li, Suya Gao, Haiqin Zhou, Gang Li, and Nana Wang. Thanks to Dr. Wayne Chang who organizes the research projects and keeps the team at its best productivity.

I would like to thank the National Science Foundation, the Department of Energy, and the FAW Group Corporation for the financial sponsorship of the diverse research projects in our lab. These projects gave me exposure to engine studies over a wide spectra, from fundamental discoveries to practical developments.

The study could not be finished within the short five years of the Ph.D. program without the open-source software ecosystem and communities. CANTERA, SUNDIALS, UMFPACK, Lapack,

etc. provided high-quality building blocks and enabled the programs developed in this study to enjoy the latest and greatest numerical techniques.

The accomplishments described in this dissertation are also based on my experiences obtained during my Master degree with Professor Nikolaos Gatsonis at Worcester Polytechnic Institute. Without those experiences, it would be impossible for me to have the idea which leaded to the efficient chemical kinetics solver introduced in Chap. 4.

My deepest gratitude is for my wife Dr. Yi Ren, my parents, my grand parents, and my in-laws. Your profound and endless love empowers me to take every challenge in the research and my life.

Table of Contents

List of Tables . . . . . **viii**

List of Figures . . . . . **ix**

List of Abbreviations . . . . . **xiv**

List of Symbols . . . . . **xvii**

Chapter 1 Introduction **1**
1.1 Motivations 1
1.2 Mixture Preparation in CI Engine 2
1.3 Mixture Preparation in SI Engine 4
1.4 Modeling of Multi-Component Droplet Evaporation and Flash-Boiling 5
1.5 A Brief Introduction to KIVA 6
1.6 Scope of the Present Study 7

Chapter 2 Modeling of Droplet Evaporation **12**
2.1 Thermal and Transport Properties of Fluid 12
2.2 VLE Computation 17
2.3 Droplet Evaporation Model 20
2.4 The Spray G Simulation 29

Chapter 3 Modeling of Droplet Flash-Boiling **34**
3.1 Combined Model for Flashing and Aerodynamic Droplet Breakup 35
3.2 Single Droplet Breakup 40
3.3 Flashing Spray Simulation 42
3.3.1 Flashing and Non-Flashing N-Heptane Spray 42

Chapter 4 CI Engine Simulation and Chemical Kinetics **55**
4.1 Efficient Chemical Kinetics Solver 55
4.2 Simulation of Diesel Engine Operation 61
4.3 Single Injection Ignition Phase Curve and Combustion Regimes 63
4.3.1 Overview of the Ignition Phase Curve 65
4.3.2 Effects of Combustion Chamber Geometry 66
4.3.3 Effects of Temperature 71
4.3.4 Effects of Engine Load and Overall Equivalence Ratio 72
4.4 Gasoline Direct-Injection Compression-Ignition Engine 78
4.4.1 Simulation Conditions 80

4.4.2 Effects of Fuel, Boost, Compression Ratio, and Temperature 82
4.4.3 Over-mixing and PPC Operation 86
4.4.4 Emission Dependency: ϕ, T, Dilution, and Beyond 89
4.5 Diesel - Natural Gas Dual Fuel Engine 96
4.5.1 Validation of the Simulation Work-Flow 97
4.5.2 Stoichiometric Dual Fuel Mixture Preparation 98
4.5.3 Stoichiometric Dual Fuel Operation and Limitations 101

Chapter 5 SI Engine Simulation and Flame Propagation Model 111
5.1 G-Equation Model with Knock Prediction Capability 112
5.2 Premixed Flame Propagation in a Constant Volume Chamber 117
5.3 Swirl-Dominant GDI Engine 120

Chapter 6 Summary and Future Works 125
6.1 Model Development 125
6.2 CI Engine Study and Innovation 127

References 130

Appendix A Mixture Viscosity and Thermal Conductivity 139

Appendix B Mixture-Averaged Diffusivity 143

List of Tables

2.1 The conditions of the standard Spray G experiment and its simulation. 29

4.1 Initial values of temperature, pressure, and equivalence ratio resulting in twelve combinations. 60
4.2 Details about the selected mechanisms. 60
4.3 Key parameters of the AVL 5402 single cylinder test engine. 62
4.4 The overall equivalence ratio of each tested fuel quantity. 72
4.5 Tested cases and description. 82
4.6 Engine-out emissions for each case. 89

5.1 Key parameters of the single cylinder swirl-dominant GDI test engine. 120

A.1 Constants in Eq. A.8 for viscosity. 140
A.2 Constants in Eq. A.8 for thermal conductivity. 142

List of Figures

1.1 The fundamental processes addressed and the computational models developed in the present study. . . . 8
1.2 The framework of the CFD program with the custom droplet evaporation model. The highlighted parts include the contribution of the present study. . . . 9
1.3 The framework of the CFD program with the combined aerodynamic/flashing breakup model. The highlighted parts include the contribution of the present study. . . . 9
1.4 The framework of the CFD program with the efficient chemical kinetics solver. The highlighted parts include the contribution of the present study. . . . 10
1.5 The framework of the CFD program with the unified flame propagation and spontaneous ignition model. The highlighted parts include the contribution of the present study. . . . 11

2.1 The modeled enthalpy of n-hexane and the data from NIST database [56]. The blue and red color represents 1 bar and 4 bar ambient pressure, respectively. . . . 14
2.2 The modeled viscosity of binary liquid systems of n-hexane/n-heptane/n-octane, and measured data [18]. . . . 14
2.3 The modeled viscosity of binary gas systems of nitrogen/methane, and measured data [26]. . . . 15
2.4 The modeled thermal conductivity of binary liquid systems of n-heptane/isooctane, and measured data [28]. . . . 15
2.5 The modeled thermal conductivity of binary gas systems of methane/propane, and measured data [93]. . . . 16
2.6 The modeled mixture-averaged diffusion coefficient of n-heptane in liquid and gas binary systems of n-heptane/nitrogen, compared with measured data [65] and molecular dynamics simulation [7]. . . . 17
2.7 The VLE calculation of binary systems of n-hexane/n-heptane, and measured data [38]. . . . 19
2.8 The VLE calculation of ternary systems of n-hexane/cyclohexane/n-heptane, and measured data [38]. . . . 19
2.9 The VLE calculation of binary systems of propane/carbon-dioxide, and measured data [82]. . . . 20
2.10 The temperature distribution in a slowly evaporating droplet. . . . 24
2.11 The temperature distribution in a rapidly evaporating droplet. . . . 24
2.12 The calculated evaporation rate of n-heptane droplet and data from suspended droplet experiments [9, 69, 30] and from model in literature [113]. . . . 25

2.13 The calculated evaporation progress of isooctane droplet and data from float droplet experiment [12]. 26
2.14 The calculated evaporation progress of n-heptane droplet under high pressure and data from suspended droplet experiment [69]. 26
2.15 The calculated evaporation rate of isooctane droplet and an empirical correlation [81]. 27
2.16 The molar fraction of the more volatile species in the droplet at different stage of the evaporation process [80]. 28
2.17 A schematic drawing of the standard Spray G experiment, the configuration of the present simulation of the Spray G (left), and the $\frac{1}{8}$ sector grid (right). 30
2.18 The visualization of the liquid phase (Lagrangian parcels) and the fuel vapor distribution (volume rendering of the gas phase fuel mass fraction) of the Spray G. 32
2.19 The vertical liquid and vapor penetration of the Spray G [27]. 33
2.20 The comparison of the Spray G fuel mass fraction distribution between the present simulation and the LES study by Argonne National Lab [37]. 33

3.1 The aerodynamic breakup and flashing breakup of liquid jet. 35
3.2 The density of nucleation sites upon pressure drop. 36
3.3 The calculated water bubble growth history and measured data [55]. 38
3.4 A schematic picture of a deformed droplet in the TAB model. 39
3.5 The droplet deformation $\hat{x}$ upon aerodynamic load of different Weber numbers. . . . 40
3.6 The TAB and flashing breakup time of superheated water droplet. 41
3.7 The perpendicular secondary droplet velocity normalized by the original droplet velocity, *a.k.a.* the tangent of the spray half cone angle, of the TAB and flashing breakup. 41
3.8 The SMR of the secondary droplet normalized by the original droplet upon TAB and flashing breakup. 42
3.9 The Lagrangian parcels and the fuel mass fraction in a non-flashing hollow-cone spray 2-D simulation (top row), and the synthetic droplet light blockage images (middle row). For comparison are the high speed images in the same scale [112] (bottom row). 44
3.10 The Lagrangian parcels and the fuel mass fraction in a flashing hollow-cone spray 2-D simulation (top row), and the synthetic droplet light blockage images (middle row). For comparison are the high speed images in the same scale [112] (bottom row). 45
3.11 The Lagrangian parcels and the fuel mass fraction in hollow-cone spray 2-D simulations (top row), and the synthetic droplet light blockage images (middle row). For comparison are the high speed images in the same scale [112] (bottom row). The snapshot for different liquid temperatures are taken at 0.5 ms after SOI. 49
3.12 The Lagrangian parcels and the fuel mass fraction in hollow-cone spray 2-D simulations (top row), and the synthetic droplet light blockage images (middle row). For comparison are the high speed images in the same scale [112] (bottom row). The snapshot for different liquid temperatures are taken at 1.0 ms after SOI. 50
3.13 The Lagrangian parcels and the fuel mass fraction in hollow-cone spray 2-D simulations (top row), and the synthetic droplet light blockage images (middle row). For comparison are the high speed images in the same scale [112] (bottom row). The snapshot for different liquid temperatures are taken at 1.5 ms after SOI. 51

3.14 The Lagrangian parcels and the fuel mass fraction in hollow-cone spray 2-D simulations (top row), and the synthetic droplet light blockage images (middle row). For comparison are the high speed images in the same scale [112] (bottom row). The snapshot for different liquid temperatures are taken at 2.0 ms after SOI. 52
3.15 The Lagrangian parcels and the fuel mass fraction in hollow-cone spray 2-D simulations (top row), and the synthetic droplet light blockage images (middle row). For comparison are the high speed images in the same scale [112] (bottom row). The snapshot for different liquid temperatures are taken at 2.5 ms after SOI. 53
3.16 The Lagrangian parcels and the fuel mass fraction in hollow-cone spray 2-D simulations (top row), and the synthetic droplet light blockage images (middle row). For comparison are the high speed images in the same scale [112] (bottom row). The snapshot for different liquid temperatures are taken at 3.0 ms after SOI. 54

4.1 Average CPU times for direct dense method with semi-analytical Jacobian formulation, preconditioned Krylov method, and CANTERA to simulate all selected mechanisms [106]. 61
4.2 Comparison between predicted and measured pressure trace under different engine loads. 62
4.3 Comparison between predicted and measured pressure trace with different SOI timings. 62
4.4 A schematic plot of ignition phase curve [108]. 64
4.5 An example of $T - \phi$ distribution plot through the combustion process. 65
4.6 The baseline (high temperature) ignition phase curve and the onset of cool flame [108]. 66
4.7 The equivalence ratio distribution at 4° after SOI (SOI is at 330°) [108]. The stock and simplified piston geometry are compared with each other. 67
4.8 The baseline ignition phase curve and deviations via altering the piston and injector geometry [108]. 67
4.9 The equivalence ratio distribution of two baseline cases at 346° (before the onset of cool flame) [108]. 68
4.10 Evolution of the fuel mass fraction distribution in the baseline case with SOI = 328° [108]. 69
4.11 Evolution of the temperature distribution in the baseline case with SOI = 328° [108]. 70
4.12 In bowl and out of bowl $T - \phi$ snapshot of the baseline case with SOI = 328° AT CA = 346° [108]. 70
4.13 The ignition phase curve with different IVC temperatures [108]. 72
4.14 CA50 vs SOI timing under different loads. 73
4.15 The volume rendering of the equivalence ratio at 340° crank angle with two different SOI timings, 312° and 318°. Both cases have the fuel quantity of 16 mg per cycle. . 74
4.16 Snapshot of the mixture mass fraction distribution in the ϕ-space at 340° crank angle at the load of 4 mg per cycle. 75
4.17 Snapshot of the mixture mass fraction distribution in the ϕ-space at 340° crank angle at the load of 10 mg per cycle. 75
4.18 CA10, CA50, and CA90 vs SOI timing under the load of 4 mg per cycle. 77
4.19 CA10, CA50, and CA90 vs SOI timing under the load of 10 mg per cycle. 77
4.20 The combustion efficiency at load of 4, 10, and 16 mg per cycle. 78
4.21 Comparison between the geometry of the stock AVL 5402 and the geometry of the derived engine. 81

4.22 CA10, CA50, and CA90 timings of the diesel-fueled operation and the baseline GDCI operation. . . . 84
4.23 CA10, CA50, and CA90 timings of the baseline GDCI operation and the p_{IVC} = 1.5bar case. . . . 84
4.24 CA10, CA50, and CA90 timings of the baseline GDCI operation and the 18.0 compression cases with 20 and 10 mg fuel. . . . 85
4.25 CA10, CA50, and CA90 timings of the baseline GDCI operation, the case with 15% warm EGR, and the case with heated intake that has the same T_{IVC} as the 15% EGR case. . . . 85
4.26 CA10 timing and the maximum local equivalence ratio at CA10 of the baseline GDCI operation. . . . 87
4.27 CA10 timing and the maximum local equivalence ratio at CA10 of the high compression ratio GDCI operation with 20 and 10 mg fuel. . . . 88
4.28 CA10 timing and the maximum local equivalence ratio at CA10 of the high IVC temperature GDCI operation with 20 and 10 mg fuel. . . . 88
4.29 ϕ-sensitivity of the PRF85-air mixture ignition under two representative initial conditions. . . . 89
4.30 Selected SOIs targeting CA50 = 370°, and the pressure traces for different cases. . . . 91
4.31 Snapshot of the baseline NO_x, CO emissions, and mixture distribution after combustion. . . . 92
4.32 Snapshot of the boosted case NO_x, CO emissions, and mixture distribution after combustion. . . . 92
4.33 Snapshot of the high C.R. case NO_x, CO emissions, and mixture distribution after combustion. . . . 93
4.34 Snapshot of the warm EGR case NO_x, CO emissions, and mixture distribution after combustion. . . . 93
4.35 Snapshot of the heated case NO_x, CO emissions, and mixture distribution after combustion. . . . 94
4.36 the evolution of the $\phi = 0.8$ iso-surface in the high compression ratio case with selected SOI. . . . 95
4.37 The comparison between calculated and measured cylinder pressure with different NG substitution ratios. . . . 98
4.38 The comparison between calculated and measured cylinder pressure with different SOI timings. . . . 98
4.39 The CA10, CA50, and CA90 as functions of SOI at different operation conditions. . . . 100
4.40 The selected SOI timing at different operation conditions. . . . 101
4.41 The snapshot of temperature, equivalent ratio, NO mass fraction, and CO mass fraction at crank angle of 347°. The operation condition is 1200 rpm and with 25 mg equivalent diesel. . . . 102
4.42 The snapshot of temperature, equivalent ratio, NO mass fraction, and CO mass fraction at crank angle of 360°. The operation condition is 1200 rpm and with 25 mg equivalent diesel. . . . 102
4.43 The snapshot of temperature, equivalent ratio, NO mass fraction, and CO mass fraction at crank angle of 365°. The operation condition is 1200 rpm and with 25 mg equivalent diesel. . . . 103

4.44 The snapshot of temperature, equivalent ratio, NO mass fraction, and CO mass fraction at crank angle of 370°. The operation condition is 1200 rpm and with 25 mg equivalent diesel. 103
4.45 The snapshot of temperature, equivalent ratio, NO mass fraction, and CO mass fraction at crank angle of 380°. The operation condition is 1200 rpm and with 25 mg equivalent diesel. 104
4.46 The indicated work from IVC to EVO at different operation conditions. 105
4.47 The indicated specific fuel consumption at different operation conditions. 105
4.48 The engine-out NO_x emission at different operation conditions. 106
4.49 The required TWC's NO_x conversion efficiency such that the tailpipe NO_x emission is 0.4 g/kwh. 106
4.50 The engine-out CO emission at different operation conditions. 107
4.51 The required TWC's CO conversion efficiency such that the tailpipe CO emission is 1 g/kwh. 108
4.52 The PPRR at different operation conditions. 109
4.53 The blow-down exhaust temperature at different operation conditions. 110
4.54 The thermal load at different operation conditions. 110

5.1 The computational grid of the constant volume chamber and the location of the spark plug. 118
5.2 The predicted and measured pressure variation in the constant volume chamber during acetylene SI combustion event. 119
5.3 The predicted temperature on the cross sections and the $G = 0$ iso-surface during acetylene SI combustion event. 119
5.4 The computational grid of the tested GDI engine, looking from the top and the bottom. 121
5.5 The ignition delay data of PRF95 visualized at a constant pressure of 20 bar. 122
5.6 The ignition delay data of PRF95 visualized at a constant pressure of 40 bar. 123
5.7 The predicted (with PRF95) and measured pressure trace of the tested GDI engine. 124
5.8 The $G = 0$ iso-surface and the volume rendering of H during the operation of the tested GDI engine with reference fuels of different octane ratings. 124

List of Abbreviations

AKI	anti-knock index
ALE	arbitrary Lagrangian-Eulerian
ANL	Argonne National Laboratory
BDF	backward differentiation formulas
BTDC	before top dead center
CA	crank angle
CFD	computational fluid dynamics
CI	compression-ignition
DI	direct-injection
DIATA	direct-injection, aluminum, through-bolt assembly
DICI	direct-injection compression-ignition
DPI	diesel pilot ignition
ECU	engine control unit
EGR	exhaust gas recirculation
ECN	Engine Combustion Network
EOS	equation of state
EPA	United States Environmental Protection Agency
EVO	exhaust valve opening
FVM	finite volume method
GDCI	gasoline direct-injection compression-ignition
GDI	gasoline direct-injection
GMRES	generalized minimal residual

GSA	global sensitivity analysis
HCCI	homogeneous charge compression-ignition
ILDM	intrinsic lower-dimensional manifold
IMEP	indicated mean effective pressure
ISFC	indicated specific fuel consumption
IVC	intake valve closing
LES	large eddy simulation
LIVC	late intake valve closing
LNT	lean NO_x trap
LTC	low temperature combustion
MON	motor octane number
NASA	National Aeronautics and Space Administration
NG	natural gas
NIST	National Institute of Standards and Technology
ODE	ordinary differential equation
PCCI	partially premixed charge compression ignition
PFI	port fuel injection
PPC	partially premixed combustion
PPRR	peak pressure rising rate
PR	Peng-Robinson
PRR	pressure rising rate
PRF	primary reference fuel
RCCI	reactivity-controlled compression-ignition
RHS	right hand side
RON	research octane number
SCR	selective catalytic reduction
SI	spark-ignition
SMR	Sauter mean radius
SOC	start of combustion

SOI	start of injection
TAB	Taylor analogy breakup
TDC	top dead center
TRF	toluene reference fuel
TWC	three-way catalytic converter
VLE	vapor-liquid equilibrium

List of Symbols

B_i	transfer number of species i
c_p, c_v	mass based constant pressure and constant volume heat capacity
D_i	mixture-averaged diffusivity of species i
E	factor of surface-mean difference due to non-zero Péclet number; energy of the bubble-droplet system
f_i	fugacity of species i
G	the scalar field that tracks the flame front in the unified combustion model
H	the scalar field that tracks spontaneous ignition in the unified combustion model
$\hat{h}$	molar based specific enthalpy of real fluid
$\hat{h}_{ig}$	molar based specific enthalpy at ideal gas limit
$\mathbf{J}$	Jacobian matrix of the chemical kinetics problem
Ja	Jakob number
K	droplet surface area reduction rate; total droplet oscillation energy over that of the primary oscillation mode
k	thermal conductivity
$\tilde{M}_i$	molar mass of species i
N_b	number density of bubble nucleation sites
Nu	Nusselt number
$\mathbf{P}$	preconditioning matrix
p	pressure
p_v	vapor pressure
Pe	Péclet number
Pr	Prandtl number

R	radius of droplet
R_{32}	Sauter mean radius of droplets
$\hat{R}$	molar based ideal gas constant
Re	Reynolds number
Sc_i	Schmidt number of species i
Sh_i	Sherwood number of species i
T	temperature
ΔT	superheat
u	droplet speed relative to the gas
u_i	mass based specific internal energy of species i
$\hat{v}$	molar based specific volume
$v_\perp$	secondary droplet speed perpendicular to u
We	droplet Weber number
x	droplet deformation in the TAB model
X_i	molar fraction of species i
Y_i	mass fraction of species i
Γ	flux
ϵ	bubble void fraction of droplet
ϵ_i	mass fraction of species i in the evaporating mixture
μ	dynamic viscosity
ρ	density
σ	surface tension
ϕ	equivalence ratio
ϕ_i	fugacity coefficient of species i

Subscripts and superscripts:

$(\cdot)_0$	initial value of $(\cdot)$
$(\cdot)_b$	$(\cdot)$ of bubble

$(\cdot)_c$	$(\cdot)$ of the critical state
$(\cdot)^e$	effective value of $(\cdot)$ due to droplet internal circulation
$(\cdot)_g$	$(\cdot)$ of gas
$(\cdot)_i$	$(\cdot)$ of species i; $(\cdot)$ at the bubble-liquid interface; $(\cdot)$ at the flame inner layer
$(\cdot)_l$	$(\cdot)$ of liquid
$(\cdot)_o$	$(\cdot)$ of the outer surface of the bubble-droplet system
$(\cdot)_s$	$(\cdot)$ at surface
$(\cdot)_\infty$	$(\cdot)$ far out of the boundary layer
$\hat{(\cdot)}$	molar based value of $(\cdot)$; normalized value of $(\cdot)$
$\bar{(\cdot)}$	averaged value of $(\cdot)$ by the "$\frac{1}{3}$" rule

Chapter 1

Introduction

1.1 Motivations

Internal combustion engine has been and will be, in the foreseeable future, used as the major power production device in ground transportation activities. With modern society's heavy dependency on ground transportation, internal combustion engine's high energy consumption and negative environmental impact have become major issues. Development of efficient and environmentally-friendly internal combustion engine is among the most important tasks in the pursuit of sustainable prosperity.

The increasing awareness and concern about the environmental impact from internal combustion engine applications have resulted in stringent emission regulations. The current EPA Tier-4 and Euro-VI regulations demand exponential reduction of engine emissions compared to the previous series of regulations. Such reduction of emissions is achievable with current technology, but at the cost of serious reduction of fuel efficiency and significant increase in system complexity. The automotive industry is in desperate need of revolutionary improvements in engine technology to be propelled out of the efficiency-cleanness dilemma.

Mixture preparation is a key subject in such revolutionary improvements of internal combustion engine. In both compression-ignition (CI) and spark-ignition (SI) engines, the method and strategy of mixture preparation determine the state of fuel-air mixture before combustion. The ignition, fuel conversion, pollutant formation, and other processes in the combustion event are significantly affected by the mixture preparation and subsequent state of the fuel-air mixture. In CI engine combustion, the chemical kinetics that leads to the ignition is among the most influential elements that determine the outcome of the combustion event. The effectiveness and speed of ignition is strongly affected by the local fuel concentration and temperature. In SI engine combustion, the

flame propagation and pollutant emission are directly affected by the distribution of fuel vapor in the combustion chamber, which makes the mixture preparation one of the most important topics in the development of efficient, smooth, and clean SI engines.

In this research, the effects of mixture preparation on both chemical kinetics and flame propagation are studied in detail using computational methods. The evaporation of fuel droplets, one of the most important processes in mixture preparation, is analyzed and modeled numerically. Flash-boiling of the spray, a potentially effective method to improve mixture preparation, is also examined. The presented work not only helps with the understanding of the fundamental physical and chemical processes during mixture preparation and combustion, but also provides practical and efficient computational methods for the discovery of future revolutionary engine technology as well as the development of future engine product.

1.2 Mixture Preparation in CI Engine

In the conventional CI engine combustion, the duration of mixture preparation is short (often less than 1 ms between fuel injection and ignition). During engine operation, a chemically-reactive fuel, *i.e.* diesel, is injected directly into the combustion chamber at a timing when the piston is very close to the top dead center (TDC). The fuel spray is quickly atomized due to its high Weber number, and is evaporated into fuel vapor, which mixes with the surrounding air. The layer of fuel-air mixture surrounding the spray is exposed to a high temperature (*i.e.* 800–1200 K) high pressure (*i.e.* 40–120 bar) environment, and ignites spontaneously after a short induction time, determined by the chemical kinetics. In the case that the fuel injection continues after ignition, the structure of spray combustion is formed [22]. In spray combustion, a rich premixed combustion region, upstream of which the fresh air entrains the atomizing spray, exists close to the injector nozzle. A bag-shaped diffusion flame is formed downstream of the rich premixed combustion region, separating the fuel vapor from the surrounding air, and heating the gases. Despite of the short duration of mixture preparation in conventional CI engine, great efforts have been made to improve the engine operation smoothness by applying a pilot fuel injection to tune the mixture environment for the combustion of the main fuel spray [85, 6].

In the discovery and development of advanced CI engine combustion, varying the mixture

preparation strategy is the main approach to achieve the desired combustion outcome. Wang *et al.* [108] studied numerically the interaction between fuel-air mixing and chemical kinetics. In the study, it was demonstrated that conventional direct injection compression ignition (DICI) combustion, and partially premixed combustion (PPC) [43] can be achieved by simply adjusting the start of injection (SOI) timing of the single fuel injection event. In engine operation with PPC, the first fuel injection event has an advanced timing, such that the gas temperature and pressure is still low at the moment of injection. The ignition delay is elongated to provide more time for the mixture preparation process. With the fuel vapor more evenly distributed in the combustion chamber, the fuel-rich spots responsible for the soot emission are eliminated. With the piston traveling near the TDC, the fuel-air mixture is ignited by either another fuel injection, or the incremental heat release from the first injection. Apart from the tuning of the injection timing, the PPC concept is often accompanied by the use of exhaust gas recirculation (EGR) [71], which is another approach to alter the mixture state in engine. By diluting the mixture with EGR gas, not only is the mixture preparation time extended, the combustion temperature is also reduced to suppress the formation of nitrogen oxides (NO_x) and soot.

The introduction of a second fuel (often more volatile but less reactive than diesel, *e.g.* natural gas, gasoline, *etc.*) expands the possibility of mixture preparation for CI engine operation. In a dual fuel CI engine, the high-volatility fuel is introduced into the combustion chamber prior to the high-reactivity fuel. Either intake manifold induction/injection or early direct fuel injection is used to produce the mixture of high-volatility fuel and fresh air. Then the high-reactivity fuel is injected directly into the combustion chamber, generating distributed ignition kernels that initiate the deflagration through the premixed flammable mixture. Depending on the local equivalence ratio of the ignition kernel before ignition, the ignition is classified as either reactivity-controlled compression-ignition (RCCI) [46] or conventional diesel pilot ignition (DPI) [41]. In RCCI combustion, the SOI of the high-reactivity fuel is long before TDC, and the ignition timing is inversely related to the SOI due to the over-mixing effect. In DPI combustion, the high-reactivity fuel is injected near TDC, and the ignition timing is positively controlled by the SOI. Wang *et al.* [107] used 0-D computation to study the chemical effects of natural gas on diesel ignition. They also conducted 3-D CFD-based optimization to find the best control strategy for a given operation

condition.

1.3 Mixture Preparation in SI Engine

Modern SI engines have three major fuel injection/induction strategies: throttle body injection/induction, port fuel injection (PFI), and direct injection (DI).

In both throttle body injection/induction and PFI, the fuel is injected/inducted upstream of the combustion chamber, and is mixed with air before entering the combustion chamber. Often, it is likely to have homogeneous mixture at the moment of spark discharge, unless there were injection system malfunctions or design defects in the flow system. The equivalence ratio of the mixture is precisely controlled in the vicinity of 1.0 in common SI engines. In the case that the homogeneous mixture is richer than stoichiometry, CO emission is expected due to insufficient oxygen supply. When the homogeneous mixture is leaner than stoichiometry, the residual oxygen in the exhaust gas deteriorates the NO_x conversion of the three-way catalytic converter (TWC). In practice, the equivalence ratio of the mixture is periodically "dithered" by a small magnitude from stoichiometry even at steady engine operation condition in order to stretch the TWC's equivalence ratio window for effective conversion of hydrocarbon (HC), CO, and NO_x emissions [24].

For the DI method of mixture preparation, two major strategies exist. One strategy is to inject the fuel during the intake stroke to produce homogeneous mixture as seen in the setup with throttle body injection and PFI system. Efforts have been made to enhance the mixing by tuning intake flow [33] and injection timing [34]. Unfortunately the mixture prepared by the DI method still cannot be as homogeneous as the mixture prepared by the other two methods. The existence of the locally rich region during combustion is responsible for the higher engine-out CO and soot emissions from SI engines with DI system. The other strategy is to inject the fuel during the compression stroke to intentionally produce inhomogeneous mixture, *a.k.a.* stratified charge. Zeng and Lee [115] demonstrated numerically the capability of such strategy to generate stratified charge being near stoichiometric around the spark plug and ultra-lean in the outer region. However, the excessive oxygen in the exhaust deteriorates the TWC's NO_x conversion. For this reason, the stratified charge lean-burn strategy is often accompanied by the use of EGR to suppress NO_x generation [88]. Detailed study on the trade-off between fast flame propagation and low NO_x formation is in

urgent need but is rare in the literature. Another issue with DI mixture preparation method is the wall wetting in the combustion chamber and the subsequent high HC emission [10]. In order to address these issues with the DI mixture preparation in SI engine, further research on spray atomization, fuel evaporation, and turbulent transport is needed.

1.4 Modeling of Multi-Component Droplet Evaporation and Flash-Boiling

The outcome of mixture preparation is determined by the process of spray atomization, liquid fuel evaporation, and turbulent transport. The spray atomization consists of the breakup of the continuous liquid jet and the breakup of the discrete droplets. Under non-flashing environment, the interaction between the aerodynamic force and the surface tension is the primary mechanism that breaks up the liquid jet [83], the liquid sheet [92], and the liquid droplets [72, 4]. In the case that the liquid is superheated upon injection, the breakup is enhanced by the growth of vapor bubbles inside the liquid jet and the droplet. The spray undergoes evaporation process as soon as the liquid is injected into the ambient environment. The liquid surface releases vapor into the gas so that vapor-liquid equilibrium (VLE) is achieved at the phase interface. The fuel vapor near the interface is then transported away from the interface due to the vapor's concentration gradient in the surrounding medium. In spite of the depletion effect of the gas phase transport, the liquid keeps releasing vapor, maintaining VLE at the phase interface.

Due to the interest in using flash-boiling to enhance atomization in internal combustion engine, efforts have been made to include the flash-boiling effect into CFD simulation with Lagrangian liquid phase representation. Kawano *et al.* [42] developed a flash-boiling model for the KIVA-3V program based on the earlier work of Senda *et al.* [91]. In the model, computation of bubble nucleation, bubble growth, and droplet flashing breakup were added to the KIVA-3V program to simulate the flash-boiling of superheated spray. Zeng and Lee [117] developed a similar model, but included a more detailed analysis for the bubble growth and breakup process. The bubble growth was predicted by coupling the Rayleigh-Plesset Equation with 1-D-resolved heat transfer in the liquid phase. An energy-based secondary droplet model and a stability-analysis-based breakup

criterion were developed to improve the prediction of breakup time and outcome. Chang and Lee [8] improved the computation efficiency of the flash-boiling model [117] by replacing the finite volume method (FVM) solution of the liquid phase heat transfer with an approximate transient boundary layer thickness and a polynomial temperature profile. However, the integration of the Rayleigh-Plesset equation, which is stiff for the thermal-diffusion-controlled bubble growth, still poses challenge for the application of flash-boiling models in engine CFD simulation.

A multi-component droplet evaporation model calculates the energy and species transport in the liquid and the gas phase, as well as the VLE at the phase interface. To resolve the internal circulation in the liquid phase, it requires at least 2-D (axial-symmetric) description of the droplet [1]. However, in order to keep the computational cost manageable, it is common to use 1-D (spherical-symmetric) model in CFD with Lagrangian droplets. The concept of equivalent diffusivity was introduced to account for the internal circulation in the liquid phase [1]. Zeng and Lee [118] further simplified the 1-D problem by constructing a quasi 1-D model in which the differences between the droplet surface state and the mean droplet state are modeled. The quasi 1-D model shows satisfying accuracy compared to the 1-D model, while significantly reduces the computational cost.

1.5 A Brief Introduction to KIVA

In this work, a customized version of the KIVA-3V Release 2 [2] software is used as the CFD platform. KIVA is a source-available CFD software specifically designed for internal combustion engine applications. KIVA applies an Arbitrary Lagrangian-Eulerian (ALE) method to solve the compressible Navier-Stokes Equations. The ALE method is in the category of segregated pressure-based solvers. KIVA-3V uses FVM upon block-structured, staggered grid, where momentum conservation is enforced in the nodal control volumes, and other states are solved in the cell control volumes. The liquid phase is represented by Lagrangian parcels in KIVA simulations. Each parcel represents a finite number of physical droplets that have the same state and distributed in a space smaller than the size of the grid cell. The number of droplets represented by one parcel can be either greater than 1 (parcel is a sample of multiple droplets) or smaller than 1 (parcel is a sample of multiple realizations). The continuous liquid core near the injector nozzle is also represented by

parcels as "blobs" of liquid [83], in which case the number of "blobs" represented by one parcel is often less than 1.

Improvements to the original KIVA-3V Release 2 code have been added in the ongoing research in the author's lab. Major improvements and additions to the KIVA's original set of sub-models include multi-component droplet evaporation [118], spray impingement and wall film dynamics [99], multi-component wall film evaporation [116], efficient chemical kinetics computation [106], *etc.*

1.6 Scope of the Present Study

The works presented in this dissertation are classified into two categories: the development of computational models, and the application of these models in engine study and innovation.

As for the model development, this dissertation addresses the simulation of the mixture preparation processes, as well as the evaluation of the effects of mixture preparation on the engine operation. As illustrated in Fig. 1.1, two important processes in the mixture preparation, the evaporation of the fuel droplet, as well as the aerodynamic and flashing breakup of the fuel droplet, are modeled in this dissertation. Also modeled is the combustion process which takes the prepared mixture and determines the combustion outcomes. In CI engine operation, the mixture preparation affects the spontaneous ignition which is calculated using the efficient chemical kinetics solver introduced in this dissertation; In SI engine operation, the mixture preparation affects the flame propagation and knocking behavior which are simulated using the unified combustion model developed in the present study.

Each of the four computational models are described in detail in this dissertation. Demonstrative simulations of spray and engine operation are also included in this dissertation for each model.

Figure 1.2 illustrates the interaction between the new droplet evaporation model and the KIVA CFD platform used in the present study. The droplet evaporation model operates upon the KIVA's Lagrangian parcel framework, and has access to the state of the gaseous mixture in the vicinity of the given Lagrangian parcel. The droplet evaporation model calculates the evaporation rate and heat transfer rate through the interface between the liquid phase and the gas phase. The evaporation model also integrates the rates in time, and advances the state of droplet stored in

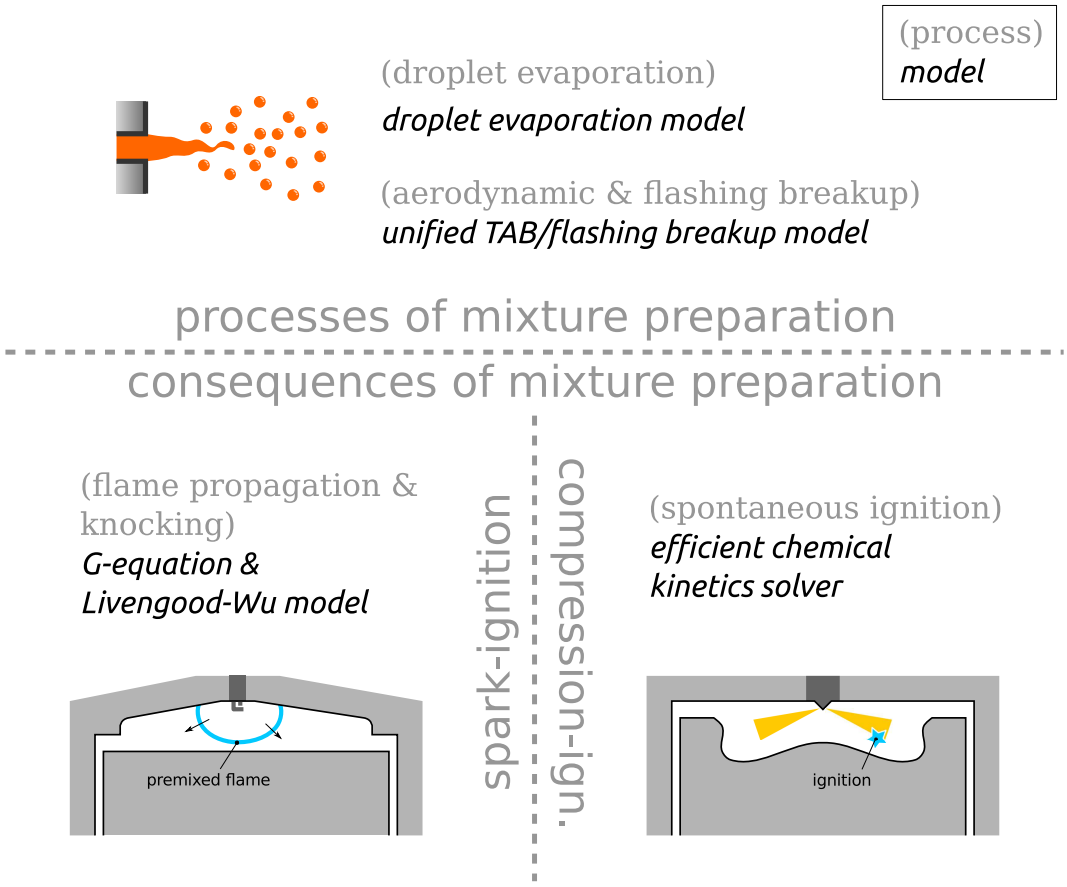

Figure 1.1: The fundamental processes addressed and the computational models developed in the present study.

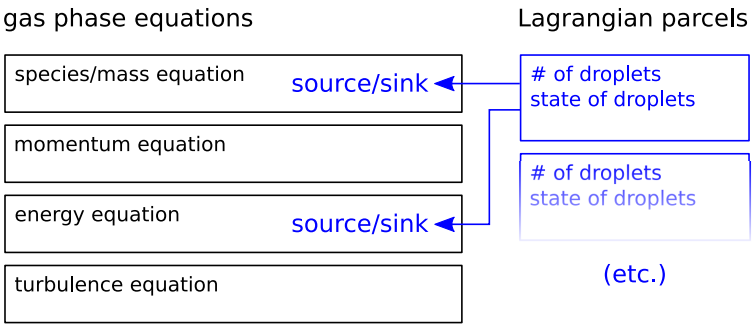

Figure 1.2: The framework of the CFD program with the custom droplet evaporation model. The highlighted parts include the contribution of the present study.

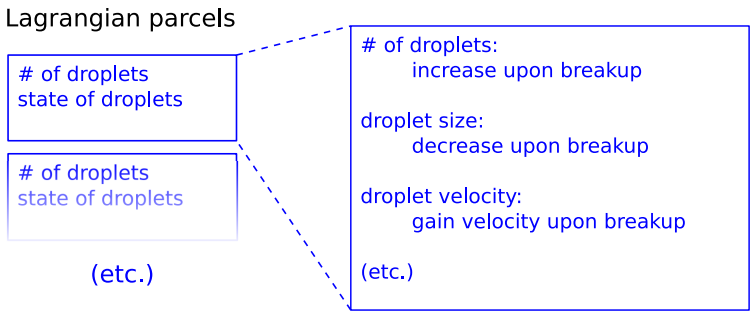

Figure 1.3: The framework of the CFD program with the combined aerodynamic/flashing breakup model. The highlighted parts include the contribution of the present study.

the Lagrangian parcel, and the state of gas stored in the FVM cells. From the perspective of the gas phase CFD, the droplet evaporation model evaluates the source term in the species/mass and energy equation, due to the evaporation of the liquid droplet.

As shown in Fig. 1.3, the combined flashing and aerodynamic breakup model operates within the KIVA's Lagrangian parcel framework, and does not have immediate influence on the gas phase computation. The combined breakup model tracks the magnitude of the aerodynamic-load-induced distortion and the internal bubble growth for each parcel, and triggers the breakup event once any of the breakup criteria is satisfied. Upon breakup, the combined breakup model calculates the state and quantity of the secondary droplets, and updates the Lagrangian parcel with these values. Thus, the Lagrangian parcel turns into a representation of the secondary droplets, from the representation of the pre-breakup droplets. Not adopted in this study is the creation of new Lagrangian parcels upon breakup, due to its complexity, and the consequent penalty on the efficiency of data storage and access.

The efficient chemical kinetics solver is developed primarily for the simulation of CI engine

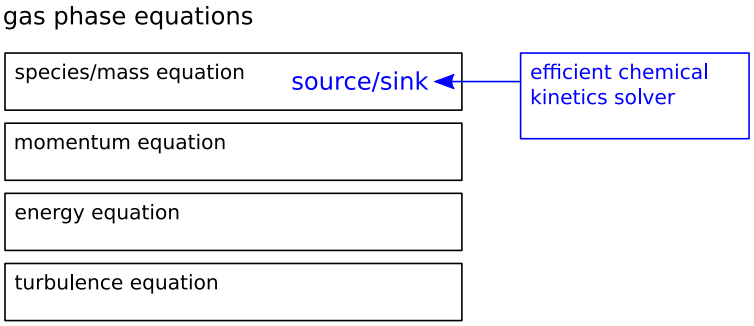

Figure 1.4: The framework of the CFD program with the efficient chemical kinetics solver. The highlighted parts include the contribution of the present study.

operation. As illustrated in Fig. 1.4, the chemical kinetics solver evaluates the chemical source term in the species equation, and integrates the source term forward in time for each of the FVM cells. It should be noted that the chemical kinetics solver does not have direct influence on the KIVA's gas phase energy equation. This is due to the fact that the chemical energy is embedded in the specific enthalpy of each species. With the change of the local composition, the energy conservation automatically accounts for the exchange between chemical energy and thermal energy, and causes local temperature variation as a result of chemical reaction.

Figure 1.5 shows the CFD framework with the unified flame propagation and spontaneous ignition model, which is developed primarily for SI engine simulation. Two new governing equations, the G- and H-equation, are implemented in the KIVA's gaseous CFD platform. The local value of the G is then translated into the local chemical reaction advancement, which determines the chemical source term in the species equation. As with the efficient chemical kinetics model, the combined flame propagation and spontaneous ignition model does not alter the energy equation.

Apart from the development of the four computational models, and the demonstrative simulations for each model, the new chemical kinetics solver is extensively used in the study of CI engine operation and the discovery of various advanced CI engine concepts. The CI engine studies are presented as components of Chap. 4, as they are closely related to the interaction between mixture preparation and local chemical kinetics.

Section 4.3 introduces the concept of single injection ignition phase curve, which shows the relation between the ignition timing and the SOI timing. The ignition phase curve is explained based on the competition between the fuel-air mixing and the chemical kinetics that leads to the

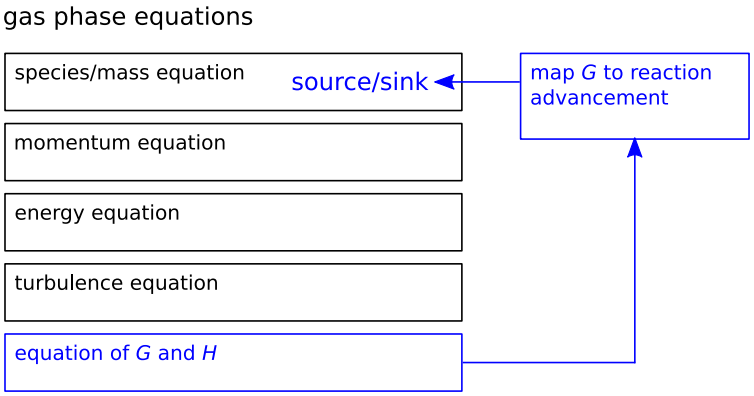

Figure 1.5: The framework of the CFD program with the unified flame propagation and spontaneous ignition model. The highlighted parts include the contribution of the present study.

ignition. The study also addresses and explains the effects of the combustion chamber geometry, the gas temperature, the engine load, and the overall equivalence ratio on the behavior of the ignition phase curve.

Section 4.4 studies a novel type of CI engine that swaps the diesel fuel with gasoline. Comparing to the diesel fuel, gasoline fuel is more volatile and less reactive, altering both the mixture preparation and the chemical kinetics. Various approaches are tested to bring the familiar diesel-like SOI control authority back to the gasoline CI operation. The pollutant formation mechanisms in gasoline-fueled CI engine operation is also discussed in detail.

A first-of-its-kind stoichiometric CI engine concept is introduced in Sec. 4.5. The proposed concept ignites premixed natural gas and air with a direct injection of diesel. Unlike the existing dual fuel CI engine technology, the proposed concept keeps the overall equivalence ratio near stoichiometric, which enables the effective application of the TWC after-treatment system. The proposed concept is demonstrated by engine simulations with the efficient chemical kinetics solver over a large range of engine load and engine speed. Limitations of the proposed concept are also identified and explained based on the simulation result.

Chapter 2

Modeling of Droplet Evaporation

In practical CFD engine simulations, the liquid fuel is represented by Lagrangian parcels. The interactions between the gas and liquid phase, *e.g.*, evaporation, drag, *etc.*, are formulated as the exchanges of mass, momentum, and energy between the Lagrangian parcels and the gas phase FVM cells. In this study, a droplet evaporation model is constructed upon the Lagrangian parcel paradigm. The new model is based on the previous work by the author's laboratory [118]. Major improvements include: real fluid property estimation, updated VLE solver, modular implementation, and various modern software development practices. The droplet evaporation model is validated using single droplet evaporation data from the literature. Integrated into the KIVA software, the new droplet evaporation model is also validated by the spray evaporation simulation of the standard Spray G experiment, and is readily available for practical engine simulations.

2.1 Thermal and Transport Properties of Fluid

In the droplet evaporation model, the thermal and transport properties of both multi-component liquid and multi-component gas are calculated with models for general fluids. These models cover a wide range of pressure, and they are valid under low pressure as well as near-critical and supercritical conditions. These models only use input parameters that can be easily obtained from the literature and public databases. In addition, only input parameters for pure fluids are needed to calculate the properties of mixtures.

The Peng-Robinson (PR) equation of state (EOS) with the van der Waal mixing rule [74] is used to calculate the p-T-$\hat{v}$ relation of real multi-component fluid. The PR EOS reads,

$$p = \frac{\hat{R}T}{\hat{v} - b} - \frac{a}{\hat{v}^2 + 2b\hat{v} - b^2}, \tag{2.1}$$

where $a = \sum_i^{n_{sp}} \sum_j^{n_{sp}} X_i X_j a_{ij}$, $b = \sum_i^{n_{sp}} X_i b_i$,

$$
\begin{aligned}
a_{ij} &= (1 - \delta_{ij})\sqrt{a_i a_j}, \\
a_i &= 0.457235 \frac{\hat{R}^2 T_{ci}^2}{p_{ci}} \cdot \left[1 + \kappa_i \left(1 - \sqrt{\frac{T}{T_{ci}}}\right)\right]^2, \\
b_i &= 0.077796 \frac{\hat{R} T_{ci}}{p_{ci}}, \\
\kappa_i &= 0.37464 + 1.54226\omega_i - 0.26692\omega_i^2.
\end{aligned}
$$

Chueh and Prausnitz [11] developed a model for the binary interaction between non-polar components,

$$1 - \delta_{ij} = \left(\frac{2 v_{ci}^{1/6} v_{cj}^{1/6}}{v_{ci}^{1/3} + v_{cj}^{1/3}}\right)^6 \tag{2.2}$$

The enthalpy departure is derived based on the PR EOS [78],

$$\hat{h} - \hat{h}_{ig} = \hat{R}T(Z-1) + \frac{T\frac{\mathrm{d}\,a}{\mathrm{d}\,T} - a}{2\sqrt{2}b} \ln\left(\frac{Z + (1+\sqrt{2})B}{Z + (1-\sqrt{2})B}\right), \tag{2.3}$$

where $Z = \frac{p\hat{v}}{\hat{R}T}$, $B = \frac{bp}{\hat{R}T}$,

$$
\begin{aligned}
\frac{\mathrm{d}\,a}{\mathrm{d}\,T} &= \frac{1}{2} \sum_i^{n_{sp}} \sum_j^{n_{sp}} (1 - \delta_{ij}) X_i X_j \left(\sqrt{\frac{a_j}{a_i}} \frac{\mathrm{d}\,a_i}{\mathrm{d}\,T} + \sqrt{\frac{a_i}{a_j}} \frac{\mathrm{d}\,a_j}{\mathrm{d}\,T}\right), \\
\frac{\mathrm{d}\,a_i}{\mathrm{d}\,T} &= -\frac{\kappa_i a_i}{\left[1 + \kappa_i \left(1 - \sqrt{\frac{T}{T_{ci}}}\right)\right] \sqrt{T_{ci} T}}.
\end{aligned}
$$

With the ideal gas thermal properties of pure fluid calculated by the NASA 7-coefficient polynomial, Eq. 2.3 gives the enthalpy of a real fluid mixture. The modeled specific enthalpy of n-hexane liquid and vapor is plotted in Fig. 2.1, and is compared with the NIST database [56].

The viscosity and thermal conductivity are calculated using the method developed by Chung *et al.* [14] and Chung *et al.* [13]. The model is based on the Chapman-Enskog Theory, and is valid for high pressure and condensed fluid, as well as low pressure gas. Details about the model are documented in Appx. A. The modeled liquid and gas viscosity and thermal conductivity are compared with literature data in Fig. 2.2 to 2.5.

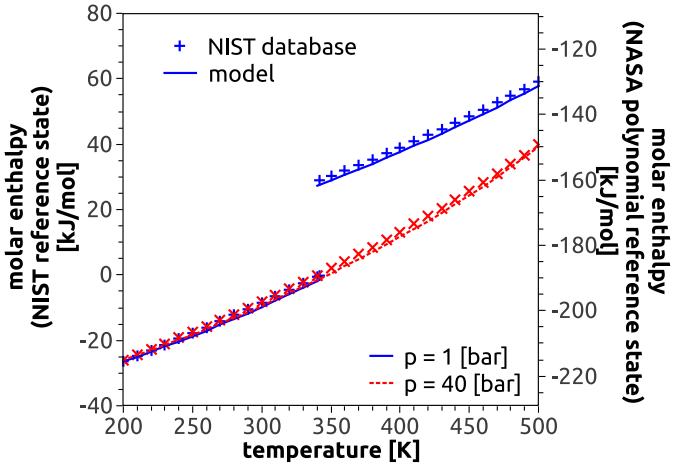

Figure 2.1: The modeled enthalpy of n-hexane and the data from NIST database [56]. The blue and red color represents 1 bar and 4 bar ambient pressure, respectively.

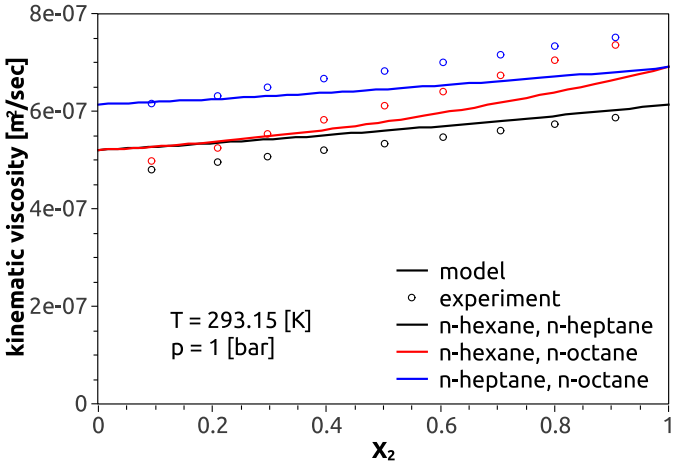

Figure 2.2: The modeled viscosity of binary liquid systems of n-hexane/n-heptane/n-octane, and measured data [18].

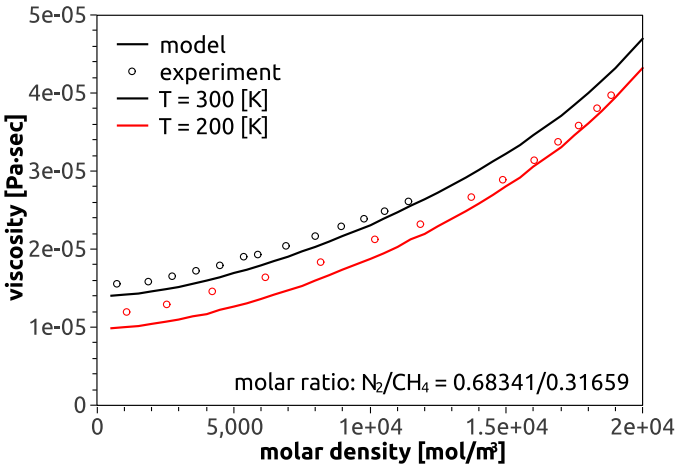

Figure 2.3: The modeled viscosity of binary gas systems of nitrogen/methane, and measured data [26].

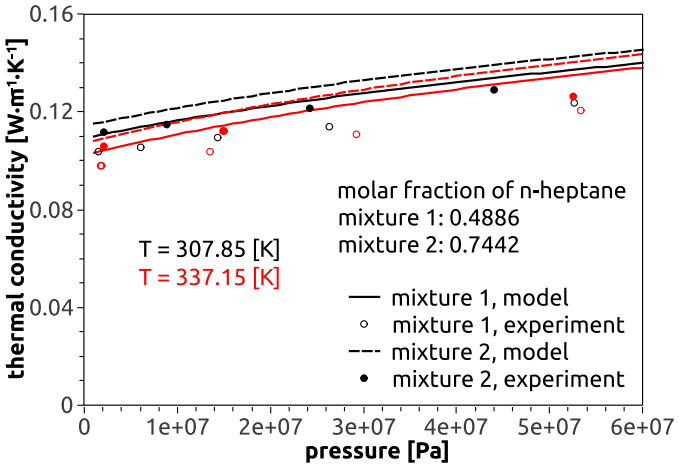

Figure 2.4: The modeled thermal conductivity of binary liquid systems of n-heptane/isooctane, and measured data [28].

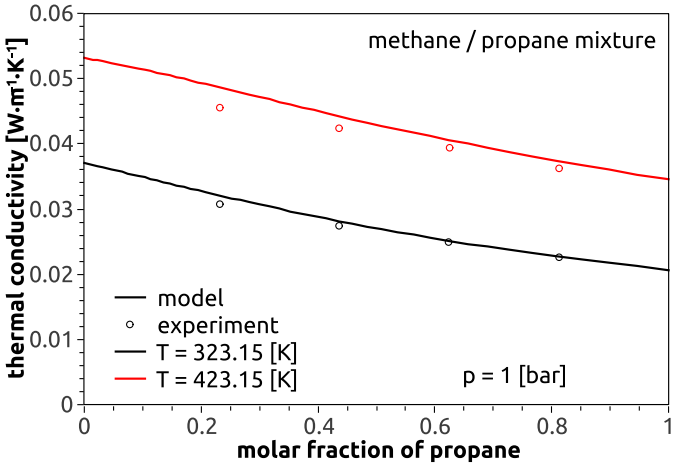

Figure 2.5: The modeled thermal conductivity of binary gas systems of methane/propane, and measured data [93].

In the previous droplet evaporation models, the mass diffusivity is often estimated such that the liquid Lewis number $Le_l = 10$, and the gas Lewis number $Le_g = 1$. In this research, the Chapman-Enskog-based low pressure binary diffusivity model [35, 66] is extended to high pressure condition following a reduced-volume-based empirical correlation [21, 84]. An approximate mixture-averaged diffusivity model is obtained following the method by Riazi and Whitson [84]. Details about the model are documented in Appx. B. Extensive comparisons between the calculated properties of fluid and the data from literature are conducted. The liquid and gas diffusivity obtained in both the current study and the literature are shown in Fig. 2.6.

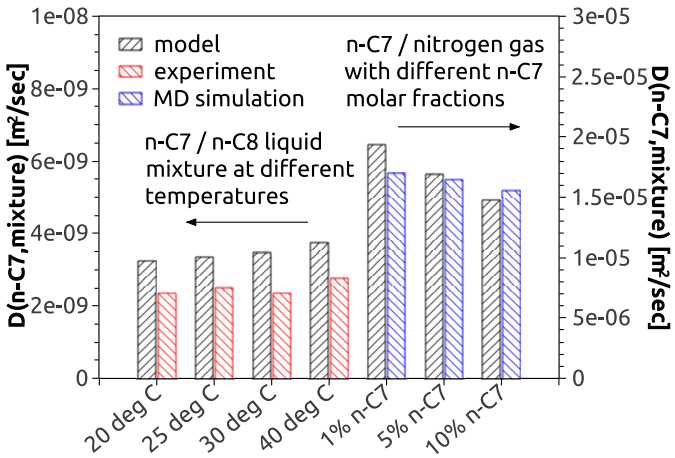

Figure 2.6: The modeled mixture-averaged diffusion coefficient of n-heptane in liquid and gas binary systems of n-heptane/nitrogen, compared with measured data [65] and molecular dynamics simulation [7].

2.2 VLE Computation

Given a liquid surface state, the gas surface state is calculated such that the liquid and gas are in equilibrium at the interface. Equilibrium requires the temperature and the fugacity of each species to be continuous through the phase interface,

$$T_{ls} = T_{gs}, \tag{2.4}$$

$$\phi_{lis} X_{lis} = \phi_{gis} X_{gis}, \tag{2.5}$$

where $\phi_i = \frac{f_i}{pX_i}$ is the fugacity coefficient of species i in the local fluid mixture. The fugacity coefficient can be calculated with the PR EOS [78],

$$\ln \phi_i = \frac{b_i}{b}(Z-1) - \ln(Z-B) + \frac{A}{2\sqrt{2}B}\left(\frac{b_i}{b} - \frac{2}{a}\sum_j^{n_{sp}} X_j a_{ij}\right) \ln\left(\frac{Z+(1+\sqrt{2})B}{Z+(1-\sqrt{2})B}\right), \tag{2.6}$$

where $Z = \frac{p\hat{v}}{\hat{R}T}$, $A = \frac{ap}{\hat{R}^2T^2}$, and $B = \frac{bp}{\hat{R}T}$.

In the VLE computation, the considered species include all species in the liquid fuel, as well as a "filler gas" specie, which is represented by nitrogen in this research. The equilibrium solver solves the non-linear equations Eq. 2.5 with $X_{gis}, i \in \{\text{fuel species}\}$, and $X_{lis}, i = \text{nitrogen}$ as independent variables. The nitrogen molar fraction in gas, $X_{gis}, i = \text{nitrogen}$, is set such that the gas molar

fractions add up to 1. The fuel species molar fractions in liquid, $X_{lis}, i \in \{\text{fuel species}\}$, are set such that their relative ratios are the same as before nitrogen is dissolved in the liquid. It should be noted that the molar fraction of nitrogen in the liquid is often very small unless it was under ultra-high pressure. It is assumed in this research that the nitrogen dissolved in liquid only affects the VLE calculation, and it does not diffuse into the liquid region. In the case that the surface liquid is not superheated, the "filler gas" molar fraction is greater than or equal to 0. In the case that the surface liquid is superheated, the "filler gas" molar fraction drops to 0, the gas pressure is increased to get a physically-non-equilibrium solution of Eq. 2.5, and an indicator is returned to show that the liquid surface is undergoing flashing process.

The result generated by the VLE solver is compared extensively with data from literature. Figure 2.7 shows the VLE of a binary system of n-hexane/n-heptane mixtures. The predicted isobaric bubble point and dew point curves match with those from measurement [38] through the full range of blending ratio. Figure 2.8 shows the VLE of a ternary system of n-hexane/cyclohexane/n-heptane mixtures at atmospheric pressure. The test samples multiple liquid mixtures of different blending ratios, and finds their saturation temperature under atmospheric pressure, as well as the composition of the saturated vapor in equilibrium with the liquids. As shown in Fig. 2.8, the predicted saturation temperature and vapor composition agree with those from measurement [38]. Figure 2.9 shows the isothermal bubble point and dew point curves of a propane/carbon-dioxide system over a large range of pressure up to the critical locus and various temperatures. The predicted curves are compared with measurement [82] and show reasonable accuracy. The comparisons demonstrate the capability of the model to predict the gas phase state at the phase interface under the typical internal combustion engines' operation pressure.

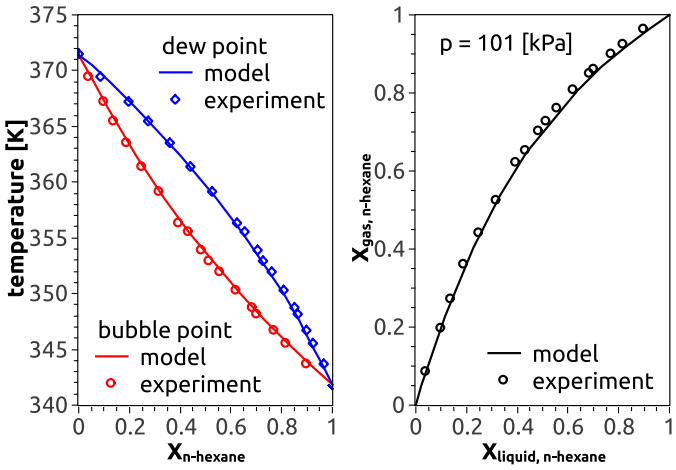

Figure 2.7: The VLE calculation of binary systems of n-hexane/n-heptane, and measured data [38].

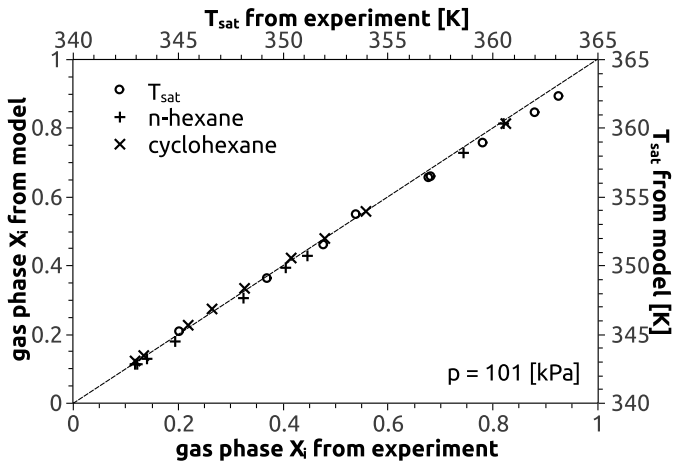

Figure 2.8: The VLE calculation of ternary systems of n-hexane/cyclohexane/n-heptane, and measured data [38].

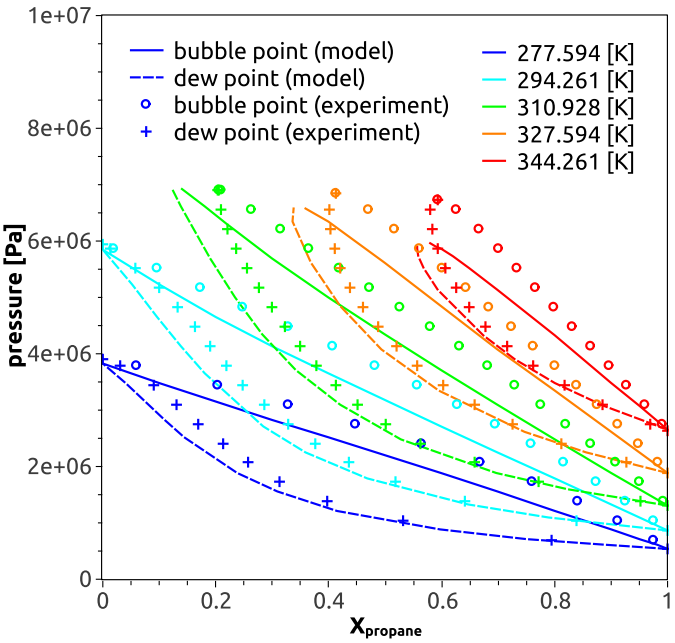

Figure 2.9: The VLE calculation of binary systems of propane/carbon-dioxide, and measured data [82].

2.3 Droplet Evaporation Model

In addition to the VLE calculation, the droplet evaporation model includes a liquid phase model and a gas phase model.

Assuming the droplet is spherical, and the problem is spherically symmetric, one can write the 1-D governing equations for the energy and species transport in the liquid. For a droplet having instantaneous radius $R = R(t)$, $\forall\ r \in (0, R)$,

$$\frac{\mathrm{D}}{\mathrm{D}\,t}\left(4\pi r^2 \rho_l Y_i\right) = \frac{\partial}{\partial r}\left(4\pi r^2 \rho_l D_i^e \frac{\partial Y_i}{\partial r}\right), \tag{2.7}$$

$$\frac{\mathrm{D}}{\mathrm{D}\,t}\left(4\pi r^2 \rho_l h_l\right) = \frac{\partial}{\partial r}\left(4\pi r^2 k^e \frac{\partial T}{\partial r}\right). \tag{2.8}$$

The boundary conditions at the phase interface $r = R(t)$ is determined by the mass flux of each

species Γ_i^{mass} and the energy flux, Γ^{energy},

$$4\pi R^2 \Gamma_i^{mass} = \dot{m}\epsilon_i = \dot{m} Y_{lis} - 4\pi R^2 \rho_l D_i^e \left.\frac{\partial Y_i}{\partial r}\right|_{r=R}, \tag{2.9}$$

$$4\pi R^2 \Gamma^{energy} = \sum_i \dot{m}\epsilon_i h_{lis} - 4\pi R^2 k^e \left.\frac{\partial T}{\partial r}\right|_{r=R}. \tag{2.10}$$

At the droplet center, $r = 0$, $\Gamma_i^{mass} = 0$, and $\Gamma^{energy} = 0$. The concept of equivalent diffusivity is used to account for the internal circulation in the liquid phase [1],

$$\frac{D_i^e}{D_i} = 1.86 + 0.86 \tanh\left[2.245 \log_{10}\left(\frac{Re_l Sc_{li}}{30}\right)\right], \tag{2.11}$$

$$\frac{k^e}{k} = 1.86 + 0.86 \tanh\left[2.245 \log_{10}\left(\frac{Re_l Pr_l}{30}\right)\right]. \tag{2.12}$$

By assuming ρ, c_p, D_i^e, and k^e being constant throughout the liquid domain, neglecting the bulk liquid motion, applying a deforming reference frame such that $r = R(t)\xi$, and introducing different mass and heat diffusion time scales, such that $\tau_i = \frac{t}{R^2/D_i^e}$, $\tau_T = \frac{t}{R^2 \rho_l c_p / k^e}$, the government equations become:

$$(1 + 2\tau_i Pe_i)\frac{\partial Y_i}{\partial \tau_i} + \left(\xi Pe_i - \frac{2}{\xi}\right)\frac{\partial Y_i}{\partial \xi} - \frac{\partial^2 Y_i}{\partial \xi^2} = 0, \tag{2.13}$$

$$(1 + 2\tau_T Pe_T)\frac{\partial T}{\partial \tau_T} + \left(\xi Pe_T - \frac{2}{\xi}\right)\frac{\partial T}{\partial \xi} - \frac{\partial^2 T}{\partial \xi^2} = 0, \tag{2.14}$$

where the Péclet numbers are:

$$Pe_i = -\frac{R\,\mathrm{d}\,R/\,\mathrm{d}\,t}{D_i^e}, \tag{2.15}$$

$$Pe_T = -\frac{R\,\mathrm{d}\,R/\,\mathrm{d}\,t}{k^e/(\rho_l c_p)}. \tag{2.16}$$

It is clear that the governing equations for the species and energy transport in the 1-D liquid domain share the identical form, which enables unified solution strategy. For such 1-D problems that share the same general form, Zeng and Lee [118] developed an approximate analytical model

for the difference between the surface state and the mean state,

$$\frac{\mathrm{d}(\Theta_s - \bar{\Theta})}{\mathrm{d}\,t} = \frac{\mu_1^2 \left[0.2E(Pe)\ \frac{\partial \Theta}{\partial r}\big|_{r=R} R - (\Theta_s - \bar{\Theta})\right]}{E(Pe)R^2/D^e}, \tag{2.17}$$

where Θ represents either Y_i or T. $E(Pe)$ is the surface-mean difference with a given Péclet number normalized by the surface-mean difference with $Pe = 0$, and is tabulated along Pe [114]. With Eq. 2.17, the 1-D problem is approximated by a quasi 1-D problem in which both the mean states and the surface-mean differences are tracked. Compared to the 0-D model (infinite diffusion model), the quasi 1-D model provides accurate estimation of the surface state. Compared to the 1-D FVM model, the quasi 1-D model requires significantly less computation time.

The gas phase model closes the problem by calculating the mass and energy fluxes in the boundary conditions, Eq. 2.9 and 2.10. The mass flux is calculated using the method by Abramzon and Sirignano [1],

$$\Gamma_i^{mass} = \frac{\bar{\rho}_g \bar{D}_g \ln(1 + B_i)}{2R} Sh_i. \tag{2.18}$$

The effective Sherwood number for evaporating droplet is:

$$Sh_i = 2 + \frac{Sh_0 - 2}{F(B_i)}, \tag{2.19}$$

where,

$$Sh_0 = 2 + 0.552 Re^{1/2} \bar{Sc}^{1/3}, \tag{2.20}$$

$$F(B_i) = (1 + B_i)^{0.7} \frac{\ln(1 + B_i)}{B_i}, \tag{2.21}$$

and the transfer number is:

$$B_i = \frac{Y_{gis} - Y_{i\infty}}{1 - Y_{gis}}. \tag{2.22}$$

The energy flux is given by Jin and Borman [39],

$$\Gamma^{energy} = \frac{Nu\bar{k}_g}{2R} \xi_T (T_s - T_\infty) + \sum_i \Gamma_i^{mass} h_{gis}. \tag{2.23}$$

The Nusselt number in the non-evaporative limit,

$$Nu = 2 + \frac{0.555 Re^{1/2} \bar{Pr}^{1/3}}{\left[1 + 1.232 / \left(Re \bar{Pr}^{4/3}\right)\right]^{1/2}}, \tag{2.24}$$

where,

$$\xi_T = \frac{z_T}{e^{z_T} - 1}, \tag{2.25}$$

$$z_T = \frac{2R \sum_i \Gamma_i^{mass} \bar{c}_{pgi}}{Nu \bar{k}_g}. \tag{2.26}$$

The average gas phase properties $\bar{(\cdot)}_g$ are estimated using the "$\frac{1}{3}$" rule,

$$\bar{(\cdot)} = (\cdot)_{gs} + \frac{1}{3}\left[(\cdot)_\infty - (\cdot)_{gs}\right]. \tag{2.27}$$

The gas phase model takes the state of the gas at the interface, which is calculated by the VLE solver, and evaluates the boundary conditions of the liquid phase problem, providing an explicit closure to the problem.

The evaporation under low and high Péclet number is very different. With $Pe << 1$, the surface recession is significantly slower than the diffusion process in the liquid, and the distribution of state is relatively smooth in the droplet due to the pronounced diffusion effect, as shown in Fig. 2.10. As $Pe >> 1$, with the surface recessing rapidly, the diffusion process does not have enough time to smooth the state in the liquid, and the pronounced recession effect results in a steep boundary layer near the surface, while the internal state deeper than the boundary layer stays roughly unchanged, as shown in Fig. 2.11. When the Péclet number is small, the relatively fast diffusion supplies volatile components to the droplet surface, thus the multi-component effect becomes more pronounced. As shown in Fig. 2.10 and 2.11, the quasi 1-D model precisely recovers the surface state predicted by the fully resolved 1-D FVM model at both high and low Péclet number, and efficiently enables accurate VLE calculation at the droplet surface.

The evaporation rate is validated against multiple suspended droplet experiments [9, 69, 30] (as shown in Fig. 2.12) and a floating droplet experiment [12] (as shown in Fig. 2.13). The comparisons show reasonable agreement between the model and the experiments under the condition without

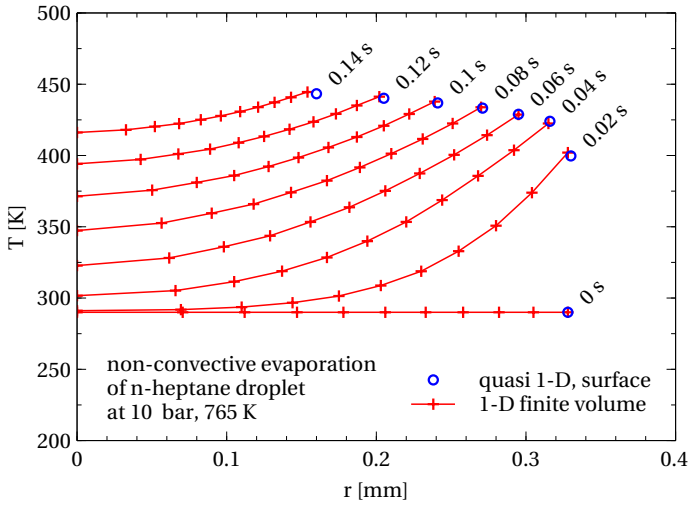

Figure 2.10: The temperature distribution in a slowly evaporating droplet.

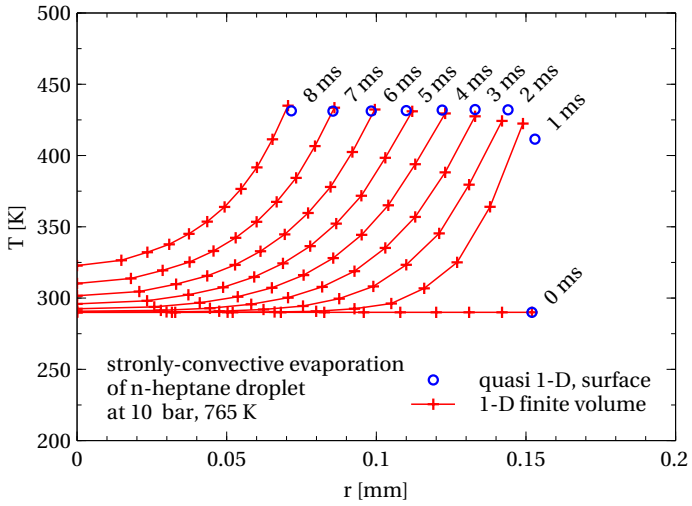

Figure 2.11: The temperature distribution in a rapidly evaporating droplet.

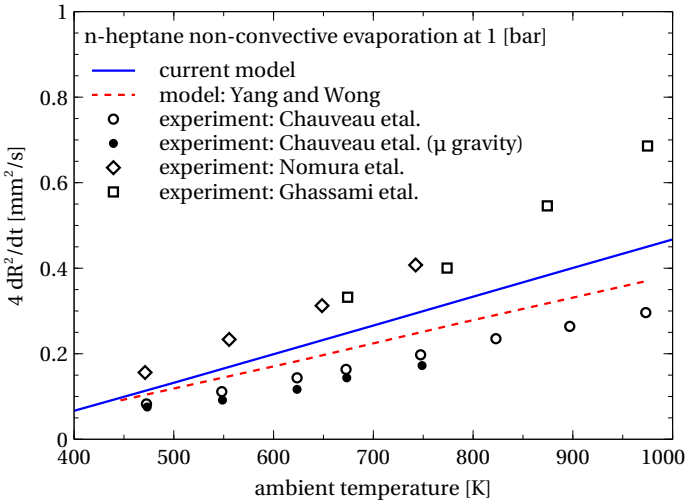

Figure 2.12: The calculated evaporation rate of n-heptane droplet and data from suspended droplet experiments [9, 69, 30] and from model in literature [113].

relative motion between the droplet and the ambient gas. The ambient pressure used in the tests (1 to 2 bar) is representative for the intake manifold condition in modern boosted engines.

In the test shown in Fig. 2.14, the pressure is elevated to 50 bar, which is relevant to the direct-injection engine in-cylinder condition. As shown, the predicted droplet size variation matches reasonably well with the measured droplet size variation during a suspend droplet evaporation experiment [69].

The effect of ambient flow on the evaporation rate is verified against the empirical correlation [81],

$$\frac{K(Re_g)}{K(0)} = 1 + 0.276 Sc_g^{\frac{1}{3}} Re_g^{\frac{1}{2}} \approx 1 + 0.25 Re_g^{\frac{1}{2}}, \tag{2.28}$$

where the evaporation rate is quantified by the droplet surface area reduction rate K (with the unit of $\frac{\text{mm}^2}{\text{s}}$). The value of $\frac{K(0)}{K(Re_g)}$ represents the droplet life time normalized by that with $Re_g = 0$. The comparison between the modeled normalized droplet life time and the normalized droplet life time indicated by the empirical correlation is shown in Fig. 2.15. The comparison shows reasonable accuracy of the model in predicting the evaporation of fuel droplet traveling in gas, which often has Re_g well below 1000 in typical internal combustion engine.

In case that the droplet consists multiple components of different volatility, the species of higher volatility is depleted from the droplet faster comparing to the less volatile species. The

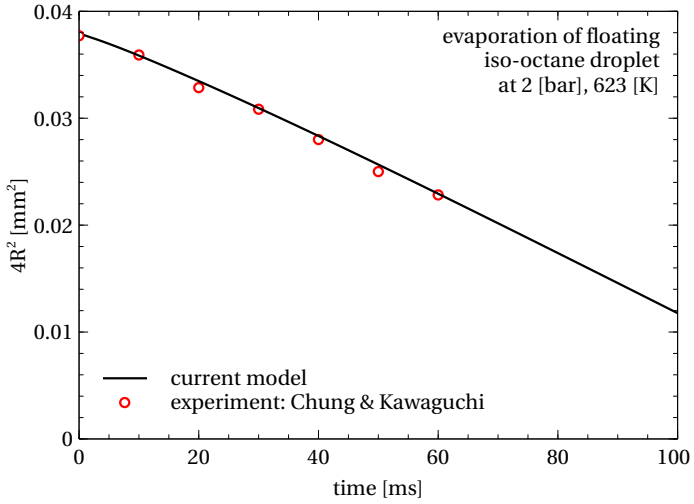

Figure 2.13: The calculated evaporation progress of isooctane droplet and data from float droplet experiment [12].

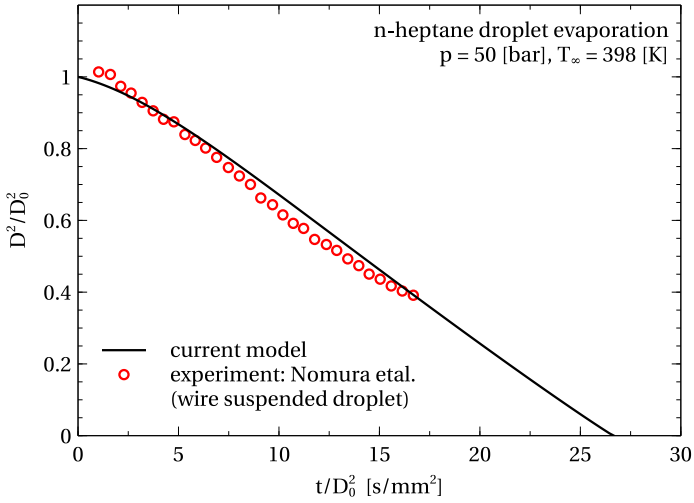

Figure 2.14: The calculated evaporation progress of n-heptane droplet under high pressure and data from suspended droplet experiment [69].

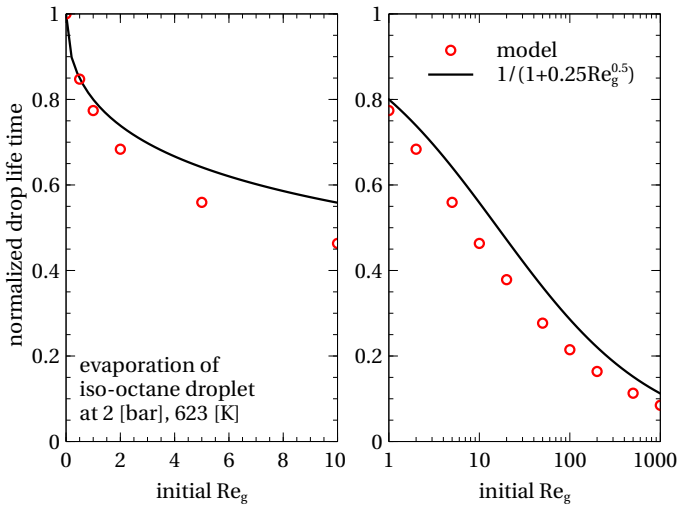

Figure 2.15: The calculated evaporation rate of isooctane droplet and an empirical correlation [81].

multi-component droplet evaporation experiments [80] are used to validate the multi-component droplet evaporation computation. In the experiments, n-decane, n-dodecan, n-tetradecan were blended with n-hexadecane. The molar fraction of the more volatile species in the droplets was recorded at different stages of the evaporation process. The evaporation progress is quantified by 1 minus the ratio between the instantaneous and initial droplet surface area. The computational and experimental results are compared in Fig. 2.16. The result shows the capability of the evaporation model in predicting the evaporation of multi-component droplet. As shown, for the liquid mixture with relatively large volatility difference, *i.e.* in the n-decane/n-hexadecane system, the more volatile species is depleted rapidly at the surface, while the bulk fluid still contains considerable amount of the more volatile species. After the near-depletion at the surface, the evaporation of the more volatile species is controlled by the mass diffusion from the bulk to the surface. With reducing the volatility difference, such preferential evaporation effect becomes less pronounced, but the more volatile species always has lower mass fraction at the surface comparing to the spatial mean state, given that the initial state is uniform through the droplet's radial direction.

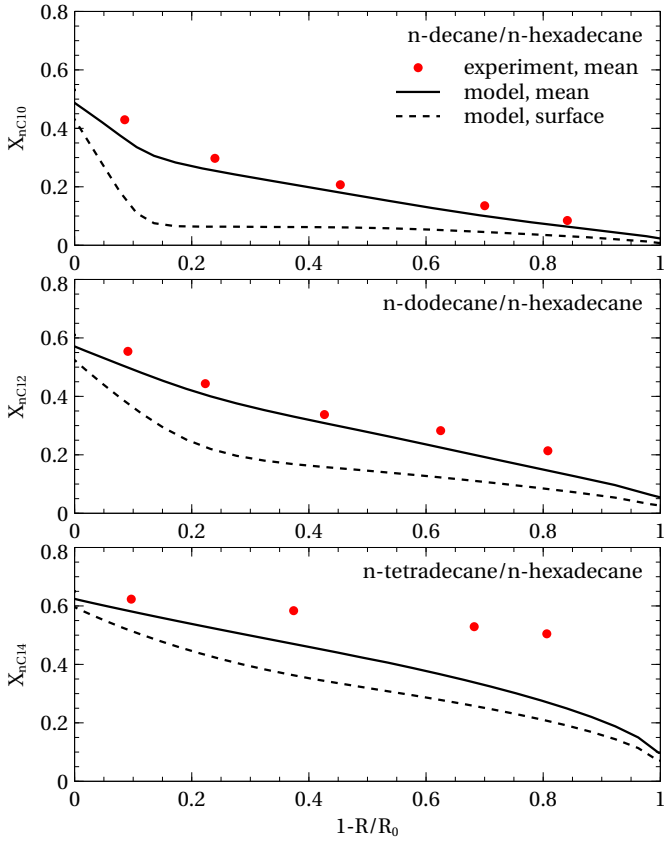

Figure 2.16: The molar fraction of the more volatile species in the droplet at different stage of the evaporation process [80].

2.4 The Spray G Simulation

The Spray G [27] is a standard gasoline direct-injection (GDI) spray experiment shared over the Engine Combustion Network (ECN), a community of internal combustion engine research. The purpose of the standard Spray G experiment is to act as a baseline case for the study of modern GDI spray, as well as a benchmark case for numerical simulation of the GDI spray.

In the present study, the new droplet evaporation code is integrated into the KIVA program. The customized KIVA program is used to simulate the standard Spray G. The simulation and experimental conditions are tabulated in Tab. 2.1. The computation simulates one of the eight nozzles by using a $\frac{1}{8}$ sector grid and applying periodic boundary condition on the two radial cut planes. The spray is centralized in the azimuthal direction, *i.e.* having 22.5° apart from either of the two radial cut planes. The configuration as well as the computational grid is shown in Fig. 2.17. The start of the simulation is aligned with the SOI, and the simulation stops at 1 ms after SOI. To compute the aerodynamic breakup of the liquid droplet, the breakup model introduced in Chap. 3 is used in the ECN Spray G simulation.

Figure 2.18 visualizes the predicted transient evolution of the liquid phase and the vapor phase. The liquid phase is represented by the Lagrangian parcels. Volume rendering of the gas phase fuel mass fraction distribution is used to visualize the instantaneous fuel vapor distribution. Worth mentioning is that the vapor distribution prediction as the one shown in Fig. 2.18 is important in engine simulation since it represents the outcome of the mixture preparation. The location and mass fraction of the vapor have substantial effects on the ignition, flame propagation, and formation

Table 2.1: The conditions of the standard Spray G experiment and its simulation.

Chamber shape	cylindrical	Gas composition	100% nitrogen
Chamber diameter	108 mm	Gas pressure	6 bar
Chamber height	108 mm	Gas temperature	573 K
Injector location	center, top-mount	Gas density	3.5 kg/m^3
Injector orientation	straightly downwards	Fuel composition	100% iso-octane
Number of nozzles	8	Fuel temperature	363 K
Nozzle orientation	polar angle = 37°	Fuel mass	10 mg
Nozzle diameter	0.165 mm	Rail pressure	200 bar
		Injection duration	0.68/0.78/0.76 ms (signal/full/simulation)

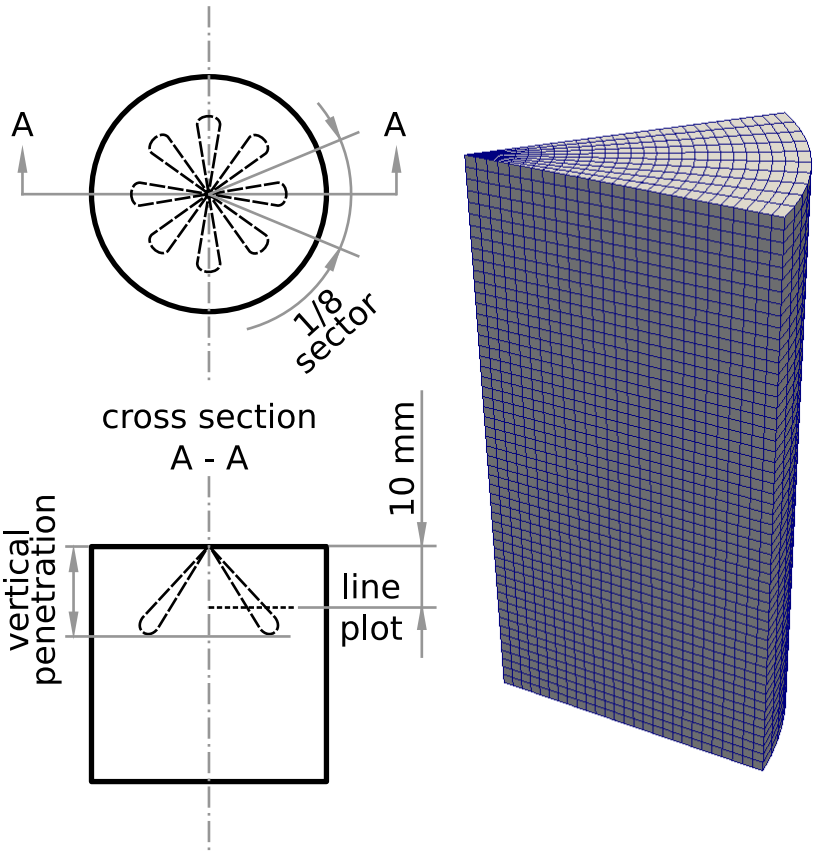

Figure 2.17: A schematic drawing of the standard Spray G experiment, the configuration of the present simulation of the Spray G (left), and the $\frac{1}{8}$ sector grid (right).

of emissions, which are all important characteristics of engine operation.

Another major task of the spray simulation is to predict the liquid and vapor penetration due to the fuel injection. As illustrated in Fig. 2.17, the projection onto the vertical direction is used to quantify the penetration length. The comparison between the penetration prediction and measurements is shown in Fig. 2.19. In the comparison, the predicted liquid penetration is marked by the location of the farthest Lagrangian parcel, while the vapor penetration is based on the height of the $X_{\text{fuel}} = 0.01$ iso-surface. Figure 2.19 demonstrates similarity between the simulation and measurement. It is also noticeable that the predicted liquid and vapor penetration are consistently shorter comparing to the measurement. This is due to the fact that the measurement is determined by the longest one of the eight plumes.

Another major task of the evaporation model and spray simulation is to predict the mixture preparation outcome by the liquid fuel injection. In order to study the simulated mixture preparation outcome, the instantaneous fuel mass fraction is plotted along a radial line which is aligned with the jet and sits 10 mm below the nozzle (as illustrated by Fig. 2.17). The computational result generated by the present simulation is compared with the result produced by Argonne National Laboratory (ANL) [37] in Fig. 2.20. The ANL result is constructed base on the ensemble average of 20 large eddy simulation (LES) realizations. Figure 2.20 shows similar level of fuel mass fraction near the spray core, demonstrating the usefulness of the present evaporation model. It is also noticeable that the fuel mass fraction by the present simulation is not as crisp as in the ANL result even though in both case the result should represent the ensemble average. This is due to the limited resolution and higher numerical diffusion of KIVA simulation comparing to the high-fidelity LES technique. Nevertheless, LES is currently impractical in industrial engine simulations; and the modular droplet evaporation model developed in this study is readily transferable to the future high-fidelity simulation techniques.

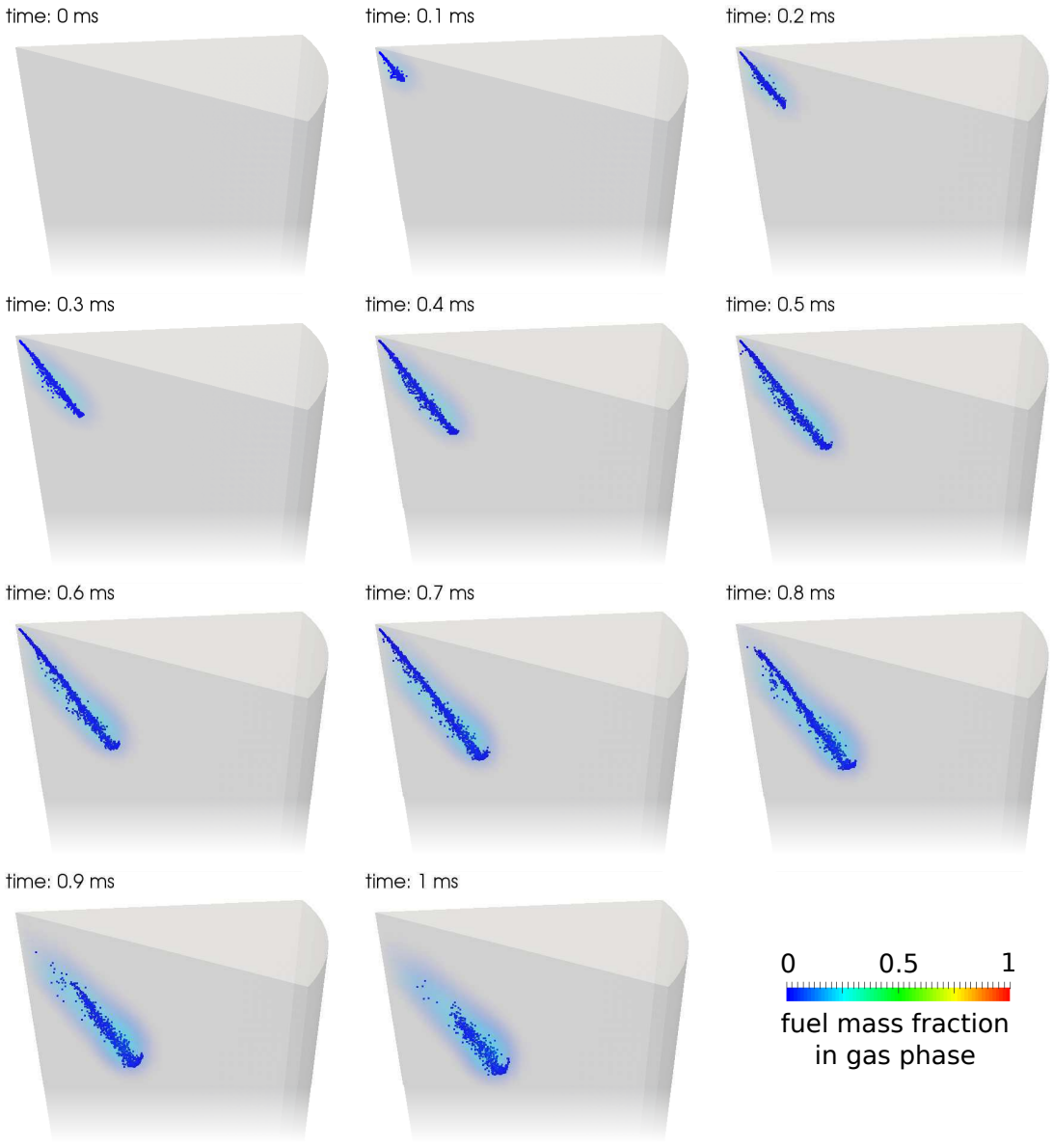

Figure 2.18: The visualization of the liquid phase (Lagrangian parcels) and the fuel vapor distribution (volume rendering of the gas phase fuel mass fraction) of the Spray G.

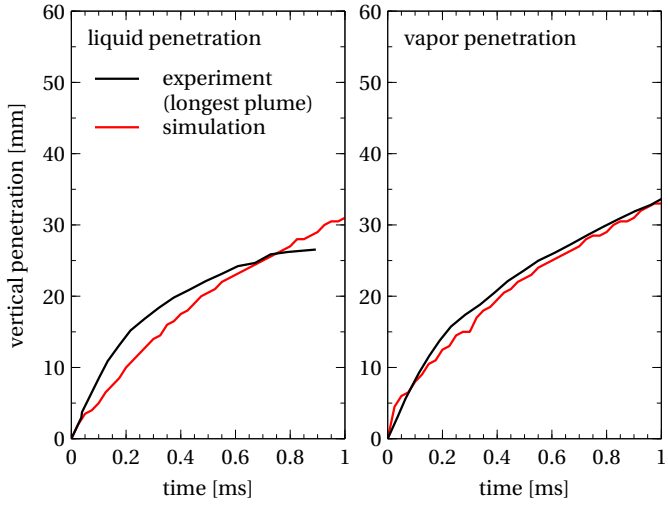

Figure 2.19: The vertical liquid and vapor penetration of the Spray G [27].

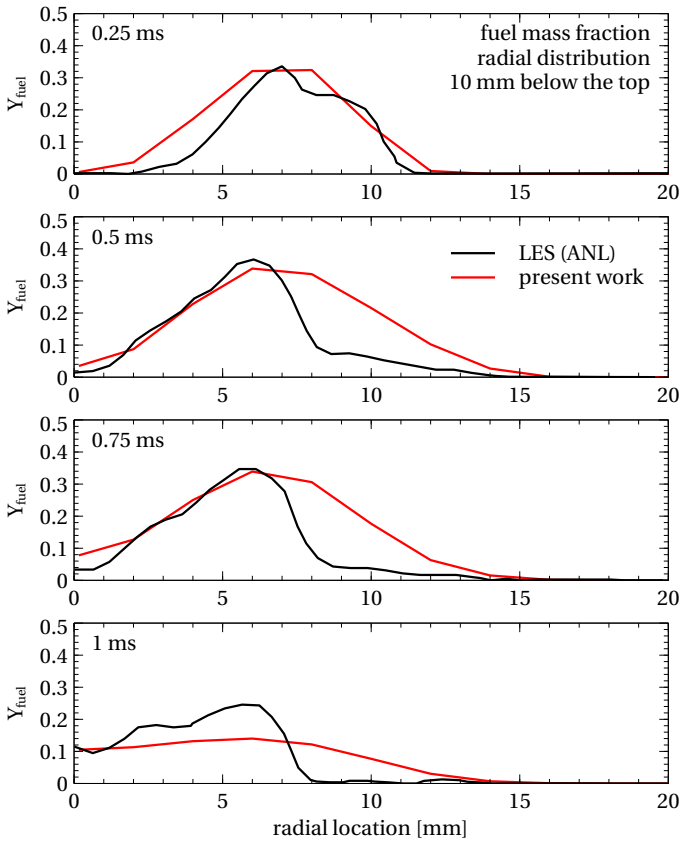

Figure 2.20: The comparison of the Spray G fuel mass fraction distribution between the present simulation and the LES study by Argonne National Lab [37].

Chapter 3

Modeling of Droplet Flash-Boiling

The breakup of the liquid jet and the liquid droplet is an important event in the process of mixture preparation. As the consequence of the breakup, fine droplets are generated and the overall liquid surface area to volume ratio rises, which enhances the droplet evaporation. Fuel spray under common engine condition is not superheated upon injection, and undergoes only aerodynamic breakup. The aerodynamic breakup is driven by the excessive kinetic energy of the liquid and the violent momentum exchange on the interface between the liquid phase and the gas phase, which is illustrated in Fig. 3.1. Also illustrated in Fig. 3.1 is another breakup mode, *a.k.a.* flashing breakup. As an effort to improve the homogeneity of the air-fuel mixture, the liquid fuel is deliberately superheated upon injection. Once the superheated liquid exits the injector nozzle and is exposed to an environmental pressure lower than the saturated vapor pressure corresponding to the liquid fuel, the liquid undergoes fast flash-boiling process. As shown in Fig. 3.1, the superheated droplet may undergoes either aerodynamic breakup or flashing breakup. In the case of flashing breakup, the expansion of the internal bubbles is the direct cause of the breakup; In the case of aerodynamic breakup, the expansion of the internal bubbles also promotes the aerodynamic-load-induced droplet distortion, hence the aerodynamic breakup process.

In the present study, a combined model for flashing and aerodynamic droplet breakup is constructed based on the previous effort in the author's lab [117]. Comparing to the previous model [117], the new model presented in this dissertation has superior performance enabled by the use of an approximate analytical solution for the problem of bubble growth. Another major improvement is that the new model is derived upon, and merged into the framework of an existing and widely used aerodynamic breakup model. This combined model ensures the simultaneous consideration of the two interacting and competing breakup modes, the flashing breakup and the aerodynamic breakup.

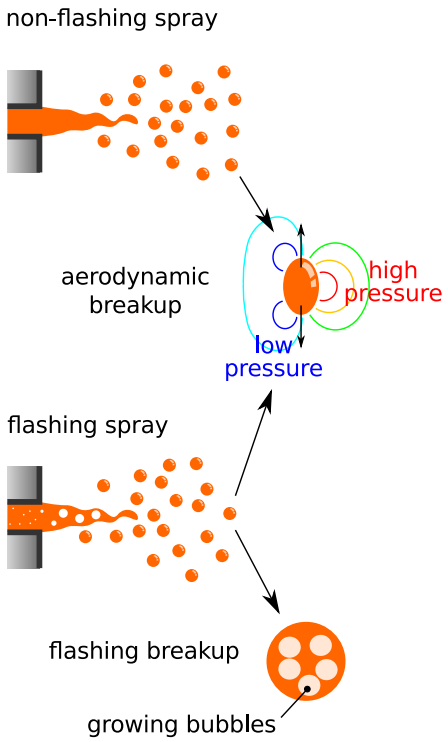

Figure 3.1: The aerodynamic breakup and flashing breakup of liquid jet.

3.1 Combined Model for Flashing and Aerodynamic Droplet Breakup

Flash-boiling of spray consists of three major processes, bubble nucleation, bubble growth, and droplet breakup.

Senda *et al.* [91] developed a unified empirical correlation of the nucleation site density for different liquid fuels upon sudden pressure drop. Senda *et al.* claimed that the model accounts for the trace amount of air dissolved in the liquid fuel, thus the model is categorized as a homogeneous nucleation model [100]. The nucleation model calculates the density of nucleation sites, $\frac{N_b}{V}$, which has the unit of m^{-3},

$$\frac{N_b}{V} = 5.757 \times 10^{12} \exp\left(\frac{-5.279}{\Delta T}\right). \tag{3.1}$$

The number of nucleus due to the sudden pressure drop (and the consequent superheat) is visualized in Fig. 3.2 for droplets of various sizes. As shown, at superheat near 1 K, the number of nucleus rises sharply with superheat. While the number of nucleus progressively saturates with the superheat

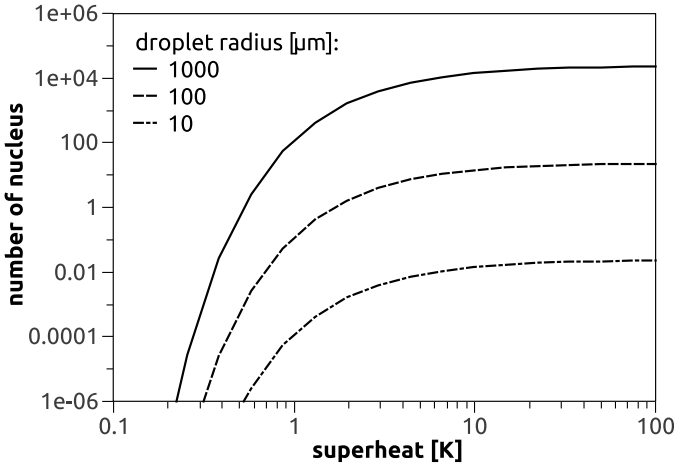

Figure 3.2: The density of nucleation sites upon pressure drop.

beyond 10 K. It is also noticeable that for small droplet with radius less than 0.1 mm, it cannot be guaranteed that nucleation site will emerge in each droplet regardless the magnitude of the superheat.

In the previous flash-boiling models [117, 42, 8], the bubble growth is often calculated by integrating the Rayleigh-Plesset Equation,

$$\rho_l \left[R_b \frac{\mathrm{d}^2 R_b}{\mathrm{d}\, t^2} + \frac{3}{2} \left(\frac{\mathrm{d}\, R_b}{\mathrm{d}\, t} \right)^2 \right] = p_v(T_i) - p_\infty - \frac{2\sigma}{R_b}, \tag{3.2}$$

where R_b is the bubble diameter, $p_v(T_i)$ is the vapor pressure calculated using the bubble-liquid interface temperature, p_∞ is the pressure in the liquid, σ is the surface tension of the liquid. For a bubble that $R_b = \frac{2\sigma}{p_v(T_\infty) - p_\infty}$, and $\frac{\mathrm{d}\, R_b}{\mathrm{d}\, t} = 0$, integrating Eq. 3.2 does not change the state of the bubble. In order to prevent the bubble from staying unchanged or imploding, an artificial disturbance is needed to let the bubble grow. With a disturbance that is sufficiently small, there is a short duration that the bubble is seemingly unchanged before growing. However such initial delay of growth is sensitive to the magnitude of the artificial disturbance [8]. In the spray flash-boiling process, the initial delay is neglected considering the low possibility that the size of the nucleation site coincides with the critical bubble size $R_b = \frac{2\sigma}{p_v(T_\infty) - p_\infty}$. Besides the justification of the artificial disturbance, another challenge to the integration of Eq. 3.2 is its stiffness. The stiffness is due to the fact that the bubble growth is controlled by different effects with different characteristic time scales. The second-order term on the LHS of Eq. 3.2 is the inertia term. The inertia

term can have large contribution to Eq. 3.2 in relatively short duration of time, *i.e.* during the inertia-controlled bubble growth. After the brief inertia-controlled acceleration, the liquid motion of expansion becomes relatively stable and the bubble growth rate becomes more sensitive to other effects, *i.e.* the $p_v(T_i)$ term, where the T_i is often controlled by the heat diffusion from the bulk liquid to the bubble surface. In this case the bubble growth is thermal diffusion controlled, and the inertial effect of the liquid is in quasi equilibrium. But the stability of the numerical integration is still limited by the liquid inertial effect. The artificial disturbance as well as the stiffness issue always exist as long as the initial value problem Eq. 3.2 is to be solved numerically. However both issues can be avoided with adopting an analytical solution of Eq. 3.2. In this research, the bubble growth is modeled using the analytical solution by Mikic *et al.* [64]. Mikic *et al.* developed a unified approximate analytical solution for both inertia-controlled growth (Rayleigh growth) and thermal-diffusion-controlled growth (Plesset-Zwick Theory [77]),

$$\frac{\mathrm{d}\,\hat{R}}{\mathrm{d}\,\hat{t}} = \sqrt{\hat{t}+1} - \sqrt{\hat{t}}, \tag{3.3}$$

$$\hat{R} = \frac{2}{3}\left[(\hat{t}+1)^{\frac{3}{2}} - \hat{t}^{\frac{3}{2}} - 1\right], \tag{3.4}$$

where $\hat{R} = \frac{A}{B^2}R_b$, $\hat{t} = \frac{A^2}{B^2}t$, $A = \sqrt{\frac{2h_{fg}\rho_v\Delta T}{3\rho_l T_{sat}}}$, $B = Ja\sqrt{\frac{12k_l}{\pi\rho_l c_{p_l}}}$, and the Jakob number $Ja = \frac{\Delta T c_{p_l}\rho_l}{h_{fg}\rho_v}$. The bubble growth model is validated against water bubble growth experiment [55]. The comparison between the modeled and measured water bubble growth history is shown in Fig. 3.3, and demonstrates reasonable accuracy.

The bubble growth can eventually cause droplet breakup, for which a breakup criterion is needed. Following the linear stability analysis [117] and previous flash-boiling modeling [42], a void-fraction-based breakup criterion is chosen for flashing breakup of the bubble-droplet system,

$$\epsilon = \frac{V_b}{V_b + V_l} > 0.55. \tag{3.5}$$

In the previous works [117, 8], a flashing breakup model was used independently with an aerodynamic breakup model, the Taylor Analogy Breakup (TAB) model [72]. The TAB model was adjusted for $\epsilon > 0$ [117]. However, in the case of flashing breakup, the aerodynamic effect was

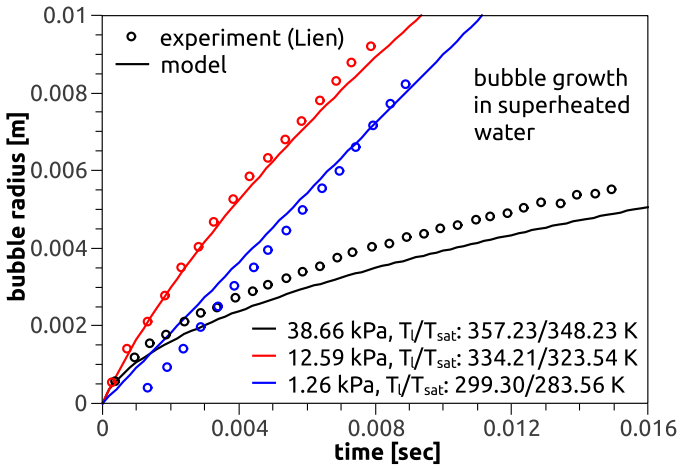

Figure 3.3: The calculated water bubble growth history and measured data [55].

neglected for the calculation of secondary droplet state. In this research, the flashing breakup is formulated within the framework of the TAB model, such that the aerodynamic and superheating effect interact appropriately with each other for all possible cases. In the TAB model, the oscillation of droplet under aerodynamic force is analogous to the oscillation of a spring-mass-damper system,

$$\rho_l R^3 x_{tt} = C_f \rho_g u^2 R^2 - C_k \sigma x - C_d \mu_l R x_t, \tag{3.6}$$

where x is the displacement (perpendicular to the flow direction) of the droplet equator, as shown in Fig. 3.4, the constants $C_f = \frac{1}{3}$, $C_k = 8$, and $C_d = 5$. With bubbles in the droplet, the overall density and viscosity changes, yielding:

$$\left[\epsilon\rho_b + (1-\epsilon)\rho_l\right] R_o^3 x_{tt} = C_f \rho_g u^2 R_o^2 - C_k \sigma x - C_d \left[\epsilon\mu_b + (1-\epsilon)\mu_l\right] R_o x_t, \tag{3.7}$$

where R_o is the outer radius of the bubble-droplet system. The criterion for aerodynamic breakup is:

$$x > C_b R_o, \tag{3.8}$$

where $C_b = \frac{1}{2}$. Using $C_b R_o$ as the length scale, such that $x = C_b R_o \hat{x}$, the breakup criterion becomes $\hat{x} > 1$, and have the non-dimensional equation of motion,

$$\hat{x}_{tt} = \frac{C_f \rho_g u^2}{C_b \left[\epsilon\rho_b + (1-\epsilon)\rho_l\right] R_o^2} - \frac{C_k \sigma}{\left[\epsilon\rho_b + (1-\epsilon)\rho_l\right] R_o^3} \hat{x} - \frac{C_d \left[\epsilon\mu_b + (1-\epsilon)\mu_l\right]}{\left[\epsilon\rho_b + (1-\epsilon)\rho_l\right] R_o^2} \hat{x}_t. \tag{3.9}$$

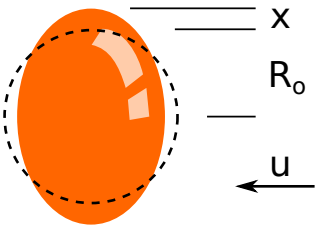

Figure 3.4: A schematic picture of a deformed droplet in the TAB model.

In addition to the droplet velocity before breakup, the secondary droplet has an additional velocity component perpendicular to the original velocity,

$$v_\perp = C_b R_o \hat{x}_t + \frac{3\pi}{16} N_b \frac{R_b^2}{R_o^2} \frac{\mathrm{d}\, R_b}{\mathrm{d}\, t}, \tag{3.10}$$

where the first term is from the original TAB model [72], the second term accounts for the effect of droplet expansion on the momentum in the direction of $v_\perp$. The number and size of secondary droplets are determined by energy balance. The total energy before breakup,

$$E_0 = 4\pi\sigma R_o^2 + 4N_b\pi\sigma R_b^2 + K\frac{4}{5}\pi C_b^2(1-\epsilon)\rho_l R_o^5\left[\hat{x}_t^2 + \frac{C_k\sigma\hat{x}^2}{(1-\epsilon)\rho_l R_o^3}\right] + \frac{2\pi(1-\epsilon)\rho_l N_b^2 R_b^4}{5R_o}\left(\frac{\mathrm{d}\, R_b}{\mathrm{d}\, t}\right)^2, \tag{3.11}$$

where $K = \frac{10}{3}$ is the total oscillation energy divided by the oscillation energy of the primary mode. Compared to the original TAB model, the second term is added to account for the additional surface energy of the bubble-liquid interface, the last term is added to account for the kinetic energy of droplet expansion. The total energy after the breakup follows the original TAB model,

$$E_1 = 4\pi\sigma\frac{(1-\epsilon)R_o^3}{R_{32}} + \frac{2}{3}\pi(1-\epsilon)R_o^3\rho_l v_\perp^2. \tag{3.12}$$

Despite of the identical form of E_1 as in the TAB model, it should be noted that the $v_\perp^2$ now includes the effect of the droplet radial expansion due to bubble growth. Equate E_0 and E_1, solve for the Sauter mean radius (SMR), R_{32}, of the secondary droplets,

$$R_{32} = \left[\frac{1}{(1-\epsilon)R_o} + \frac{N_b R_b^2}{(1-\epsilon)R_o^3} + \frac{KC_b^2\rho_l R_o^2\hat{x}_t^2}{5\sigma} + \frac{KC_b^2 C_k\hat{x}^2}{5(1-\epsilon)R_o} + \frac{N_b^2\rho_l R_b^4}{10R_o^4\sigma}\left(\frac{\mathrm{d}\, R_b}{\mathrm{d}\, t}\right)^2 - \frac{\rho_l v_\perp^2}{6\sigma}\right]^{-1}. \tag{3.13}$$

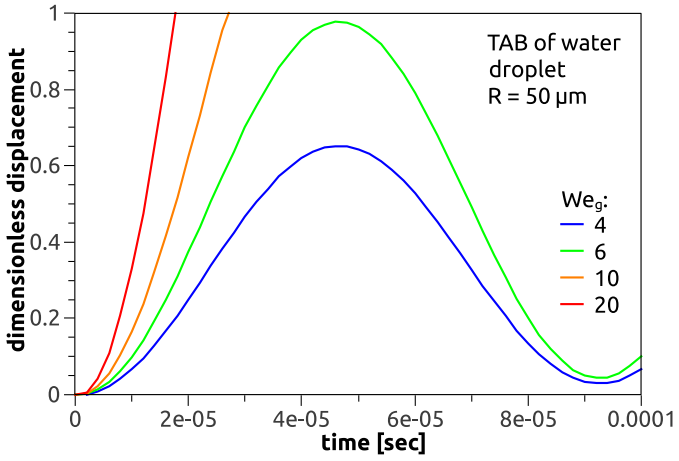

Figure 3.5: The droplet deformation $\hat{x}$ upon aerodynamic load of different Weber numbers.

3.2 Single Droplet Breakup

With the unified TAB-flashing model, the aerodynamic breakup of non-superheated droplet and "blob" is calculated in a way equivalent to the original TAB model. The un-damped TAB equation of motion results in a critical Weber number ($We_g = \frac{2R_o\rho_g u^2}{\sigma}$) of 6. With the viscous damping of the droplet, $We_g = 6$ is still stable. The evolution of the normalized deformation $\hat{x}$ is plotted in Fig. 3.5 for different Weber numbers. With low superheat, the TAB happens faster than the flashing breakup, and the existence and growth of bubbles reduce the TAB breakup time, increase the perpendicular velocity and the number of the secondary droplets, as shown in Fig. 3.6 to 3.8. With high superheat, flashing breakup happens before the aerodynamic breakup. The breakup time decreases rapidly with increasing the superheat. The broaden of spray angle due to a single flashing breakup event is not definitive, as non-monotonic behavior is observed in Fig. 3.7. However Fig. 3.7 indicates higher possibility of increased spray dispersion angle as the result of superheating. The secondary droplet size and number are also not definitive for a single flashing breakup event, as shown in Fig. 3.8. In a superheated spray event, the consecutive breakups are possible and the spray undergoes strong evaporation. These effects are not included in the result shown in Fig. 3.6 to 3.8. It is expected that the spray dispersion angle can be further increased due to the consecutive breakups, and the strong evaporation is likely to result in smaller droplet size distribution. The TAB-flashing breakup model and the droplet evaporation model need to be integrated into a CFD program for further evaluation of the spray superheating effects.

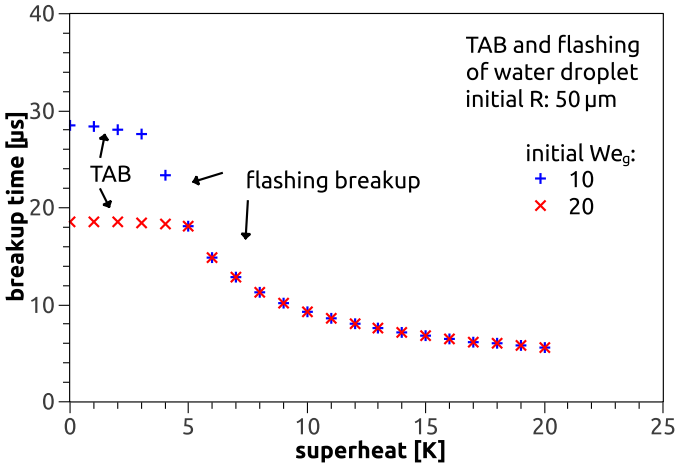

Figure 3.6: The TAB and flashing breakup time of superheated water droplet.

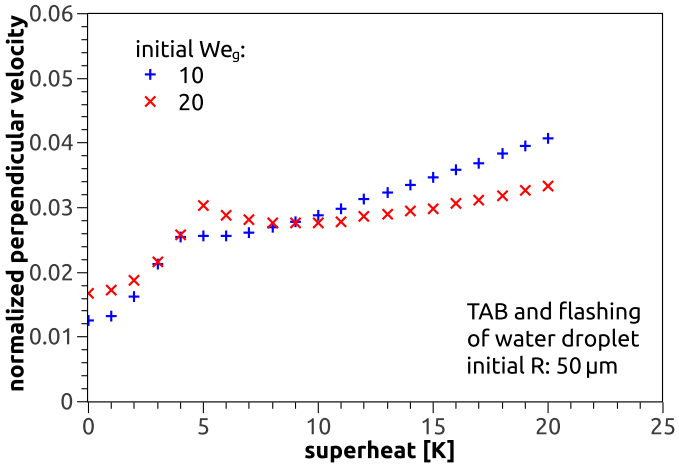

Figure 3.7: The perpendicular secondary droplet velocity normalized by the original droplet velocity, *a.k.a.* the tangent of the spray half cone angle, of the TAB and flashing breakup.

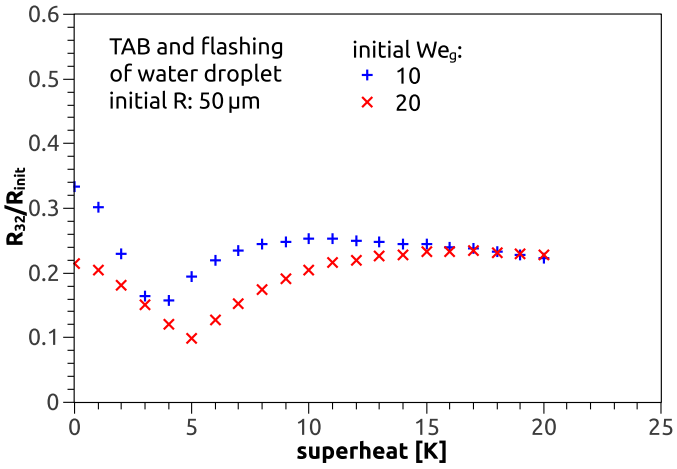

Figure 3.8: The SMR of the secondary droplet normalized by the original droplet upon TAB and flashing breakup.

3.3 Flashing Spray Simulation

In order to study the effect of flash-boiling in sprays, the single droplet breakup model developed in the present study is integrated into the KIVA program to calculate the aerodynamic and flashing breakup of each Lagrangian parcel.

3.3.1 Flashing and Non-Flashing N-Heptane Spray

The spray examined in this study is a hollow-cone n-heptane spray from a typical early generation GDI injector with cone angle of 64°. In the experiments [112], the rail pressure is held at 3 to 4 bar above the ambient gas pressure, which is 0.25 bar for the flashing case and 6 bar for the non-flashing case. The liquid flow rate is estimated to be 3.3 mg/ms, which matches the calibration [112] of the tested injector. The estimation of the spray velocity is based on both momentum conservation and mass conservation,

$$u_{spray} = C_D \sqrt{\frac{2\Delta p}{\rho}}, \tag{3.14}$$

$$u_{spray} = \frac{\dot{m}}{C_A A_{nozzle} \rho}. \tag{3.15}$$

With the typical values for the discharge coefficient $C_D = 0.55$, and area coefficient $C_A = 0.95$, both momentum conservation and mass conservation are satisfied and the liquid velocity upon

injection is estimated to be 19 m/s for the flashing and non-flashing case. For the non-flashing case, the fuel temperature is kept at 303 K, while it is raised to 353 K for the flashing case. For both cases, the ambient gas is 100% nitrogen, and has temperature of 410 K, and 323 K for the non-flashing and flashing case, respectively. The simulation assumes axial symmetry and uses a 2-D computational grid that represents a closed cylindrical chamber. During the simulated time of 3 ms, continuous injection is applied. The early generation GDI injector used in the test generates the hollow-cone spray using a swirl-atomizer mechanism. A character of such mechanism is that the liquid is not always constrained to exit at the design spray cone angle, 64° in this case. In order to compensate for this fact, the initial velocity direction of the Lagrangian parcels is broaden and dispersed in the case of flashing simulation to generate broader and thicker flashing spray from the swirl-atomizer mechanism. Such adjustment is not applied in the non-flashing case where the GDI injector operates at its common operation condition.

Apart from the combined aerodynamic and flashing breakup model developed in this study, the droplet evaporation model described in Chap. 2 is also used to calculate the vaporization of the liquid, under both flashing and non-flashing conditions.

In order to compare the simulation result with the high speed images obtained from spray experiment, synthetic light blockage images are generated based on the 2-D simulation result. The KIVA's 2-D simulation is accomplished by using a single layer of FVM cells with the width of 0.5°. The result of the thin sector is copied and revolved to generated an extended series of Lagrangian parcels, which are projected onto a vertical observation plane. For each of the original and copied parcels, its location is disturbed within a small cubical volume to account for the fact that each parcel represents a number of droplets distributed in the vicinity of the parcel. The light blockage of each pixel on the observation plane is proportional to the summation of the radius cubed of all droplets projected in such pixel divided by the physical area of the pixel. The comparisons between the simulation results and the experimental high speed images are shown in Fig. 3.9 and 3.10. The pattern of the horizontal lines in the droplet light blockage images indicates axial symmetry, which is the result of the thin sector data copying and revolving. The horizontal pattern is smeared due to the random disturbance of the Lagrangian parcel location. Rendered in the 2-D region is the fuel mass fraction in the gas phase. The solid curve represents the isobar of $Y_{fuel} = 0.01$.

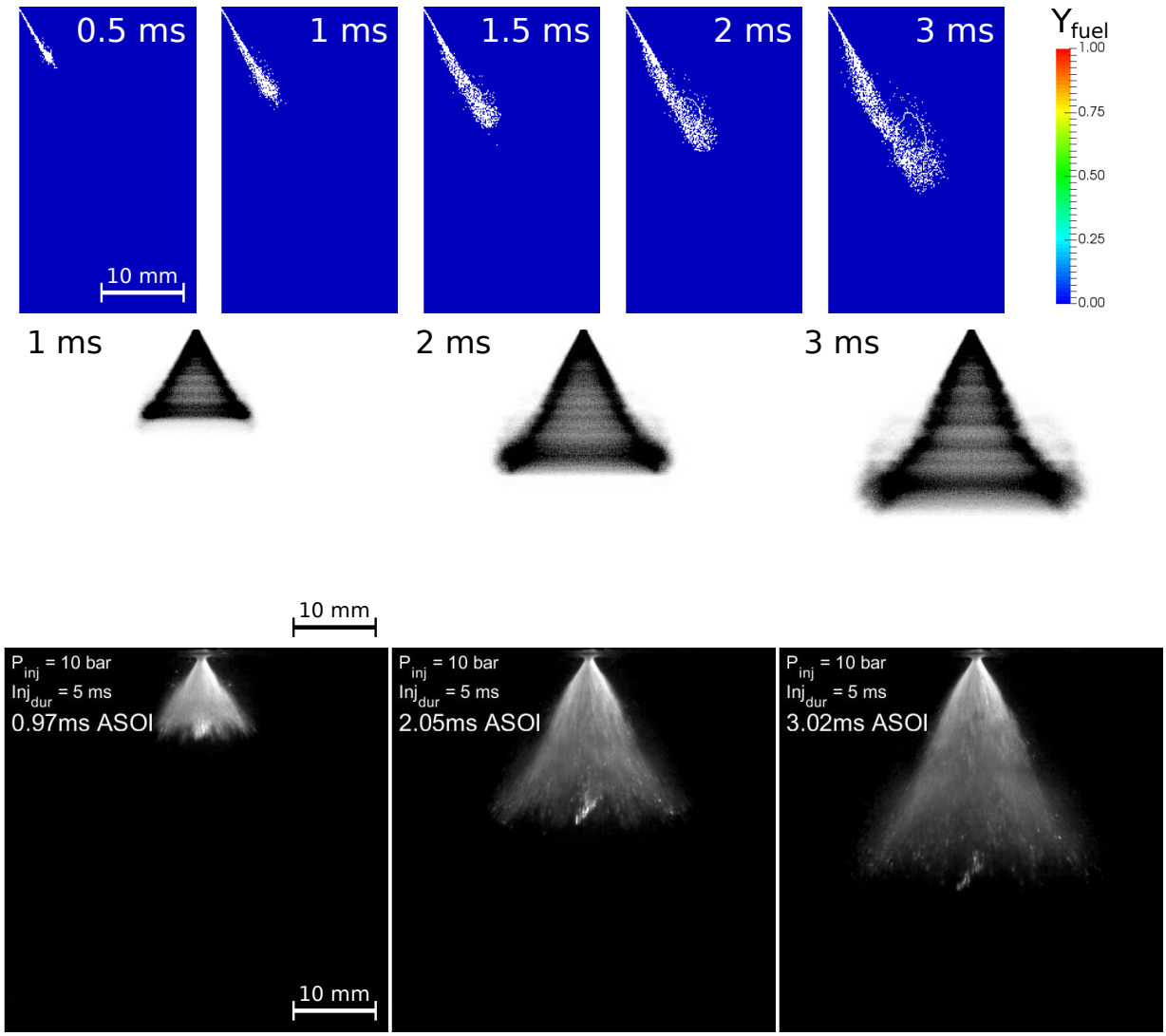

Figure 3.9: The Lagrangian parcels and the fuel mass fraction in a non-flashing hollow-cone spray 2-D simulation (top row), and the synthetic droplet light blockage images (middle row). For comparison are the high speed images in the same scale [112] (bottom row).

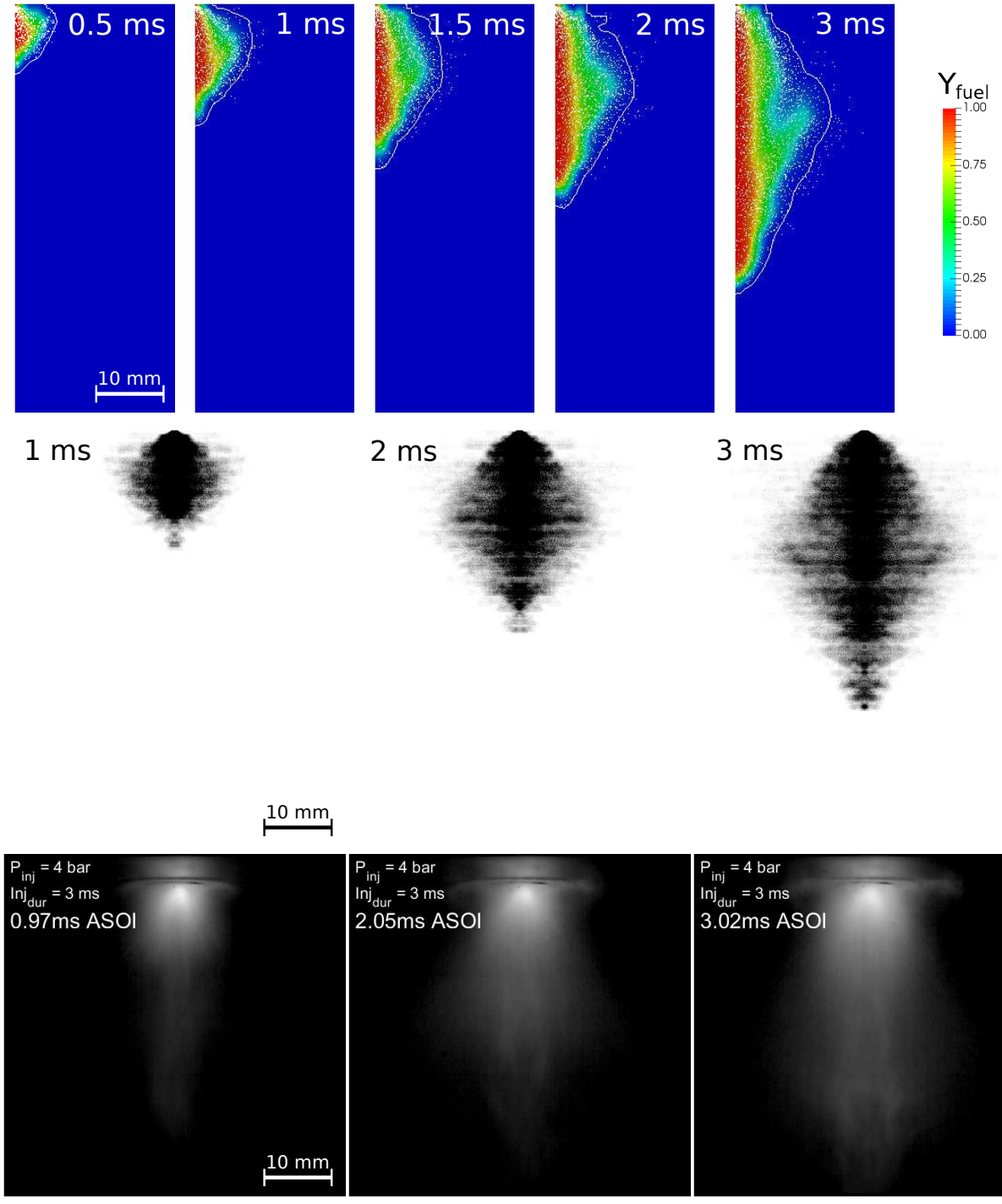

Figure 3.10: The Lagrangian parcels and the fuel mass fraction in a flashing hollow-cone spray 2-D simulation (top row), and the synthetic droplet light blockage images (middle row). For comparison are the high speed images in the same scale [112] (bottom row).

As shown in Fig. 3.9, the spray under non-flashing condition maintains the conical structure through the 3 ms tested duration, in both the prediction and the experiment. The predicted spray penetration is slightly shorter comparing to the high speed images. Such slight difference is believed to be caused by the error in the estimation of the liquid speed, as well as the insufficient camera-object distance and the subsequent image distortion. At around 1 ms to 2 ms after SOI, both prediction and observation show the development of an inward drifting motion of the droplets, which results in the turning droplet streak found in both the prediction and the experiment. Another interesting phenomenon observed in the experiment but not captured in the simulation is the cluster of large droplets generated in the early stage of the injection and traveling near the center of the cone axis. This is due to the fact that the swirl atomizer mechanism does not always constrain the direction of the exiting liquid. In the beginning of the injection, when the spray momentum is ramping-up, the liquid detaches from the conical nozzle surface and forms the cluster of large droplets found near the axis of the injector.

As shown in Fig. 3.10, the flashing spray can no longer maintain the conical structure and becomes a wide-spreading mist. The dispersion of spray is due to two effects: the lack of direction constraint by the swirl atomizer mechanism, and the flashing-breakup-induced secondary droplet velocity deviation. The first effect is compensated by the adjustment of spray cone angle and thickness, and the second effect is accounted for with the combined flashing and aerodynamic breakup model. Due to the lower ambient gas density comparing to the non-flashing case, the spray penetration in the vertical direction is considerably higher in the flashing case. Another feature of the flashing spray is the high local fuel concentration in the gas phase. Due to the excessive thermal energy contained in the superheated liquid, the phase transition happens rapidly and is able to rise the fuel mass fraction up to 100% near the core region of the spray, which cannot be achieved without heating the liquid to the saturation temperature.

In both flashing and non-flashing cases, the simulation result matches reasonably well with the high speed images in term of spray structure and size. As comparing the simulation result against the high-speed images, another thing should be noticed is that the simulation visualizations are instantaneous snapshots, while the high-speed images are time-averages through the shutter duration, which is 0.11 ms in this case.

In order to further validate the combined TAB/flashing breakup model and its integration into KIVA, as well as to study the spray behavior with elevating the liquid temperature across the saturation point, an additional series of hollow-cone spray experiments [112] are simulated. In the tests, the nitrogen pressure is fixed at 0.25 bar, under which the saturation temperature of n-heptane is 330 K, approachable by liquid preheating. The nitrogen temperature is kept at 323 K, below the saturation temperature of n-heptane. The rail pressure is held at 3 to 4 bar above the ambient nitrogen pressure. Four n-heptane temperatures across the saturation point are tested: 323, 333, 343, and 353 K. With the same GDI injector as used in the tests visualized by Fig. 3.9 and 3.10, the injection flow rate and speed are assumed to be 3.3 mg/ms and 19 m/s, respectively. Adjustment of the spray cone angle and thickness is applied for all the superheated cases in order to account for the swirl atomizer's lack of spray direction constraint and to match with the high speed images. The injection event spans the tested duration of 3 ms. Due to the low gas density and drag, the spray tip travels beyond the field of view in the experimental setup sooner than 3 ms.

The simulation result as well as high speed images are shown from Fig. 3.11 to 3.16. In the beginning of the injection, captured by Fig. 3.11, the near-axis liquid cluster is found in the experiment with all the tested liquid temperatures. In the simulation, only the case with the highest superheat, 23 K, has Lagrangian parcels near the axis. As explained previously, the near-axis liquid cluster is not captured by simulation in other cases. The large adjustment of spray cone angle and thickness for the case with the highest superheat essentially transforms the spray from a hollow-cone spray into a solid-cone spray, distributing Lagrangian parcels near the cone axis.

From around 1 ms (shown in Fig. 3.12) and afterward, the spray is seen developed the conical structure in the experiment. With the liquid temperature below the saturation temperature, the spray maintains a crisp conical structure in both experiment and simulation. And in this case the maximum vapor concentration can be very close to 1 but cannot reach 1, as seen in the top rows of Fig. 3.11 to 3.16.

With the liquid temperature at 3 K above the saturation temperature, the conical structure is still reasonably clear, but not as crisp as the non-superheated case. The synthetic droplet light blockage images show rougher edge along the cone surface comparing to the non-superheated case.

This matches well with the smeared cone boundary found in the experimental high speed images. Unlike the non-superheated case, the vapor is saturated in a small region near the injector exit. The maximum vapor concentration reaches 1 in such region as shown in the top rows of Fig. 3.11 to 3.16.

Further heating the liquid to 13 K above the saturation temperature, the conical shape becomes increasingly unstable. With the fast phase transition from liquid to gas, the momentum exchange between the two phases is also enhanced. Gas phase gains speed rapidly due to the momentum carried by the vapor generated at the droplet surface, results in strong shear effect and pronounced instability, disturbing the otherwise regular conical shape. As the result, the 13 K superheat case has rougher and more smeared cone edge in the synthetic droplet light blockage images as well as the experimental high speed images comparing to the 3 K superheat case. Also the fuel-saturated region can be found further away from the injector exit as well.

The maximum tested superheat of 23 K results in drastic flashing behavior. The conical structure is hardly recognizable and the spray turns into a wide-spreading mist. The fuel vapor is distributed in a larger region. The volume of saturated fuel vapor is also significantly enlarged. The violent flash-boiling of the superheated spray is potentially beneficial to the mixture preparation targeting homogeneous fuel-air mixture.

The simulation of the flashing and non-flashing spray demonstrates the usefulness of the combined TAB/flashing breakup model in the mixture preparation calculation of conventional engine, as well as in the development of the new engine concept exploiting flash-boiling to generate homogeneous mixture.

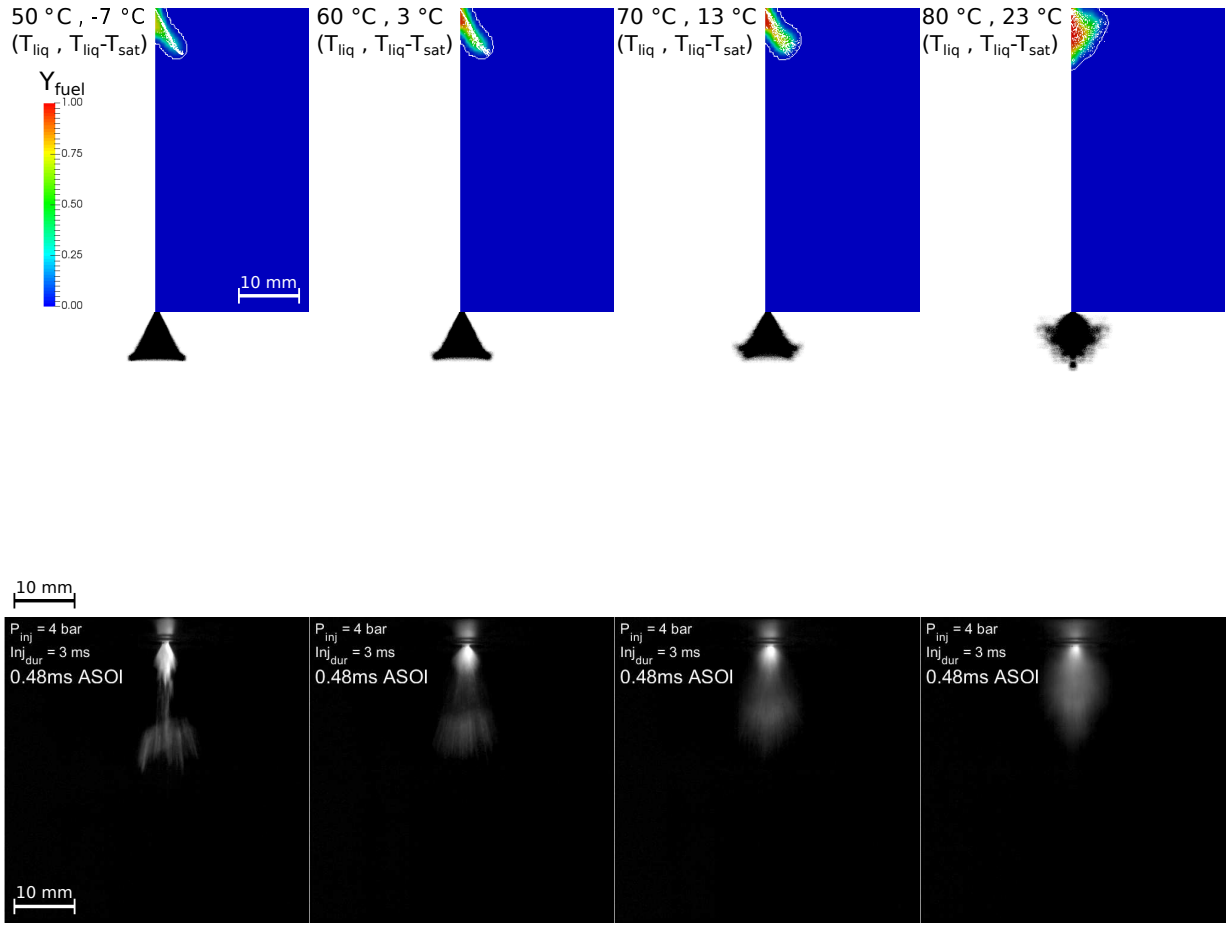

Figure 3.11: The Lagrangian parcels and the fuel mass fraction in hollow-cone spray 2-D simulations (top row), and the synthetic droplet light blockage images (middle row). For comparison are the high speed images in the same scale [112] (bottom row). The snapshot for different liquid temperatures are taken at 0.5 ms after SOI.

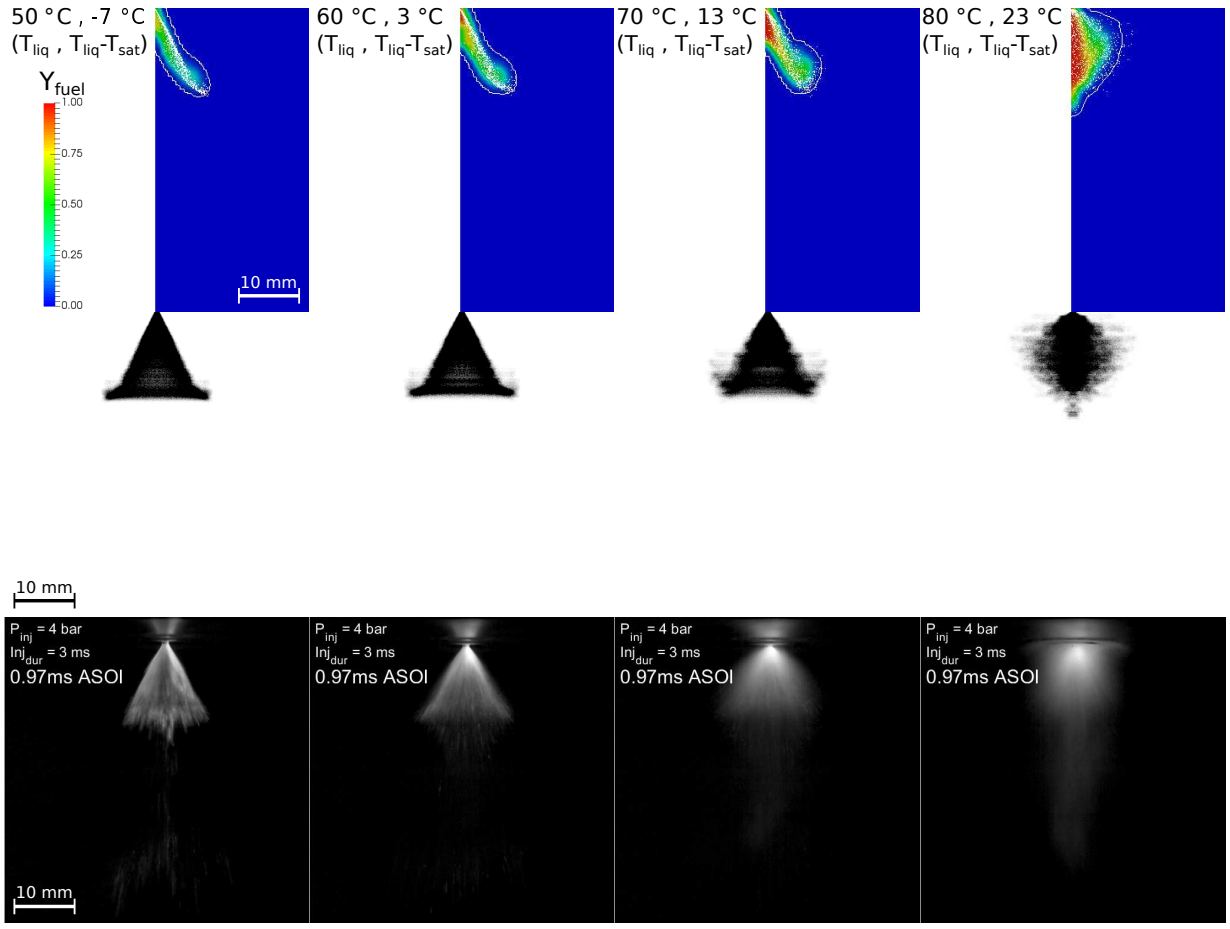

Figure 3.12: The Lagrangian parcels and the fuel mass fraction in hollow-cone spray 2-D simulations (top row), and the synthetic droplet light blockage images (middle row). For comparison are the high speed images in the same scale [112] (bottom row). The snapshot for different liquid temperatures are taken at 1.0 ms after SOI.

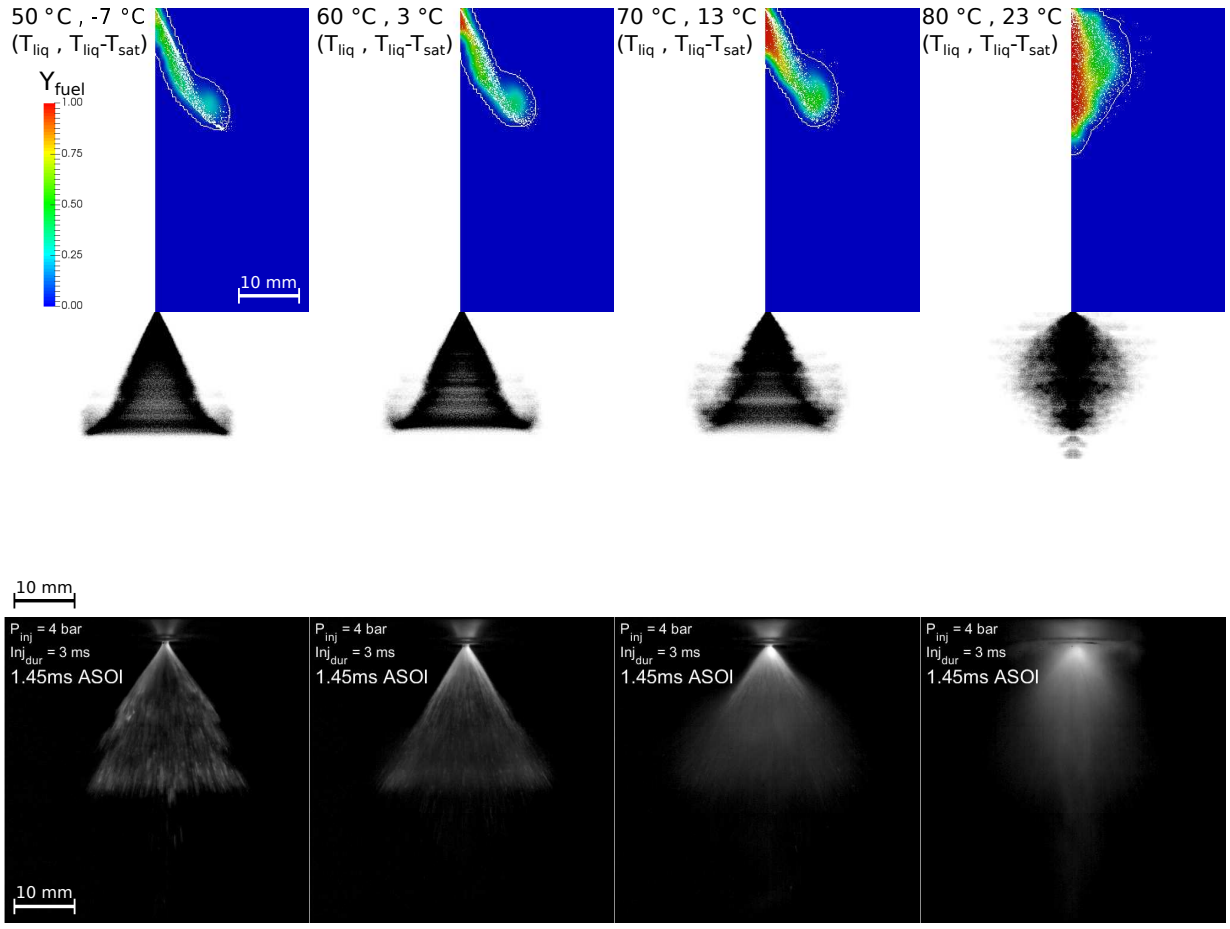

Figure 3.13: The Lagrangian parcels and the fuel mass fraction in hollow-cone spray 2-D simulations (top row), and the synthetic droplet light blockage images (middle row). For comparison are the high speed images in the same scale [112] (bottom row). The snapshot for different liquid temperatures are taken at 1.5 ms after SOI.

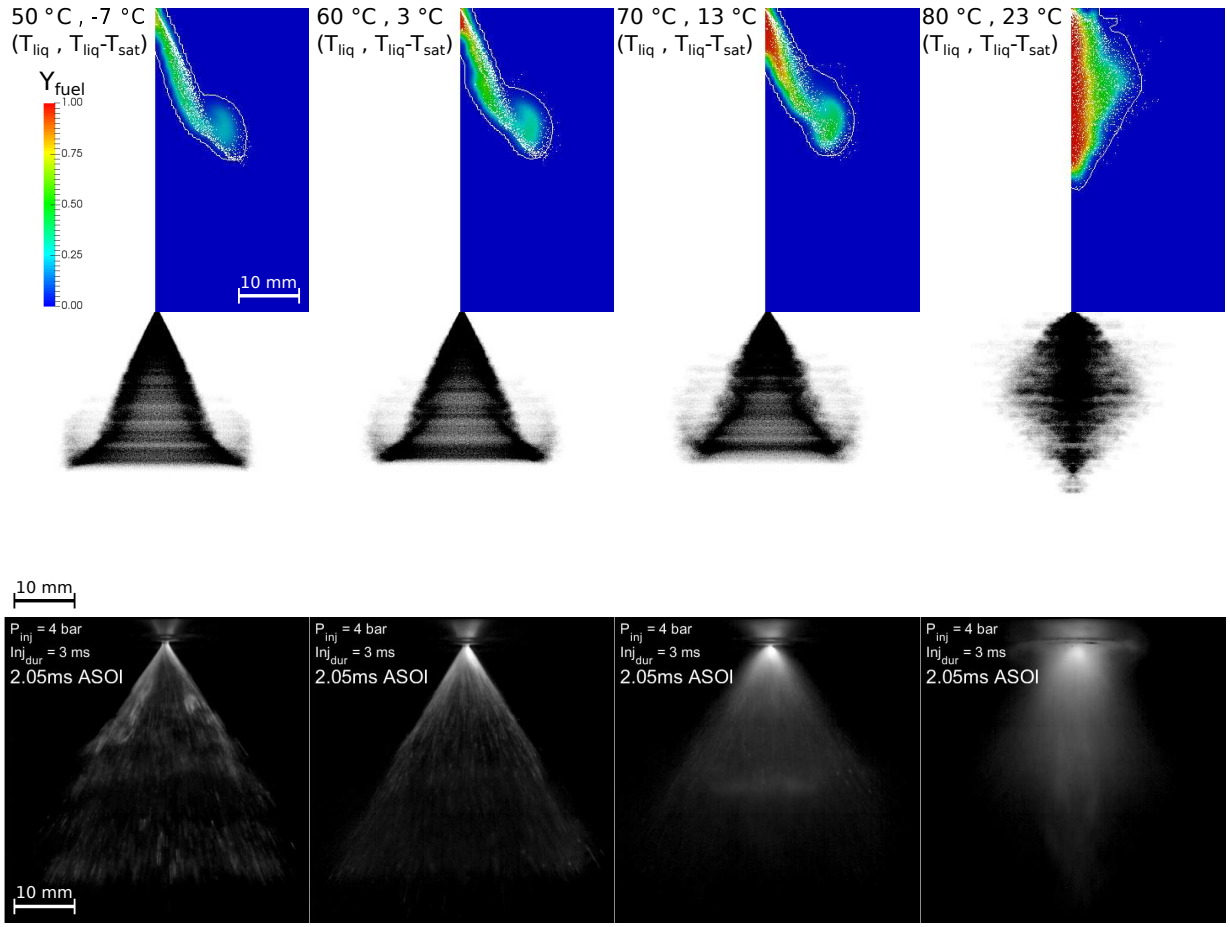

Figure 3.14: The Lagrangian parcels and the fuel mass fraction in hollow-cone spray 2-D simulations (top row), and the synthetic droplet light blockage images (middle row). For comparison are the high speed images in the same scale [112] (bottom row). The snapshot for different liquid temperatures are taken at 2.0 ms after SOI.

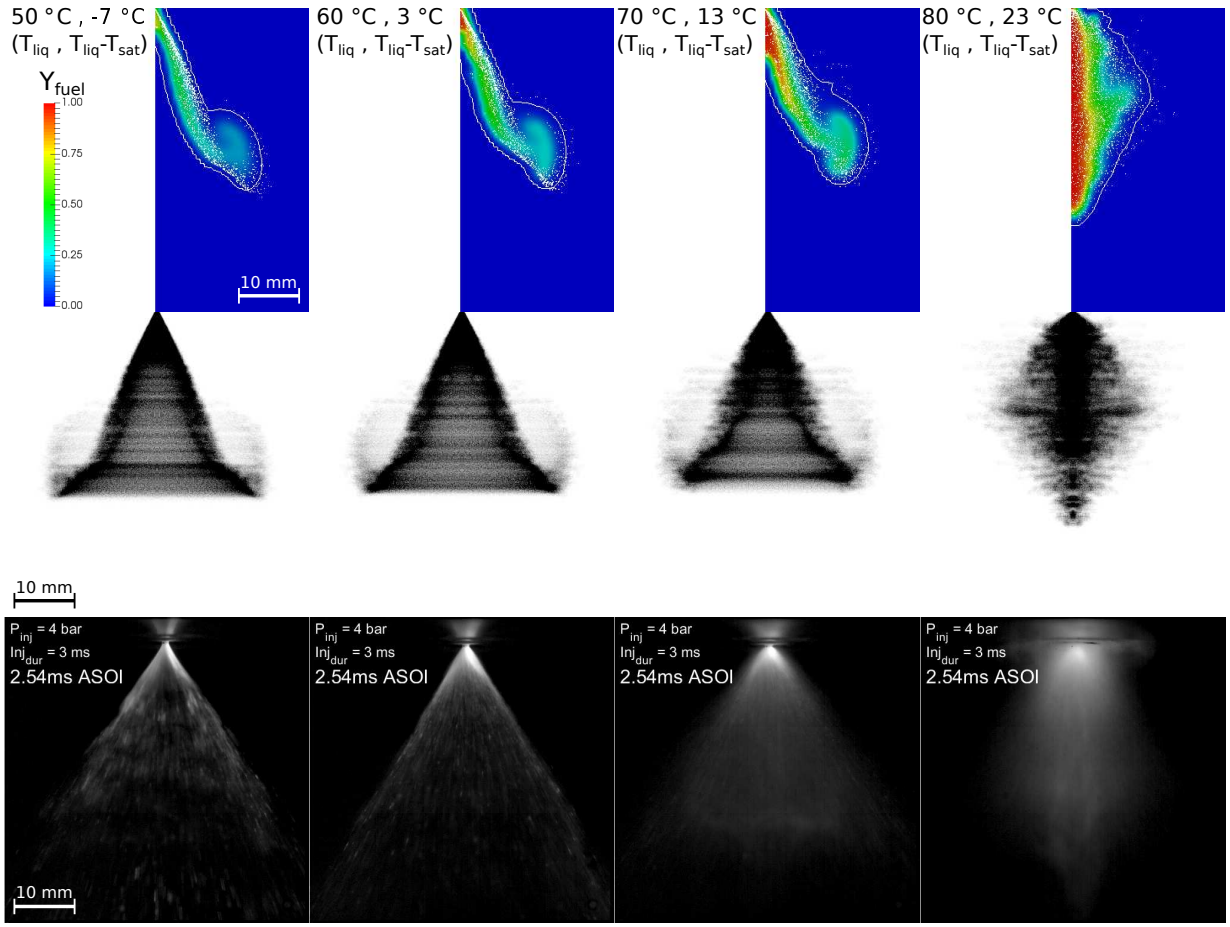

Figure 3.15: The Lagrangian parcels and the fuel mass fraction in hollow-cone spray 2-D simulations (top row), and the synthetic droplet light blockage images (middle row). For comparison are the high speed images in the same scale [112] (bottom row). The snapshot for different liquid temperatures are taken at 2.5 ms after SOI.

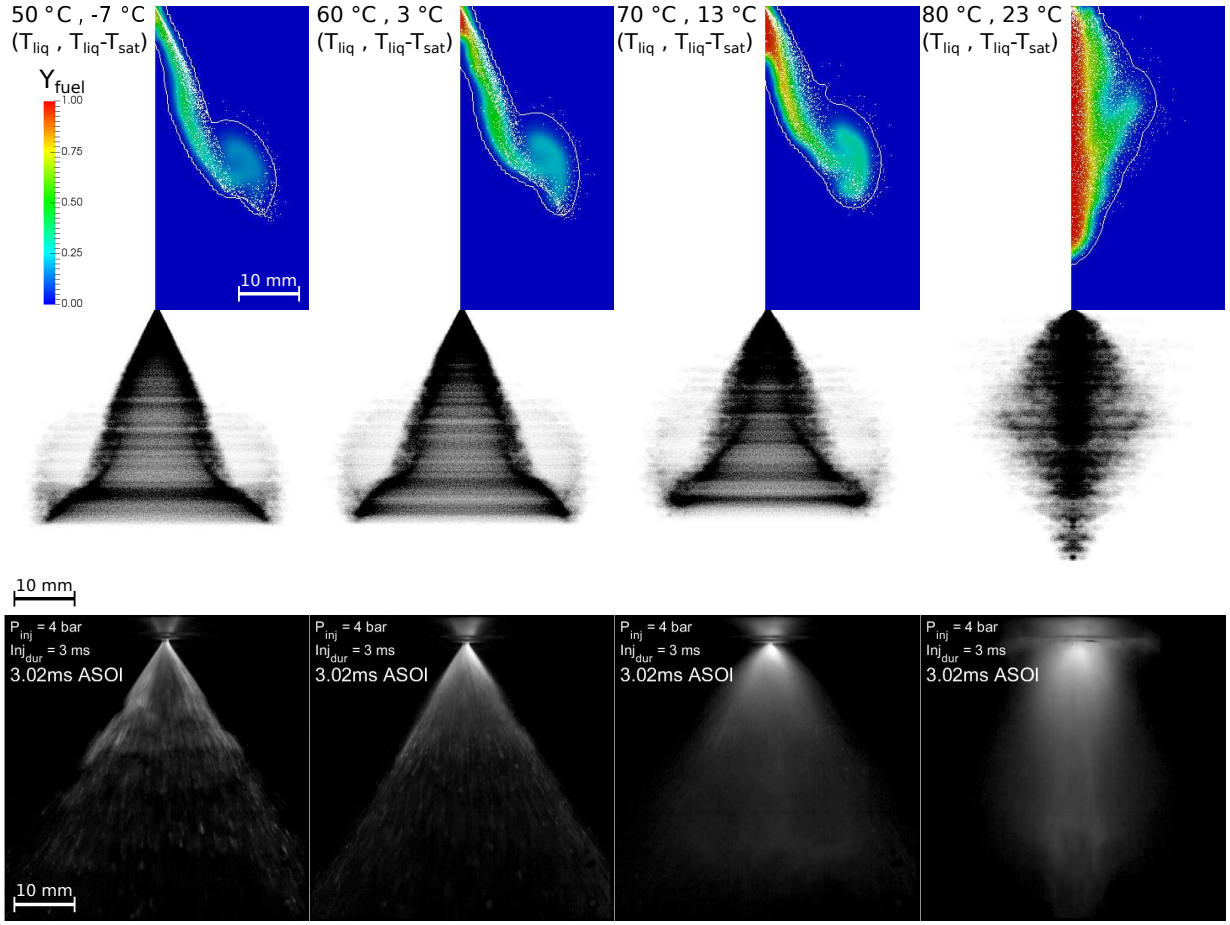

Figure 3.16: The Lagrangian parcels and the fuel mass fraction in hollow-cone spray 2-D simulations (top row), and the synthetic droplet light blockage images (middle row). For comparison are the high speed images in the same scale [112] (bottom row). The snapshot for different liquid temperatures are taken at 3.0 ms after SOI.

Chapter 4

CI Engine Simulation and Chemical Kinetics

4.1 Efficient Chemical Kinetics Solver

In CI engine operation, mixture preparation interacts with chemical kinetics and affects the spontaneous ignition of the fuel-air mixture. In CFD simulation of CI engine, the local chemical kinetics problem in the computational cell is often solved as a lumped system of homogeneous mixture. The homogeneous local system is assumed to be adiabatic and has a constant volume during the calculation of chemical reactions. The mathematical formulation of the combustion reaction kinetics in such a system is in the form of an initial value problem. Considering such a problem with n_{sp} possible species and n_{rxn} possible reactions, a system of $n_{sp}+1$ ODEs is used to describe the problem,

$$\begin{cases} \dfrac{\mathrm{d}\,Y_i}{\mathrm{d}\,t} = \dfrac{\tilde{M}_i}{\rho_{tot}} \displaystyle\sum_{\mathrm{rxn}\ m} S_{im}\left(r_m^f - r_m^b\right) \\ \dfrac{\mathrm{d}\,T}{\mathrm{d}\,t} = -\dfrac{1}{c_{vtot}} \displaystyle\sum_{\mathrm{sp}\ i} u_i \dfrac{\mathrm{d}\,Y_i}{\mathrm{d}\,t} \end{cases}, \tag{4.1}$$

where Y_i is the mass fraction of species i; T is the temperature of the mixture; $\tilde{M}_i$ is the molar mass of species i; ρ_{tot} and c_{vtot} are the overall density and overall constant-volume heat capacity, respectively; u_i is the mass-specific internal energy; r_m^f and r_m^b are the forward and backward volumetric reaction rates of the reaction m, modeled by the law of mass action with Arrhenius-type expression; $\mathbf{S} \in \mathbb{N}^{n_{sp}\times n_{rxn}}$ is the stoichiometric matrix and S_{im} is the stoichiometric number of species i in reaction m.

The task of a chemical kinetics solver in CFD is to solve the initial value problem expressed as Eq. 4.1 with the given initial Y_is and T. Extensive efforts have been made to reduce the computational cost to solve such problems in CFD by simplifying the problem. Approaches of problem simplification are based on size reduction [59, 54], stiffness removal [58], and intrinsic lower-

dimensional manifold (ILDM) attraction [60]. An efficient chemical kinetics solver is developed in this study for CI engine CFD applications [106]. The solver reduces the computation time without simplifying the problem.

In the chemical kinetics computation, the r_m^f, r_m^b, and $\sum_{\text{rxn } m} S_{im}\left(r_m^f - r_m^b\right)$ are efficiently evaluated using proven thermo-chemistry packages such as CANTERA [31]. In such packages, r_m^f and r_m^b can be in simple modified Arrhenius form, as well as in the form of third-body reaction, pressure-dependent reaction, Lindemann's formulation, Troe's formulation, *etc.* The ODE system described by Eq. 4.1 is often solved by backward differentiation formulas (BDF) scheme with Newton iterations. In this research the author selected SUNDIALS-CVODE [17], a proven and efficient implementation of variable order and variable step size BDF, as the framework to solve the stiff ODE system of reaction kinetics. In the Newton iterations, the Jacobian matrix of Eq. 4.1 needs to be evaluated and inverted. A commonly used method is to evaluate the Jacobian matrix by numerical differentiation with respect to each of the $n_{sp}+1$ dimensions of the state space, then factor and solve the Jacobian matrix using a dense matrix solver. In this study, numerical methods are developed based on an approximated semi-analytical Jacobian matrix which takes far less time to evaluate comparing to the numerical Jacobian matrix. For problems of different sizes, the approximate semi-analytical Jacobian matrix is either solved by a direct dense solver or is used to construct a preconditioner for a Krylov subspace solver. The direct dense method with semi-analytical Jacobian is tailored for small reaction mechanisms, *i.e.* $n_{sp} < 100$, and the preconditioned Krylov method is applicable for larger reaction mechanisms.

The Jacobian matrix $\mathbf{J} \in \mathbb{R}^{(n_{sp}+1)\times(n_{sp}+1)}$ for the system of Eq. 4.1 is:

$$\mathbf{J} = \begin{bmatrix} \frac{\partial}{\partial Y_j}\left(\frac{\mathrm{d}\,Y_i}{\mathrm{d}\,t}\right) & \frac{\partial}{\partial T}\left(\frac{\mathrm{d}\,Y_i}{\mathrm{d}\,t}\right) \\ \\ \frac{\partial}{\partial Y_j}\left(\frac{\mathrm{d}\,T}{\mathrm{d}\,t}\right) & \frac{\partial}{\partial T}\left(\frac{\mathrm{d}\,T}{\mathrm{d}\,t}\right) \end{bmatrix}. \tag{4.2}$$

For each of the four parts, we need an efficient method to evaluate the values for a given state.

The block $\frac{\partial}{\partial Y_j}\left(\frac{\mathrm{d}\,Y_i}{\mathrm{d}\,t}\right) \in \mathbb{R}^{n_{sp}\times n_{sp}}$ is evaluated analytically with neglecting all third-body effects:

$$\frac{\partial}{\partial Y_j}\left(\frac{\mathrm{d}\,Y_i}{\mathrm{d}\,t}\right) = \frac{\tilde{M}_i}{\rho_{tot} Y_j} \sum_{\text{rxn } m} S_{im}\left(\nu'_{jm} r_m^f - \nu''_{jm} r_m^b\right), \tag{4.3}$$

where $\nu'_{jm} = -\min\{S_{jm}, 0\}$, and $\nu''_{jm} = \max\{S_{jm}, 0\}$ are the positive stoichiometric numbers of species j in reaction m as a reactant and a product, respectively. In this work the forward and backward reaction rates r^f_m and r^b_m are evaluated using CANTERA [31]. The computation cost of evaluating r^f_m and r^b_m, for all species and reactions in total, roughly equals to the cost of only one RHS functional evaluation of the ODE system, compared to $n_{sp}+1$ RHS evaluations to construct the $\frac{\partial}{\partial Y_j}\left(\frac{\mathrm{d}\,Y_i}{\mathrm{d}\,t}\right)$ block numerically.

The row vector $\frac{\partial}{\partial Y_j}\left(\frac{\mathrm{d}\,T}{\mathrm{d}\,t}\right) \in \mathbb{R}^{n_{sp}}$ is also evaluated analytically:

$$\frac{\partial}{\partial Y_j}\left(\frac{\mathrm{d}\,T}{\mathrm{d}\,t}\right) = -\frac{c_{vj}}{c_{vtot}}\frac{\mathrm{d}\,T}{\mathrm{d}\,t} - \frac{1}{c_{vtot}}\sum_{\mathrm{sp}\ i} u_i \frac{\partial}{\partial Y_j}\left(\frac{\mathrm{d}\,Y_i}{\mathrm{d}\,t}\right), \tag{4.4}$$

where c_{vj} is the constant-volume mass-specific heat capacity of pure species j. The underlying mixing rule for heat capacity is $c_{vtot} = \sum_{\mathrm{sp}\ j} c_{vj} Y_j$. In Eq. 4.4, the result of $\frac{\partial}{\partial Y_j}\left(\frac{\mathrm{d}\,Y_i}{\mathrm{d}\,t}\right)$ is reused from the evaluation of the upper-left block, hence no additional RHS evaluation is needed. It should be noted that Eq. 4.4 fails at $Y_j = 0$. In simulation, discontinuity of the Jacobian matrix across $Y_j = 0$ causes numerical instability. In order to have a numerically stable method, two special treatments of the Y_j lower limit are used: a) in the RHS formulation, negative Y_js having magnitude smaller than the absolute tolerance are permitted; b) (only) in the Jacobian evaluation, the Y_js are bounded by a positive lower limit smaller than the absolute tolerance.

The analytical formulation of the right-most column $\frac{\partial(\cdot)}{\partial T} \in \mathbb{R}^{n_{sp}+1}$ of the Jacobian matrix given in [75] requires detailed rate expression and Arrhenius constants for each reaction. And the cost of evaluating the analytical expressions is similar to one RHS evaluation. Due to the complexity of the analytical formulation, this work follows the suggestion by [109] and evaluates the $\frac{\partial(\cdot)}{\partial T}$ column by numerical differentiation:

$$\frac{\partial \mathbf{\Phi}}{\partial T} = \frac{\mathbf{\Phi}(\{Y_i\}, T+\Delta T) - \mathbf{\Phi}(\{Y_i\}, T)}{\Delta T} + \mathrm{H.O.T.}, \tag{4.5}$$

where $\mathbf{\Phi}$ represents the RHS function of the ODE system and ΔT is a finite disturbance in temperature.

Equation 4.2 to 4.5 provide an efficient semi-analytical approximation of the Jacobian matrix. With the semi-analytical formulation, the total number of equivalent RHS evaluations required to

construct the Jacobian matrix is reduced to two from $n_{sp}+2$ of the complete numerical construction of the Jacobian matrix.

The assembled Jacobian matrix can be inverted by a linear solver. This work chooses the dense LU decomposition method as the linear solver for the direct method. The direct method is primarily designed for small problems, *i.e.* $n_{sp} < 100$. These small problems often have a Jacobian matrix with sparsity well below 1. Due to the overhead and inefficient vectorization of sparse data structure, the sparse LU solver is slower than the dense LU solver in the cases with small problem size and low sparsity.

It should be noted that for the Newton method, the Jacobian matrix does not need to be exact. A good estimation of the Jacobian matrix still has a great chance to converge due to the iterative nature of the Newton method. In the successful implementations of Newton-based implicit ODE solver, the Jacobian is commonly reused, and updated only when Newton iterations have convergence difficulties. This fact makes it possible to further simplify the Jacobian matrix formulation without deteriorating the stability and accuracy.

For large mechanisms, this work adopts a preconditioned generalized minimal residual (GMRES) method [86], one of the most stable and widely used Krylov subspace methods, to solve the linear system involved in Newton iteration. Krylov subspace methods are inherently Jacobian-free, meaning instead of requiring the full evaluation of the Jacobian matrix, the Krylov subspace methods only need to evaluate the Jacobian-vector product, which can be efficiently evaluated by one operation of numerical differentiation aligned with a given vector. It is widely known that the performance of Krylov subspace methods can be significantly improved by applying a preconditoner. By applying a (left, which is the choice of this study) precondtioner, a linear problem $\mathbf{Ax} = \mathbf{b}$ is replaced by the preconditioned problem $\mathbf{P}^{-1}\mathbf{Ax} = \mathbf{P}^{-1}\mathbf{b}$, where $\mathbf{P}$ is the preconditioning matrix. In order to apply the preconditoner, one needs to solve the preconditioning problem:

$$\mathbf{Pz} = \mathbf{r}, \tag{4.6}$$

for given residual $\mathbf{r}$. One can choose a $\mathbf{P}$ such that the preconditioned problem converges fast with the chosen Krylov subspace method. It is clear that if $\mathbf{P} = \mathbf{A}$ is chosen, $\mathbf{P}^{-1}\mathbf{A}$ equals to an identity matrix $\mathbf{I}$ of the same size as $\mathbf{A}$, and the Krylov subspace method converges in one iteration.

However, selecting such $\mathbf{P}$ shifts the computation load from solving $\mathbf{A}$ to solving $\mathbf{P}$, resulting in no improvement in efficiency. A good preconditioner should balance between effectiveness and low computation cost. Under the background of BDF scheme and Newton method, the matrix of the linear system to be solved is related to the Jacobian matrix $\mathbf{J}$ of the ODE by:

$$\mathbf{A} = \mathbf{I} - \gamma \mathbf{J}, \tag{4.7}$$

where γ is determined by the time step size and the order of BDF. In this case, an efficient approximation of $\mathbf{A}$ can be a good preconditionor.

In this research, Eq. 4.6 is solved by UMFPACK [20], an external sparse linear LU solver. The construction of $\mathbf{P}$ is based on the same semi-analytical evaluation of $\mathbf{J}$ for the direct dense method, but undergoes more aggressive simplifications. The right-most $\partial(\cdot)/\partial T$ column in the Jacobian matrix is a dense column. But it is found to be pronounced only when the temperature of the mixture is high. Based on this observation, the $\partial(\cdot)/\partial T$ column can be conditionally neglected to remove the right-most dense column in the Jacobian matrix and the additional RHS evaluation for numerical differentiation. In this work, the evaluation of the $\partial(\cdot)/\partial T$ column is enabled only when the mixture temperature is higher than a given threshold. After all the non-zero elements in Jacobian matrix have been evaluated, the preconditioning matrix $\mathbf{P}$ is generated by Eq. 4.7. As suggested in [109], another filter is applied to all non-zero elements of $\mathbf{P}$. All elements in $\mathbf{P}$ having magnitude smaller than a threshold are removed to make $\mathbf{P}$ sparser.

It should be noted that all simplifications on $\mathbf{J}$ and $\mathbf{P}$ are based on the fact that $\mathbf{P}$ only needs to be an approximation of $\mathbf{I} - \gamma\mathbf{J}$. As in the direct dense method, reusing the Jacobian-based preconditioner over time is common in BDF-Newton-Krylov solver.

The performance of the direct dense method with semi-analytical Jacobian matrix and the preconditioned Krylov subspace method are tested systematically. The performance of a given method on a given mechanism is assessed by the average CPU time. Each average CPU time is produced from simulations with twelve different sets of initial conditions. The initial conditions are listed in Tab. 4.1. The simulation is advanced with a fixed time step size $\Delta t = 50$ μs towards 1 s. The simulation is terminated at 1.5 times the ignition delay if the mixture ignites within 1 s. The moment of ignition is defined as the moment that the temperature is 400 K above the initial temperature.

Table 4.1: Initial values of temperature, pressure, and equivalence ratio resulting in twelve combinations.

Equivalence Ratio	ϕ_0	0.8, 1, 1.2
Pressure	p_0	2 bar, 10 bar
Temperature	T_0	1000 K, 1200 K

Table 4.2: Details about the selected mechanisms.

Fuel	n_{sp}	n_{rxn}	Reference
n-Heptane	29	52	[73]
Propane	92	621	[97]
n-Heptane/Methyl Decanoate	132	588	[50]
n-Butanol	243	2854	[5]
Butanol isomers	431	2551	[87]
n-Heptane	654	5258	[61]

The simulations in which the mixture does not ignite are excluded from the calculation of average CPU time. The performance test in this work also considers different mechanisms. Both reduced and detailed mechanisms, and mechanisms for different fuels are included in the test. The size of the selected mechanisms ranges from $n_{sp} = 29$ to $n_{sp} = 654$. Table 4.2 lists the details of all selected mechanisms.

The performance of the direct dense method with semi-analytical Jacobian formulation and the preconditioned Krylov subspace method are compared with the performance of the stock time stepper of CANTERA via average CPU time. CANTERA's time stepper uses the direct dense method with numerical Jacobian formulation. The average CPU times for each method to simulate each selected mechanisms are plotted in Fig. 4.1. It can be seen from the results that there is no globally optimal method. For smaller mechanisms, the direct dense method is more efficient with either semi-analytical or numerical Jacobian formulation. For large mechanisms the preconditioned Krylov subspace method is optimal.

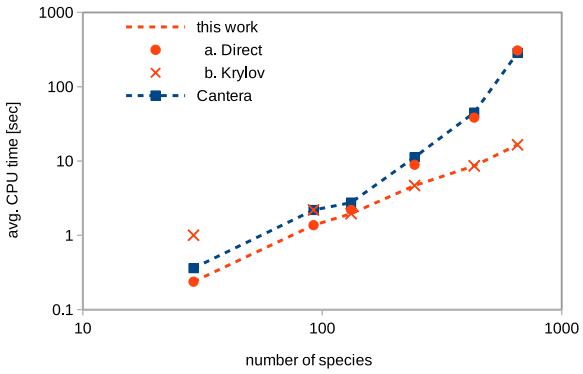

Figure 4.1: Average CPU times for direct dense method with semi-analytical Jacobian formulation, preconditioned Krylov method, and CANTERA to simulate all selected mechanisms [106].

4.2 Simulation of Diesel Engine Operation

The efficient chemical kinetics solver is integrated into KIVA to solve the local chemical kinetics problem for each finite volume cell. In order to validate the computational method, the operation of a conventional AVL 5402 single cylinder diesel test engine is simulated. The key parameters of the AVL 5402 engine are listed in Tab. 4.3. A reduced n-heptane mechanism [51] is used to model the chemical processes of diesel combustion. The mechanism includes 39 species and 98 reactions. It should be noted that the diesel surrogate, n-heptane, is only use to model the chemical processes, while the liquid properties of the fuel still use the values of diesel. The flow inside the simulated engine is swirl-dominated and can be fitted by a function along the radial direction. Thus the simulations performed in this project are closed-chamber simulations with fitted initial swirl flow. All simulations start from the moment of intake valve closing (IVC) and finish at the moment of exhaust valve opening (EVO). Three engine load levels, 10, 15, and 20 mg fuel per cycle are tested with keeping the SOI timing and engine speed at 356° crank angle and 1200 rpm, respectively. For the load level of 15 mg, two additional SOI timings, 352° and 360° crank angle, are tested. The comparisons between the predicted pressure trace and the measured pressure trace are shown in Fig. 4.2 and 4.3. As shown, the CFD program and the customized chemical kinetics solver are capable of predicting the ignition and combustion in CI engine with reasonable accuracy, regardless of the engine operation condition variation.

Table 4.3: Key parameters of the AVL 5402 single cylinder test engine.

bore [mm]	85.0	nozzle diameter [mm]	0.18
stroke [mm]	90.0	fuel delivery type	common rail
compression ratio	17.1	rail pressure [bar]	600
IVC angle [°]	226	intake type	naturally aspirated
injector type	multi-hole	swirl ratio	1.779
number of nozzles	5	EGR type	not mounted
distribution cone angle [°]	142		

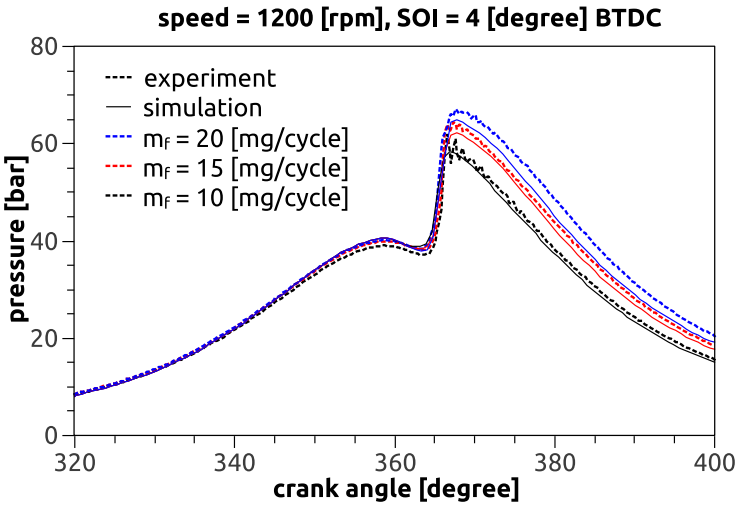

Figure 4.2: Comparison between predicted and measured pressure trace under different engine loads.

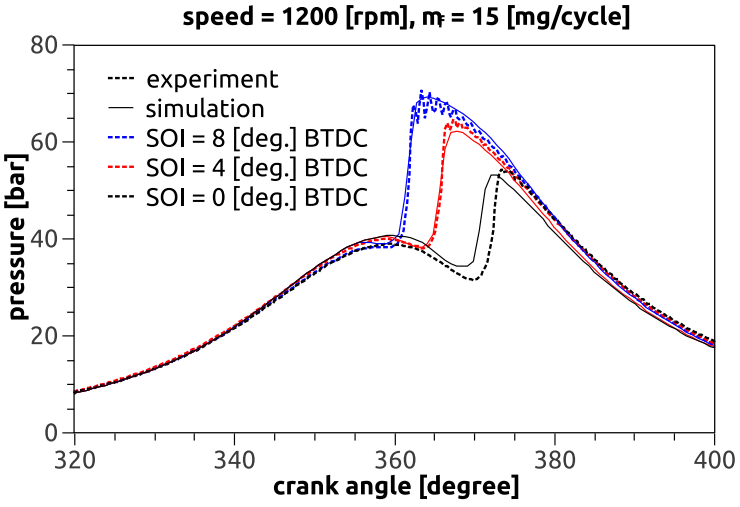

Figure 4.3: Comparison between predicted and measured pressure trace with different SOI timings.

4.3 Single Injection Ignition Phase Curve and Combustion Regimes

Ignition is one of the most important physical and chemical processes in the operation of CI engines. The ignition phasing and robustness of a CI engine have dominant effects on the engine's efficiency, pollutant emissions, noise production, structure lifespan, and controllability. In most conventional CI engines, the ignition phasing largely depends on the SOI timing. Modern engine control unit (ECU) maps the SOI timing within the operation condition envelope, and adaptively adjusts the SOI timing on the fly to target the desired combustion phasing. Apart from the SOI timing, the ignition phasing is also sensitive to multiple parameters, *e.g.* intake gas pressure, temperature, EGR ratio, compression ratio, coolant temperature, fuel quantity, fuel composition, *etc.* Comprehensive understanding of the ignition phasing and the pre-ignition physical state (the mixture preparation outcome) is the key to effective CI engine combustion concept innovation and operation scheme optimization.

Kook *et al.* [47] used a small bore optically-accessible diesel test engine to study the ignition, combustion, and pollutant formation under low temperature combustion (LTC) operation condition. The ignition delay was reported for a wide range of SOI, *i.e.* from $\sim 330^\circ$ to $\sim 370^\circ$ crank angle. It was found that a minimal ignition delay exists within the range of tested SOI. This fact was explained by correlating the ignition delay and the averaged temperature from the SOI to the start of combustion (SOC). Also studied in detail was the effect of EGR on the ignition. The ignition delay time was shown to be roughly proportional to $X_{O_2}^{-1.2}$, where X_{O_2} is the molar fraction of O_2. While the test covered moderately advanced SOI timing, the authors had not tried to further advanced the SOI timing and bridge the LTC operation with moderately advanced SOI timing to the homogeneous charge compression-ignition (HCCI) operation. Kook *et al.* [48] then extended the SOI timing to 160° crank angle. Ignition delay curves were obtained for different compression ratio and different engine speed. The trend of the ignition delay was well explained based on the temperature and pressure during the development of the flame. But the result showed non-monotonic trend of the ignition phasing, which was not addressed. More detailed analysis on spray dynamics and turbulent transport are needed to explain the ignition with deeply advanced

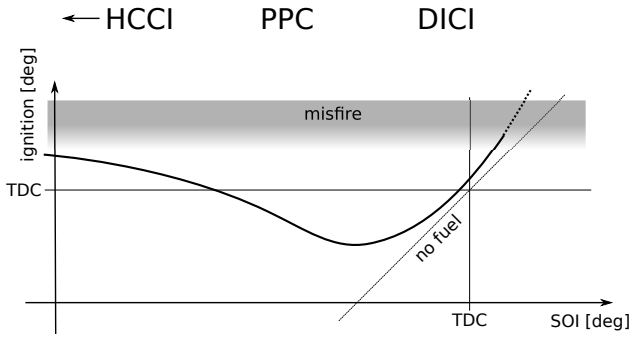

Figure 4.4: A schematic plot of ignition phase curve [108].

SOI timing.

Kiplimo *et al.* [44] studied experimentally the effects of injection pressure, SOI, and EGR ratio on the combustion in a (partially) premixed charge compression ignition (PCCI, considered equivalent to PPC in this study) engine. The ignition delay was measured for SOI timing as early as 330° crank angle. The transition to PCCI combustion regime was identified with the present of the two stage ignition behavior and the cool flame before the high temperature ignition.

Solaka *et al.* [95] conducted similar experiments in a PPC engine with multiple fuel blends developed from primary reference fuels (PRF), toluene, and ethanol. A series of ignition delay curves were experimentally obtained to analyze the effects of research octane number (RON) and motor octane number (MON), as well as the effects of individual fuel components.

In the current study, an ignition phase curve as shown in Fig. 4.4 is proposed. Figure 4.4 considers the ignition phasing as a function of SOI. The ignition curve consists of two segments. Closely following the unit slope on the right is the conventional DICI segment. With advancing the SOI, the ignition transits from the DICI mode to the PPC mode, in which earlier SOI results in retarded ignition due to the over-mixing effect. Excessively advanced SOI leads the ignition curve to either misfire or the HCCI limit on the far left.

The chemical kinetics solver developed in this study is used with a toluene reference fuel (TRF) surrogate mechanism for diesel [111] to study the different ignition regimes from a single diesel injection [108]. Additional computational [103] studies are also performed with a reduced n-heptane mechanism [51] to obtain more comprehensive understanding about the ignition phase curve and the combustion regimes under different engine load.

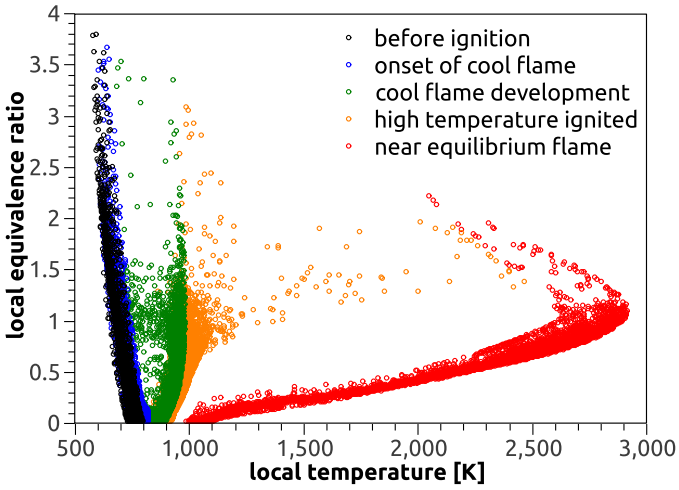

Figure 4.5: An example of $T - \phi$ distribution plot through the combustion process.

4.3.1 Overview of the Ignition Phase Curve

The ignition process in a CI engine simulation is visualized in Fig. 4.5. In the plot, the location of each scatter point shows the instantaneous temperature (horizontal axis) and local equivalence ratio (vertical axis) of a finite volume cell. Before ignition, the scatters form a slope on the left of the plot. The relatively lower temperature in the rich region is due to: a) fuel is injected at a lower temperature than the in-cylinder gas; b) evaporation of fuel is endothermic. The onset of the cool flame is marked by the initial heat release, which is identified by visual inspection of the temperature "bump" on the $T - \phi$ distribution front. With the development of the cool flame, the temperature rises steadily. Once the chemical processes are sufficiently activated due to the radical accumulation as well as the temperature increase, high temperature ignition takes place with drastic temperature jump in the near-stoichiometric region and the rich region. In the following discussion, the high temperature ignition refers to the moment at which at least one finite volume cell has local temperature above 1500 K. Eventually, the $T - \phi$ approaches the chemically equilibrium state.

The proposed ignition phase curve as shown in Fig. 4.4 is verified by CFD computation of an AVL 5402 single cylinder test engine. The geometry and operation parameters of the AVL 5402 engine are listed in the Tab. 4.3. For the baseline ignition phase curve, the load of the engine is fixed at 15 mg per cycle; the speed of the engine is fixed at 1200 rpm. The baseline high temperature

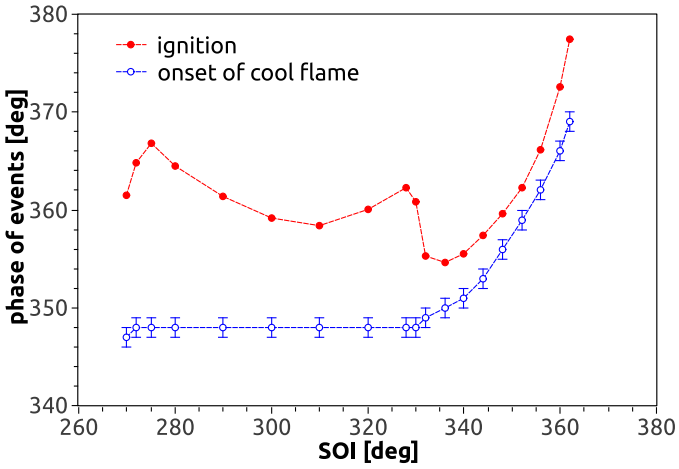

Figure 4.6: The baseline (high temperature) ignition phase curve and the onset of cool flame [108].

ignition phase curve shown in Fig. 4.6 follows the expected ignition phase curve except the non-monotonic behaviors in the PPC segment, which are addressed in the following section. In the PPC regime, the onset of the cool flame timing does not change significantly. With advancing the SOI timing, the over-mixing effect shrinks the volume of the rich and near-stoichiometric region, resulting in retarded high temperature ignition. However, the lean region responsible for the onset of the cool flame has local equivalence ratio close to the overall value, thus not significantly affected by the over-mixing effect, resulting in the stable onset of cool flame timing.

4.3.2 Effects of Combustion Chamber Geometry

Non-monotonic behavior of the ignition phase exists in the vicinity of SOI = 320°. The ignition is delayed by $\sim 5°$ near SOI = 320°, from the otherwise monotonic PPC segment of the ignition phase curve. This is due to the spray impingement upon the upper neck region of the bowl in the piston. In order to verify this conclusion, additional simulations with simplified piston geometry are conducted. The simulation results and comparisons between the stock and simplified piston geometry are shown in Fig. 4.7 and 4.8. The results demonstrate that by simplifying the bowl geometry and reducing spray penetration upon the piston bowl neck, the non-monotonic ignition behavior near SOI = 320° is removed.

Figure 4.6 also shows enhancement of ignition near SOI = 270°. The abnormal advancement of the ignition phasing is caused by the relatively rich mixture near the cylinder wall shown in

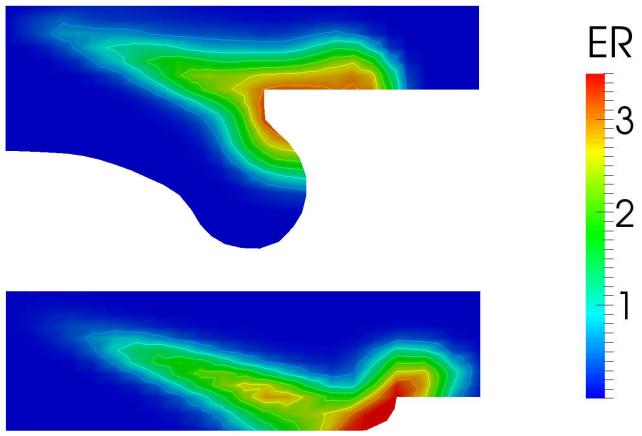

Figure 4.7: The equivalence ratio distribution at 4° after SOI (SOI is at 330°) [108]. The stock and simplified piston geometry are compared with each other.

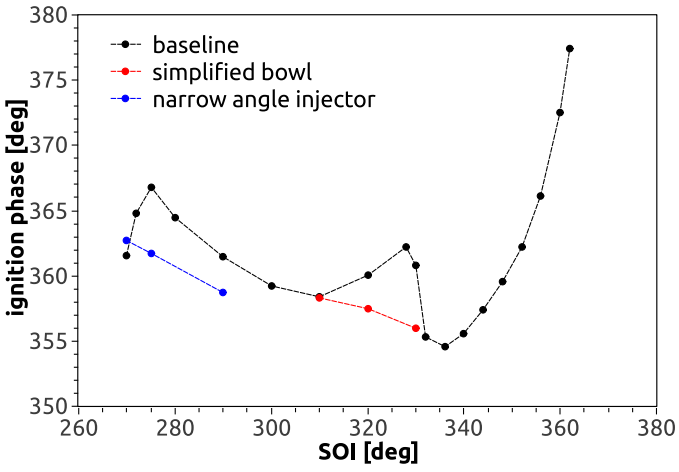

Figure 4.8: The baseline ignition phase curve and deviations via altering the piston and injector geometry [108].

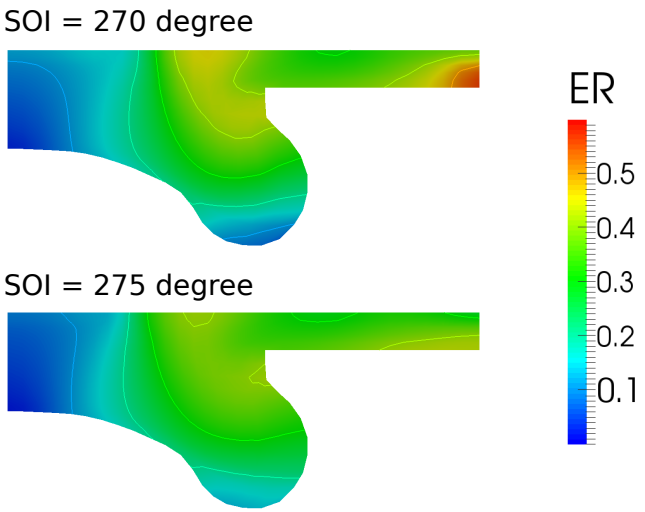

Figure 4.9: The equivalence ratio distribution of two baseline cases at 346° (before the onset of cool flame) [108].

Fig. 4.9. Near the corner between the piston top and the cylinder liner, the viscous effect is strong due to the existence of the solid wall. With the spray aiming at the corner, which is the case when SOI $\approx 270°$, the fuel-air mixing is slowed down due to the ineffective transport. It is demonstrated in Fig. 4.8 that the non-monotonic behavior caused by the near-wall-enrichment can be alleviated by reducing the injection distribution cone angle to 90°. It should also be noted that the problems of poor atomization and wall wetting become in-negligible when advancing the SOI towards the HCCI limit [36]. Injector with narrow cone angle nozzle orientation not only suppresses the abnormal local enrichment near wall, but also reduces the risk of spray impingement upon the cylinder wall.

Another noticeable factor that affects the ignition is the heat transfer loss to the solid wall. The case of SOI = 328° with the baseline settings is used to illustrate the effects of heat transfer loss. As shown in Fig. 4.10, the fuel vapor is split by the upper bowl neck into two regions. Some of the fuel is trapped in the squish region, while the rest is in and above the piston bowl. The mixture in the squish region happens to be richer than the mixture in the bowl, as shown in Fig. 4.10. Due to the strong heat transfer to the cylinder head and the piston top, the mixture in the squish region is constantly cooled, and has about 30 K cooler pre-ignition temperature than the gas inside the bowl with the same equivalence ratio, as shown in Fig. 4.11 and 4.12. The cooling effect results in considerably slower fuel consumption in the squish region than in the piston bowl,

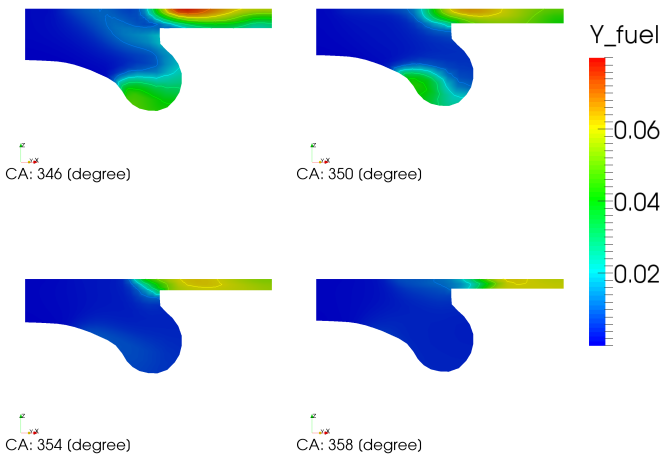

Figure 4.10: Evolution of the fuel mass fraction distribution in the baseline case with SOI = 328° [108].

which is visualized in Fig. 4.10.

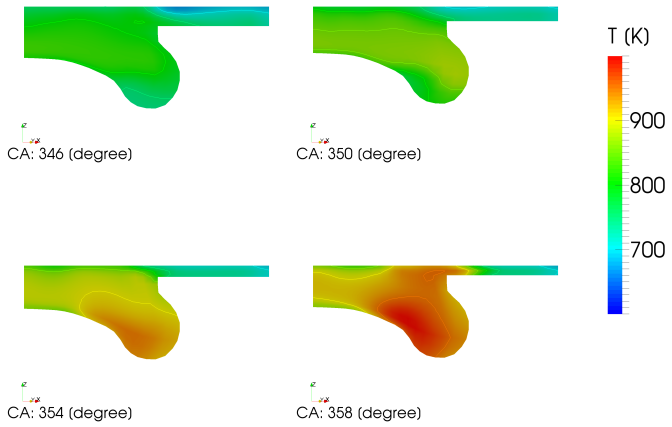

Figure 4.11: Evolution of the temperature distribution in the baseline case with SOI = 328° [108].

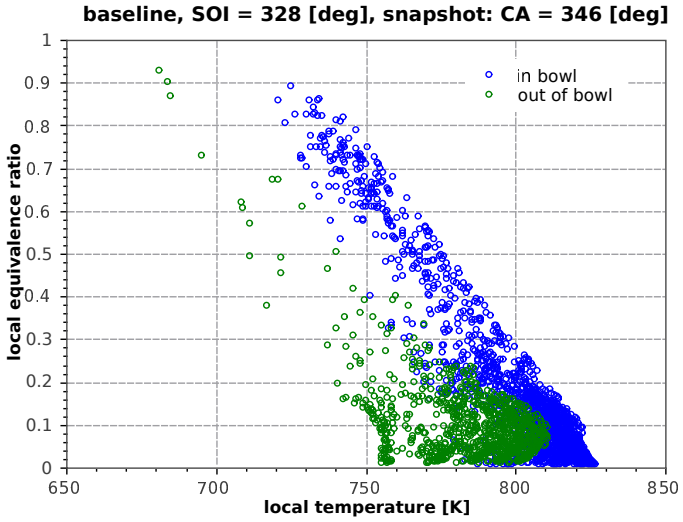

Figure 4.12: In bowl and out of bowl $T - \phi$ snapshot of the baseline case with SOI = 328° AT CA = 346° [108].

4.3.3 Effects of Temperature

The baseline ignition phase curve is constructed with $T_{\mathrm{IVC}} = 340$ K. In order to study the effects of intake temperature on the ignition phase curve, another two ignition phase curves are constructed with higher and lower IVC gas temperatures, *i.e.* $T_{\mathrm{IVC}} = 360$ K and $T_{\mathrm{IVC}} = 320$ K, respectively. The comparison of the three ignition delay curves is shown in Fig. 4.13. Through the range of tested SOI, the ignition phase is sensitive to the IVC temperature in all regimes. For the conventional DICI regime, the higher IVC temperature reduces the ignition delay, while lower IVC temperature elongates the ignition delay. In the late injection operation near SOI = 362°, the flammability limit is slightly affected by the IVC temperature. With higher IVC temperature, the SOI can be slightly more delayed without misfire. For the conventional DICI operation with advanced SOI timing, the IVC temperature affects the transition to PPC operation, in which the ignition phase and SOI are, ideally, negatively correlated. With higher IVC temperature, the DICI-to-PPC transition requires a slightly earlier SOI timing to counterbalance the reduction in the overall ignition delay duration, hence the over-mixing effect.

After the transition to the PPC operation, the sensitivity of ignition phasing to the IVC temperature becomes noticeably stronger than that in the DICI mode. With further advancing the SOI within PPC regime, the sensitivity to temperature keeps growing stronger. The operation does not always asymptotically approach to the HCCI limit with deeply advanced SOI. Higher IVC temperature increases the chance to approach to the HCCI limit. Insufficient IVC temperature, when combined with deeply advanced SOI, may result in misfire.

The high temperature ignition inhibition due to spray impingement is repeated in both $T_{\mathrm{IVC}} = 320$ K and $T_{\mathrm{IVC}} = 360$ K cases. With $T_{\mathrm{IVC}} = 320$ K, the spray impingement results in misfire. This is the reason that in Fig. 4.13, the ignition phase curve of $T_{\mathrm{IVC}} = 320$ K is broken into two parts. Also in the low IVC temperature case, due to the increased sensibility to temperature when advancing SOI, misfire happens before the local enrichment near wall could be effective. In the high IVC temperature case, however, the effect of local enrichment near wall at SOI $\sim 270°$ is repeated. Further advancement of the SOI timing makes it possible to avoid distributing fuel near the corner between the cylinder liner and the piston top. The ignition phase curve returns to the proposed trend beyond the SOI timing of 260° crank angle in the $T_{\mathrm{IVC}} = 360$ K case.

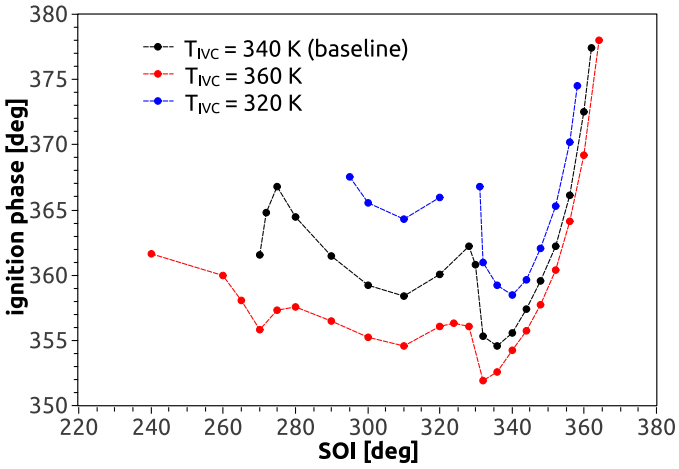

Figure 4.13: The ignition phase curve with different IVC temperatures [108].

4.3.4 Effects of Engine Load and Overall Equivalence Ratio

In order to study the single injection ignition and combustion under different engine load, additional computations are performed [103]. Various fuel quantities from 4 to 16 mg per cycle are tested. The overall equivalence ratio for each tested fuel quantity is listed in Tab. 4.4. For each of the tested fuel quantity, an SOI sweep by the interval of 1° crank angle is performed from 310° to 360° crank angle.

With including low load condition with overall equivalence ratio down to 0.1240, the 1500 K high temperature ignition identifier is no longer applicable. In ultra-lean operation, the combustion temperature might never exceed 1500 K. In order to cover the regular combustion as well as the low temperature combustion of the lean mixture, the CA50 (crank angle that 50% of the heat is released) is used to quantify the combustion phasing. The relation between the CA50 and the SOI timing under different loads is plotted in Fig. 4.14.

Table 4.4: The overall equivalence ratio of each tested fuel quantity.

fuel quantity	overall eq. ratio
4 mg	0.1240
6 mg	0.1860
8 mg	0.2480
10 mg	0.3101
12 mg	0.3721
16 mg	0.4961

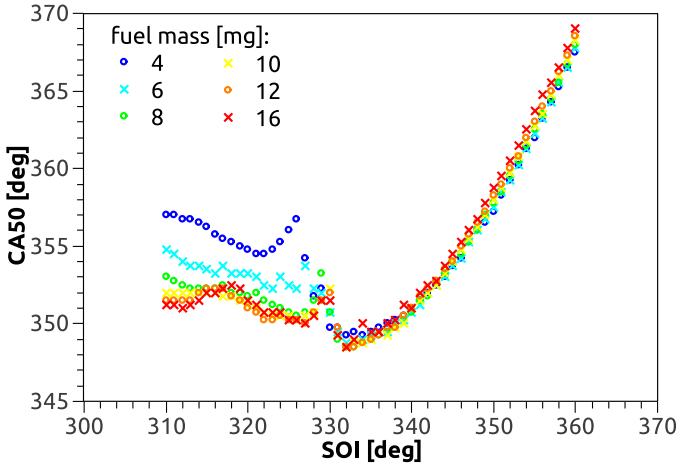

Figure 4.14: CA50 vs SOI timing under different loads.

The additional computation with fine SOI timing interval reveals another non-monotonic PPC SOI-combustion relation exists at loads above 10 mg per cycle within the SOI range from 310° to 320° crank angle. Such non-monotonic behavior is caused by the wall heat loss to the piston top and cylinder head, which is discussed in Sec. 4.3.2. Figure 4.15 compares the spatial distribution of the equivalence ratio (ϕ) at 340° crank angle (pre-ignition) with two different SOI timings, 312° (faster ignition) and 318° (slower ignition). Both cases have the fuel quantity of 16 mg per cycle. As shown, both cases have considerable amount of near-stoichiometric and rich mixture, which could result in fast ignition. With the SOI at 318° crank angle, most of the fuel vapor ends up trapped in the squish region, where the wall heat loss elongates the pre-ignition induction time. With the SOI at 312° crank angle, a noticeable amount of fast-igniting near-stoichiometric and rich mixture is above the piston bowl, where the heat transfer loss is significantly less. At higher loads above 10 mg per cycle and within the SOI range from 310° to 320°, such heat loss effect in the squish region is responsible for the non-monotonic variation of the combustion phasing.

While generally agrees with the proposed concept of the ignition phase curve (illustrated in Fig. 4.4), Fig. 4.14 reveals important systematic trends that are related to the variation of the engine load and the overall equivalence ratio. At lower load, the PPC has a more delayed timing comparing to that at higher load. In the case that the spray impingement onto the re-entrant bowl neck could be avoided and a smooth DICI-PPC transition could be obtained, a steeper CA50-SOI slope, *a.k.a.* stronger SOI control authority, is expected in the lower load PPC operation. With

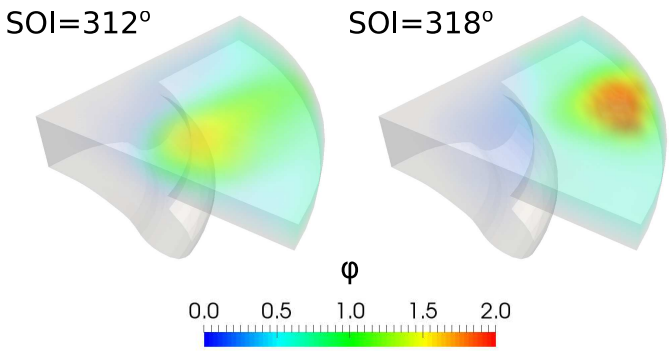

Figure 4.15: The volume rendering of the equivalence ratio at 340° crank angle with two different SOI timings, 312° and 318°. Both cases have the fuel quantity of 16 mg per cycle.

increasing the load and overall equivalence ratio, the PPC phasing advances and the SOI loses control authority over the combustion phasing.

The loss of the SOI control authority is explained by comparing the PPC operation at two loads, 4 and 10 mg fuel per cycle. Figure 4.16 and 4.17 show the pre-ignition (340° crank angle) snapshots of the mixture mass distribution over the ϕ-space. In the lower load case, with advancing the SOI timing from 320° to 310° (a range that is free of the bowl neck spray impingement), the transport process tightens the mixture distribution towards $\phi = 0.1240$, the overall equivalence ratio. At the moment of 340° crank angle, the near-stoichiometric region is completely eliminated with the SOI varying between 310° and 320°. Earlier SOI timing results in lower maximum equivalence ratio (a reduction from 0.7036 to 0.4624, as listed in Fig. 4.16), hence slower chemical kinetics and more delayed combustion. Under a higher load of 10 mg fuel per cycle, in which case the SOI timing loses control authority over the PPC combustion phasing, advancing the SOI timing from 320° to 310° fails to remove the fast-igniting near-stoichiometric region, as illustrated in Fig. 4.17. Due to the appearance of the near-stoichiometric region, the combustion timing does not change significantly with varying the SOI between 310° and 320°. As long as there exists local mixture with the most rapidly igniting equivalence ratio, the SOI's over-mixing-induced control authority over the PPC phasing disappears.

The burning duration of PPC and DICI combustion is also affected by the engine load. In this study, the burning duration is characterized by the duration from CA10 to CA90 (crank angles from 10% to 90% of the heat is released). The CA10, CA50, and CA90 phasing vs SOI timing are plotted in Fig. 4.18 and 4.19 for the load of 4 and 10 mg per cycle, respectively.

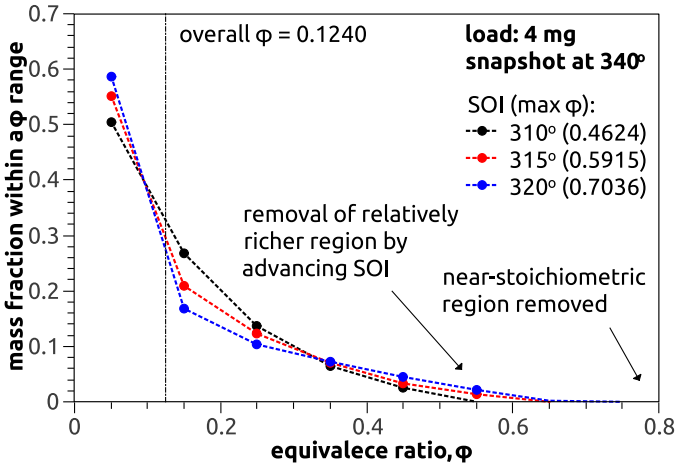

Figure 4.16: Snapshot of the mixture mass fraction distribution in the ϕ-space at 340° crank angle at the load of 4 mg per cycle.

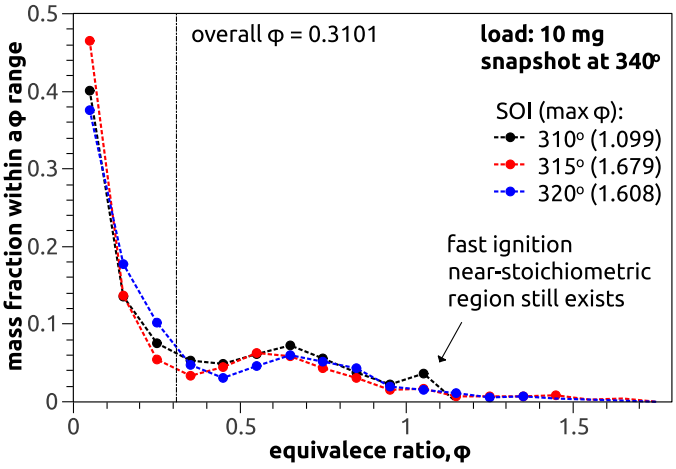

Figure 4.17: Snapshot of the mixture mass fraction distribution in the ϕ-space at 340° crank angle at the load of 10 mg per cycle.

In the PPC regime, the CA50 is close to the middle point between the CA10 and CA90, indicating a near-symmetric heat release process. At the lower load of 4 mg per cycle, the PPC heat release duration is significantly longer comparing to the higher load case of 10 mg per cycle. With 10 mg fuel, the combustion temperature of the PPC regime can rise beyond 2800 K, a temperature at which the kinetics-controlled chemical reactions are fully activated. The fast chemical kinetics results in rapid completion of the heat release. With 4 mg fuel, the overall equivalence ratio is only 0.1240 and the energy density of the mixture is low. After the ignition, the combustion struggles to elevate the maximum local temperature above 1500 K. The fuel conversion is limited by chemical kinetics through the combustion event, resulting in the long heat release duration. It can be concluded that, in the PPC regime, leaner operation results in slower heat release that spans longer duration, and potentially smoother operation.

In the DICI combustion, the CA50 is considerably closer to the CA10 comparing to the CA90. This is due to the signature two-stage heat release characteristic of the DICI combustion. After ignition, the well-premixed fuel-air mixture that is produced during the ignition induction time is consumed in a short period of time due to the high mixture energy density and fast post-ignition chemical kinetics. The fast premixed combustion stage is responsible for the shorter duration from CA10 to CA50. Once the well-premixed mixture is consumed, the DICI combustion enters the second stage of heat release, which is limited by the species transport. With a higher load, the fraction of the second heat release stage is increased, resulting in the longer CA50 to CA90 duration in Fig. 4.19 comparing to that in Fig. 4.18. With advancing the SOI timing within the DICI range, the ignition delay increases and more fuel is consumed in the premixed burning stage, resulting in a shorter CA50 to CA90 duration, as shown in Fig. 4.19.

The combustion efficiency is a measure of the completeness of the conversion from chemical energy to thermal energy. Practical engine operation requires the combustion efficiency to be greater than at least 0.8 for effective use of fuel as well as environmental safety. Fig. 4.20 shows the combustion efficiency as a function of the SOI timing at three different load: 4, 10, and 16 mg fuel per cycle. At low load, the energy density and the combustion temperature of the mixture are low, resulting in incomplete combustion. Worth noted is the PPC combustion at the load of 4 mg fuel per cycle, whose combustion efficiency is only approximately 0.6. Under this load, the DICI

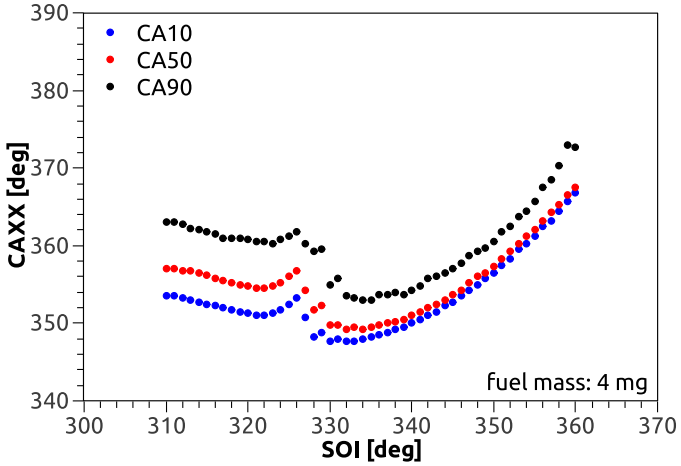

Figure 4.18: CA10, CA50, and CA90 vs SOI timing under the load of 4 mg per cycle.

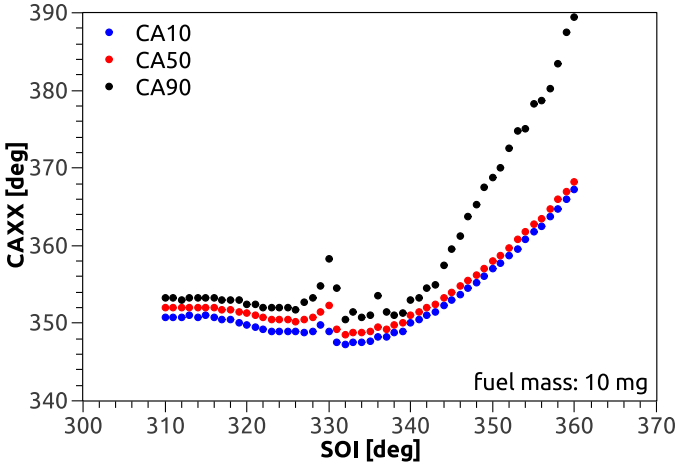

Figure 4.19: CA10, CA50, and CA90 vs SOI timing under the load of 10 mg per cycle.

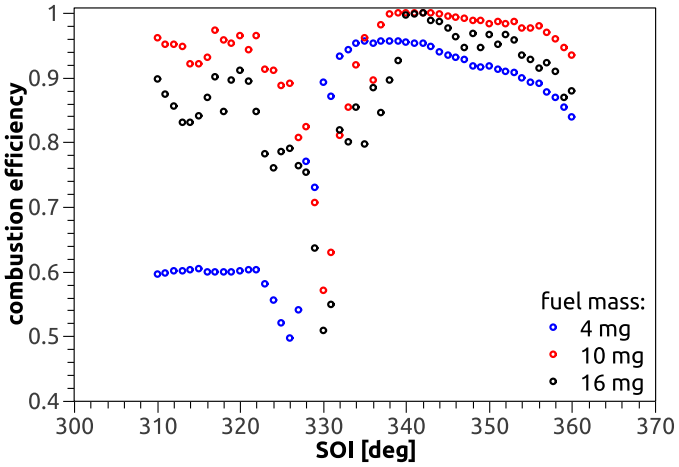

Figure 4.20: The combustion efficiency at load of 4, 10, and 16 mg per cycle.

combustion efficiency is also not ideal due to the fact that a significant amount of the fuel is over-mixed. With increasing the load to 10 mg (overall $\phi = 0.3101$), both PPC and DICI combustion have combustion efficiency greater than 0.9. Further increase the load to the highest tested level of 16 mg, the combustion efficiency drops in both regimes. In the PPC regime, the cylinder pressure and gas density at the moment of injection is low, resulting in non-ideal atomization, long liquid penetration, as well as wall wetting. The wall wetting reduces the amount of fuel that can be converted, hence the combustion efficiency. In the DICI regime, the decreased combustion efficiency is caused by the under-mixing effect. Due to the relatively high fuel quantity, rich region survives throughout the combustion event. Consequently the DICI fuel conversion at high load is also incomplete.

4.4 Gasoline Direct-Injection Compression-Ignition Engine

Among the numerous efforts of developing clean and efficient internal combustion engine technology is the application of gasoline-like fuel in CI engines. By adopting gasoline, a fuel being physically more volatile but chemically less reactive than diesel, the combustion process and outcome are different from those of diesel-fueled CI engine. Extensive studies have been conducted to understand the gasoline direct-injection compression-ignition (GDCI) engine operation and to exploit the advantages of GDCI technology.

Ra *et al.* [79] conducted CFD simulations of a GDCI engine at the fixed speed of 1200 rpm.

Systematic parametric studies were conducted to discover the effects of injection timing, fuel split, EGR ratio, boost pressure, IVC temperature, fuel quantity, swirl ratio, nozzle size, and rail pressure on the engine performance and emissions. The extensive simulation results provided a comprehensive early understanding of the GDCI engine operation.

Kalghatg *et al.* [40] experimentally tested the GDCI operation on a small bore single cylinder CI test engine. Ultra low NO_x and soot emissions were achieved simultaneously with gasoline fuel and sufficient EGR. Comparison with diesel test results eliminated the possibility of achieving simultaneous reduction of NO_x and soot emissions down to the gasoline operation level with diesel fuel. It was also found that the pressure rising rate (PRR) can be reduced with adopting gasoline fuel, reducing the engine operation noise.

Ciatti and Subramanian [16] produced similar results on a gasoline-fueled four-cylinder small bore diesel test engine. Different mixture preparation strategies were tested with both single injection and split injections. The subsequent low temperature PPC was shown effective to enable efficient and clean GDCI operation at multiple operation conditions. Ciatti *et al.* [15] extended their study on the effects of mixture stratification. Complex mixture preparation methods involving up to three gasoline direct injections were tested. CFD simulations and mixture distribution visualizations were also conducted to help explaining the effects of injection strategy observed in the engine experiments at different operation conditions.

Sellnau *et al.* [90] conducted both experimental and numerical studies to discover the GDCI operation strategy under low, medium, and high load. At low load, the ignition robustness was improved by the technique of internal EGR via exhaust port. The warm internal EGR gas was shown to enhance the ignition with minor increase of heat loss. At medium load, a triple injection strategy was found optimal to balance between smooth pressure rise and efficient combustion phasing. With the triple injection strategy, the combustion was brought closer to TDC without increasing the peak pressure and heat loss. At high load, the technique of late intake valve close (LIVC) was applied to reduce the cylinder pressure and temperature and to increase the ignition delay. Based on the accumulated discoveries, Sellnau *et al.* [89] successfully developed a four-cylinder GDCI engine. PPC operation was tested and mapped within the complete operation envelop.

Kodavasal *et al.* [45] conducted global sensitivity analysis (GSA) to examine the dependency of GDCI operation on multiple parameters. The GSA process has a higher level of automation and produces richer data comparing to conventional parametric study. Previously reported dependency of ignition and combustion on various operation parameters was identified by the GSA computation. It was also found that the liquid penetration is strongly affected by the initial turbulence length scale, opening a new direction for future study of mixture preparation.

Dempsey *et al.* [25] studied numerically the effects of fuel stratification on the GDCI operation and emissions. With highly stratified charge, the ignition timing is effectively controlled by the near-TDC injection, simplifying the combustion phasing control at the cost of higher NO_x emission. With near-homogeneous charge, the GDCI operation is similar to the HCCI operation [23], where the NO_x and soot emissions are optimal. But the GDCI operation faces challenges of weak dependency of ignition timing on the injection timing, limited load range, poor combustion efficiency, *etc.* The moderately stratified charge balances between the two extremes and has good overall potential. But the majority of the fuel is in the near-stoichiometric region, which results in excessive PRR.

In this study [105], the GDCI operation is compared with diesel-fueled operation using the ignition phase curves. Parametric studies are conducted to compare the effects of heating intake air, boosting intake air pressure (inter-cooled), applying warm EGR, and increasing compression ratio. The parametric studies are motivated by the interest on improving the GDCI's ignition-SOI sensibility while maintaining the low emissions of GDCI operation. Base on the extensive simulation data, the level of emissions is correlated to the parameters of the mixture, providing explanations of the emission reduction mechanisms as well as guidelines for the mixture preparation strategies.

4.4.1 Simulation Conditions

In this research, a GDCI engine derived from an AVL 5402 single cylinder diesel test engine is numerically studied. The key parameters of the stock AVL 5402 engine are listed in Tab. 4.3. Adjustments are applied to the piston geometry, the compression ratio, and the injector configuration of the stock AVL 5402 engine. A wider and deeper piston bowl geometry (shown in Fig. 4.21) is used following the suggestion by existing GDCI research [90, 89]. According to the result presented

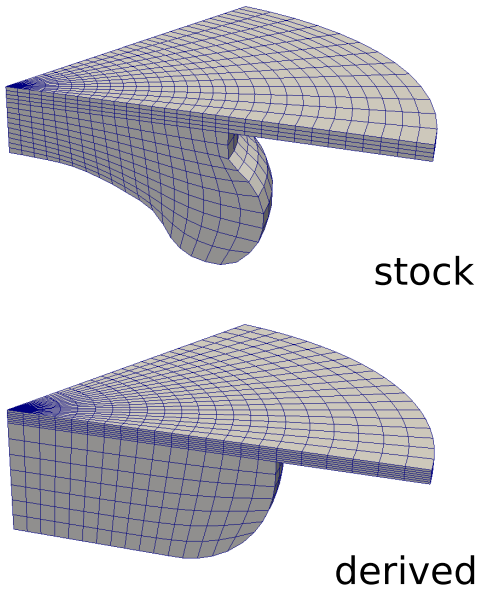

Figure 4.21: Comparison between the geometry of the stock AVL 5402 and the geometry of the derived engine.

in Sec. 4.3.2 about the spray-wall interaction in the stock AVL 5402 engine, the derived engine has a narrower injector distribution cone angle of 110° (stock: 142°) to reduce the abnormal ignition behaviors in the PPC operation. The baseline compression ratio is lowered to 16.0, which is within the range of GDCI configurations found in literature. For gasoline injection, a lower rail pressure of 300 bar is used to estimate the liquid jet velocity. The 300 bar is a typical rail pressure for modern GDI systems.

In this study, the operation speed is fixed at 1200 rpm for all cases. The fuel quantity is fixed at 20 mg per cycle for all cases except the case with smaller fuel quantity. Each engine operation cycle involves only one direct injection to simplify the analysis of the simulation result. Other conditions are listed in Tab. 4.5 for the tested cases. For each of the tested cases in Tab. 4.5, an SOI sweep by the interval of 1° crank angle is performed.

Supplied to the customized efficient chemical kinetics solver is a reduced PRF mechanism [102]. With the PRF mechanism, diesel is surrogated by n-heptane (*a.k.a.* PRF0), while gasoline is surrogated by the mixture containing 15% (by liquid volume) of n-heptane and 85% of iso-octane (*a.k.a.* PRF85). It should be noted that the PRF0 and PRF85 are only used to model the chemical processes, while the liquid properties of fuel still use the values of diesel and gasoline, respectively.

Table 4.5: Tested cases and description.

tested case	description of the case
diesel operation	diesel operation on the derived engine
GDCI baseline	same as diesel operation but use gasoline instead of diesel
GDCI boosted intake	same as baseline but increase the IVC pressure from 1.02 to 1.5 bar
GDCI high compression	same as baseline but increase the compression ratio from 16.0 to 18.0
GDCI high compression lean	same as GDCI high compression but reduce fuel from 20 to 10 mg
GDCI with warm EGR	same as baseline but 15% of the intake gas is from warm EGR
GDCI heated intake	same as baseline but increase the IVC temperature from 355 to 422 K (same IVC temperature as in the warm EGR case)
GDCI heated intake lean	same as GDCI heated intake but reduce fuel from 20 to 10 mg

A 12 step NO_x model [96] is integrated into the PRF mechanism to predict the NO_x emission. The final mechanism includes 77 species and 466 reactions.

4.4.2 Effects of Fuel, Boost, Compression Ratio, and Temperature

The compression ignition and combustion phasing of the baseline GDCI and diesel operation is visualized in the Fig. 4.22. The phasing is characterized by the CA10, CA50, and CA90 timings. By replacing diesel with gasoline, a significantly less reactive fuel, the ignition delay extends, the ignition timing delays, the operational range of SOI shrinks. In the DICI branch of the diesel ignition phase curve, the duration from CA50 to CA90 is clearly elongated with delaying the SOI from $\sim 340^\circ$ to $\sim 355^\circ$ crank angle. The diffusion-controlled combustion is responsible to such elongated heat release. In the baseline GDCI operation, the CA50 and CA90 timings are closely spaced, indicating small fraction of diffusion-controlled combustion, which can be explained by longer ignition delay, faster fuel evaporation and mixing compared to diesel-fueled operation. In diesel-fueled operation, the DICI branch has SOI-ignition control authority over a wide range of SOI phasing, while the DICI branch of the GDCI operation cannot achieve controllable ignition earlier than $\sim 370^\circ$ crank angle due to the transition to PPC branch.

In this study, four strategies are proposed to move the GDCI ignition phase curve towards that of the familiar diesel-fueled operation to improve the controllable SOI range in the DICI branch: boosting the intake (inter-cooled), increasing compression ratio, applying warm EGR, and heating the intake. As shown in Fig. 4.23 to 4.25, each of the four strategies achieves good SOI-ignition control authority through a significantly extended DICI branch, enabling diesel-like ignition

characteristics with gasoline fuel. With the fixed fuel quantity of 20 mg, increasing compression ratio does not change the overall equivalence ratio (ϕ_{avg}) significantly. Boosting the intake increases the air density at IVC, reduces the ϕ_{avg}; while heating the intake has the opposite effect on ϕ_{avg}. Adding EGR increases ϕ_{avg} further by replacing part of the fresh air by combustion products. Due to the increased ϕ_{avg} in the case of heating intake and applying warm EGR, diesel-like elongation of CA50 to CA90 duration is observed in both cases with late SOI timing (as shown in Fig. 4.25), in spite of the fast evaporation and mixing of gasoline fuel. With the same IVC temperature of 422 K, the combustion in the case of warm EGR is delayed by 0.2 to 0.5 ms compared to the case of heated intake, due the the reduced concentration of oxidizer. Nevertheless, applying warm EGR is still an effective approach to achieve diesel-like ignition characteristics in GDCI operation, and has emission advantages compared to heating the intake, as discussed in the later sections. With increasing the compression ratio from 16.0 to 18.0, slightly higher efficiency potential is expected. With the compression ratio of 18.0 and the SOI at 350°, 0.6% more indicated work can be extracted from IVC to EVO compared to the baseline case with similar CA50 timing. The case of boosted intake has a slightly higher indicated work advantage of 1.4% over the baseline case, with the matching CA50. While having similar effectiveness in extending the DICI operation range, applying boost at the medium and low load is believed to be superior than increasing the compression ratio to 18.0 due to its taller operation envelope (higher load within the peak pressure limit), as well as its sightly higher efficiency benefit.

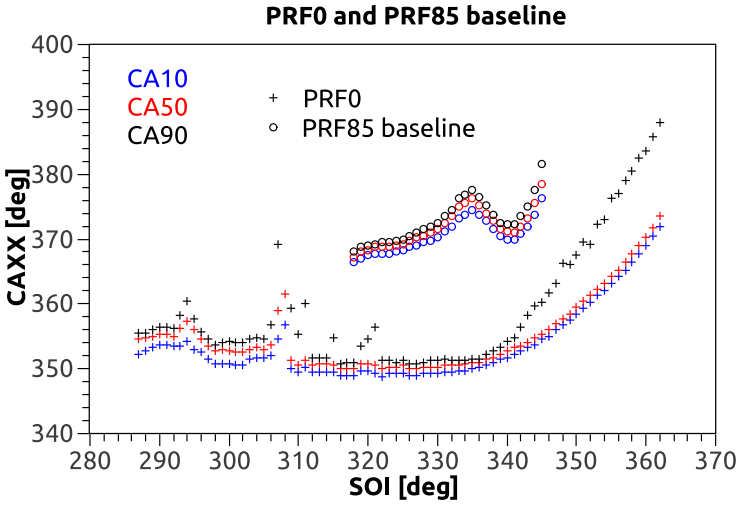

Figure 4.22: CA10, CA50, and CA90 timings of the diesel-fueled operation and the baseline GDCI operation.

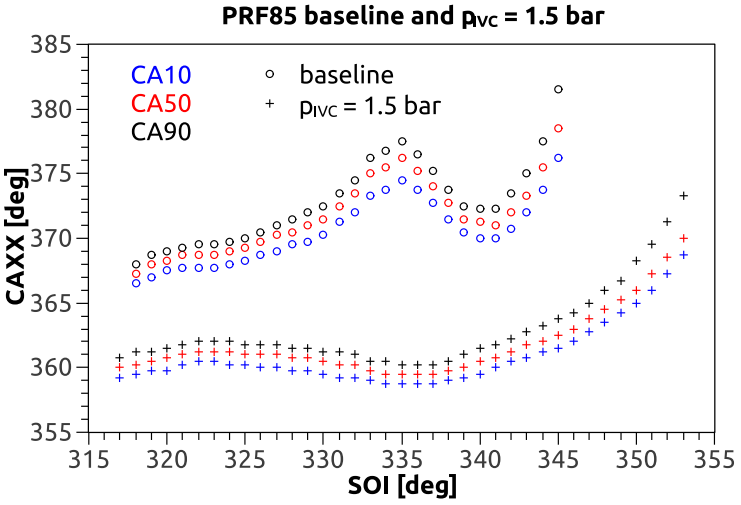

Figure 4.23: CA10, CA50, and CA90 timings of the baseline GDCI operation and the $p_{IVC} = 1.5$bar case.

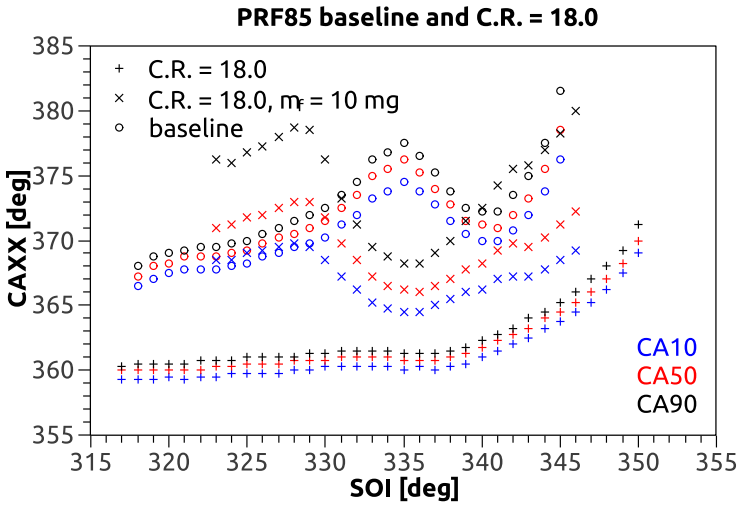

Figure 4.24: CA10, CA50, and CA90 timings of the baseline GDCI operation and the 18.0 compression cases with 20 and 10 mg fuel.

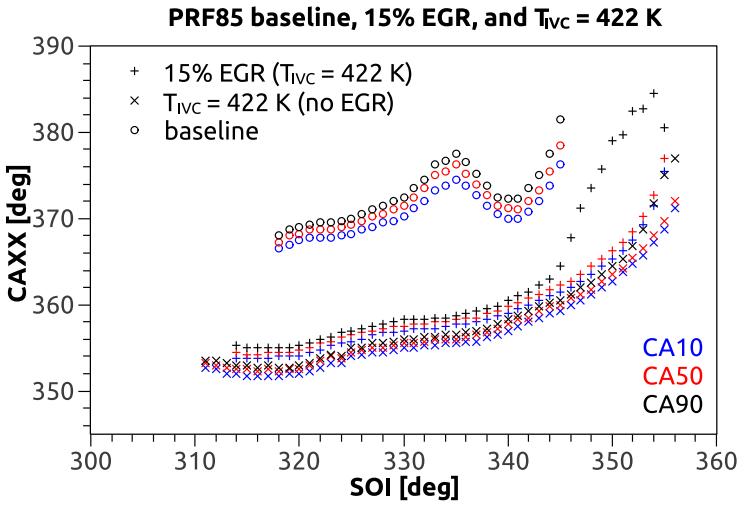

Figure 4.25: CA10, CA50, and CA90 timings of the baseline GDCI operation, the case with 15% warm EGR, and the case with heated intake that has the same T_{IVC} as the 15% EGR case.

4.4.3 Over-mixing and PPC Operation

The SOI-ignition relation in the PPC regime is expected to be monotonic in absence of abnormal spray-piston interactions, as discussed in Sec. 4.3.2. However the proposed monotonic PPC ignition behavior is not achieved in the current GDCI study. As shown in Fig. 4.26, the baseline CA10 phase curve transits from DICI to PPC regime when the SOI is advanced passing 341°. In stead of monotonically approaching to the HCCI limit, the ignition behavior is inverted when SOI is passing 335°. The non-monotonic ignition behavior is due to the fact that the maximum local equivalence ratio in the combustion chamber can not be further reduced by the over-mixing effect of the PPC regime. As shown in Fig. 4.26, advancement of SOI beyond 335° fails to reduce the maximum equivalence ratio in the combustion chamber, causing the non-monotonic ignition behavior.

In the case with increased compression ratio and the case with heated intake, the issue of the abnormal PPC regime becomes more severe: the PPC segment completely loses the SOI control authority over the combustion phasing (as shown in Fig. 4.27 and 4.28). As an effort to recover the SOI's control authority, the two cases are repeated with reduced fuel quantity of 10 mg per cycle. Completely different results are obtained for the two cases. For the case with increased compression ratio and less fuel, the SOI's control authority is partially recovered (as shown in Fig. 4.27); While for the case with heated intake and less fuel, the effort to recover the SOI's control authority fails (as shown in Fig. 4.28). Also noticeable is that by reducing the fuel quantity for the case with higher compression ratio, the ignition phase is delayed for all tested SOIs; While the ignition delay is not significantly changed for the case with heated intake by reducing the fuel quantity. Such result is caused by the different ϕ-sensitivity of ignition for the two cases. With increased compression ratio, the pre-ignition temperature and pressure are $\sim$ 900 K and $\sim$ 40 bar. With heated intake, the pre-ignition temperature and pressure are $\sim$ 1000 K and $\sim$ 35 bar. The ignition delay's sensitivity to the change of ϕ is different for the two conditions. 0-D chemical kinetics simulations are conducted to illustrate the different ϕ-sensitivity at the two representative conditions. As shown in Fig. 4.29, the ϕ-sensitivity at 900 K and 40 bar is significantly stronger than that at 1000 K and 35 bar. In engine operation, the fact that the richer mixture has lower pre-ignition temperature further diminishes the limited ϕ-sensitivity for the case with heated intake, resulting in CA10 timing that is not sensitive to the change of overall equivalence ratio. With

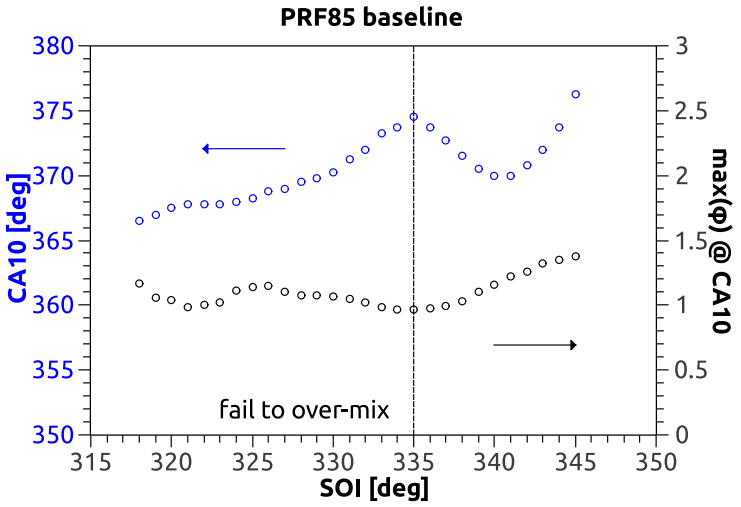

Figure 4.26: CA10 timing and the maximum local equivalence ratio at CA10 of the baseline GDCI operation.

compression ratio of 18.0, the resulting pre-ignition state happens to have strong ϕ-sensitivity, enabling the delayed ignition phasing and partially recovered SOI's control authority by reducing the fuel quantity.

The result in the current GDCI study suggests that the existence of the signature inverse SOI-ignition relation of the PPC regime depends on the effectiveness of over-mixing in reducing the maximum ϕ in the combustion chamber over a range that ignition has sufficient ϕ-sensitivity.

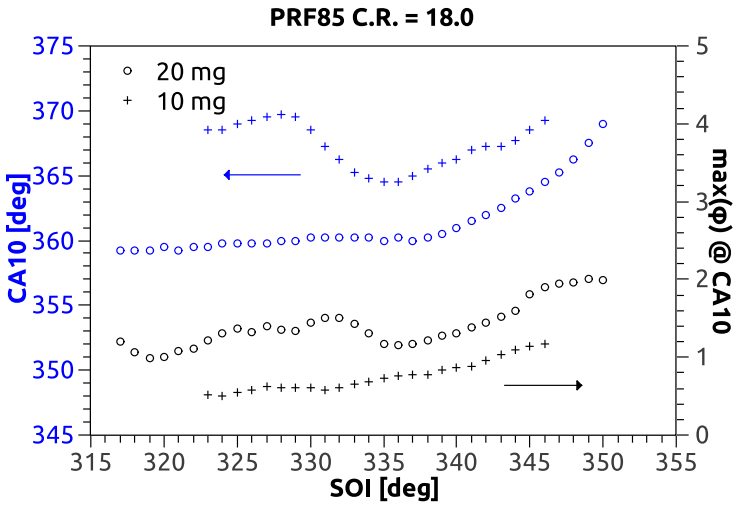

Figure 4.27: CA10 timing and the maximum local equivalence ratio at CA10 of the high compression ratio GDCI operation with 20 and 10 mg fuel.

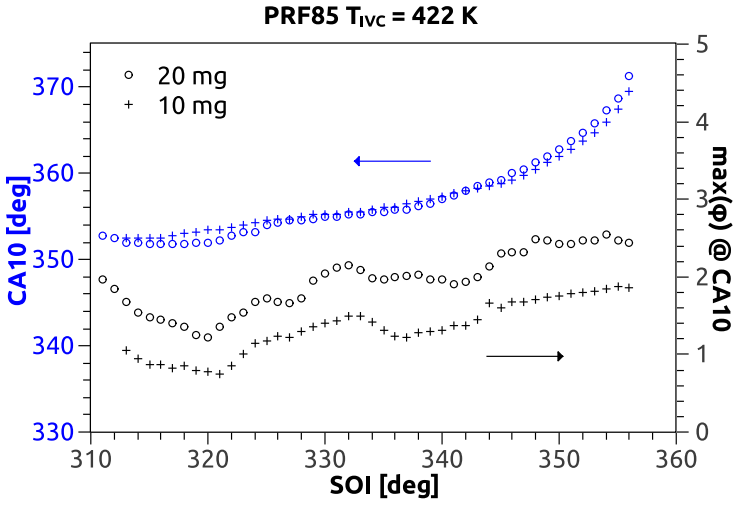

Figure 4.28: CA10 timing and the maximum local equivalence ratio at CA10 of the high IVC temperature GDCI operation with 20 and 10 mg fuel.

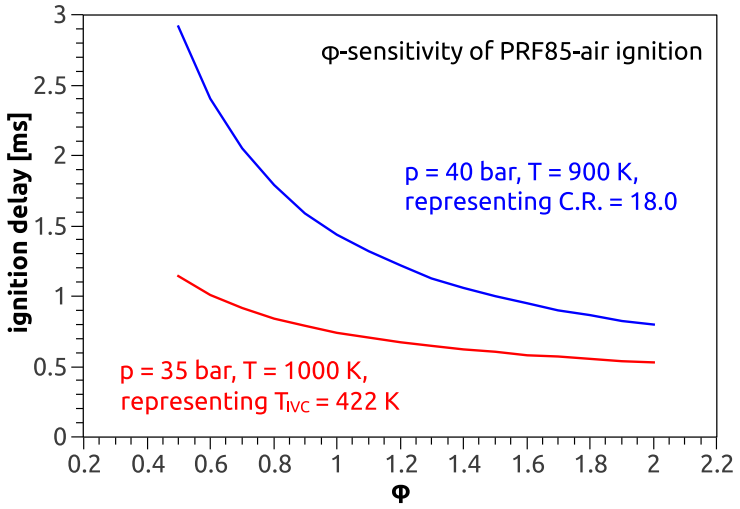

Figure 4.29: ϕ-sensitivity of the PRF85-air mixture ignition under two representative initial conditions.

4.4.4 Emission Dependency: ϕ, T, Dilution, and Beyond

In order to compare the emissions in different cases, a representative SOI is selected for each case. The SOI is selected such that the CA50 is as close to 370° crank angle as possible. The CA50 target of 370° is selected because it is achievable by DICI combustion in all tested cases. The selected SOI as well as the pressure traces for different cases are shown in Fig. 4.30. The engine-out emissions for each case with selected SOI are listed in Tab. 4.6.

As oppose to the expectation, the NO emission does not increase with the IVC pressure, the compression ratio, or the IVC temperature, suggesting an effect (or combined effects) that is stronger than the average temperature and pressure. In order to understand such effect(s), distributions of NO, CO, and volume in the ϕ-space are visualized in Fig. 4.31 to 4.35. All distributions are

Table 4.6: Engine-out emissions for each case.

tested case	NO [g/kwh]	CO [g/kwh]
GDCI baseline	16.3	1.25
GDCI boosted intake	8.72	1.63
GDCI high compression	9.71	1.44
GDCI high compression lean	1.66	49.7
GDCI with warm EGR	4.02	4.10
GDCI heated intake	11.9	0.581
GDCI heated intake lean	11.9	2.66

snapshots at 400° crank angle. The 400° is selected because: a) the combustion is finished; b) the NO_x and CO related reactions are near frozen; c) it is not too late that the dependency of emissions on ϕ is smeared by diffusion.

It can be seen from the NO distributions that the location that generates the most NO has ϕ close to 0.8, where the worst combination of high combustion temperature and sufficient oxygen supply is found. The baseline case happens to have most of the mixture in the vicinity of $\phi = 0.8$, resulting in the worst engine-out NO emission. By applying boost with the same amount of fuel, the ϕ distribution is shifted to the leaner side. Thus the local combustion temperature is reduced and NO formation is reduced.

Comparing the case with heated intake and the case with warm EGR, both cases have the same IVC temperature and similar mixture distribution. But the case with warm EGR significantly reduces the NO formation, demonstrating the effectiveness of reactant dilution in NO reduction.

Another apparent difference between the baseline case and other cases is the tighter correlation between NO and ϕ in the baseline case. In the cases other than the baseline case, a large number of scatters are found under the NO-ϕ "hump", rather than on the "hump". The lack of such NO-ϕ dispersion contributes to the significantly higher NO emission of the baseline case. The NO-ϕ dispersion indicates an unfamiliar mechanism that can strongly affect the NO formation, beyond the NO's well-known dependency on the overall T, ϕ distribution, and dilution. In order to explain the mechanism of the NO-ϕ dispersion, the evolution of the $\phi = 0.8$ iso-surface in the high compression ratio case with selected SOI is visualized in Fig. 4.36. In Fig. 4.36, the $\phi = 0.8$ iso-surface is colored by NO mass fraction and temperature. It is found that even with the same $\phi = 0.8$, the mixture at different location is consumed at different phase of the overall combustion process. Thus the relatively faster local heat release process can be at different stage within the relatively slower global pressure rising process. The $\phi = 0.8$ location that is burned earlier has higher post-combustion temperature comparing to the $\phi = 0.8$ location that is burned near the end of the overall combustion process. As shown in 4.36, the post-combustion temperature can be different by ~ 500 K within the $\phi = 0.8$ iso-surface due to the different sequence of local heat release and local compression, resulting in the NO-ϕ dispersion. Upon the discovery of the NO-ϕ dispersion due to combustion phasing, effort has been made to exploit such mechanism to reduce

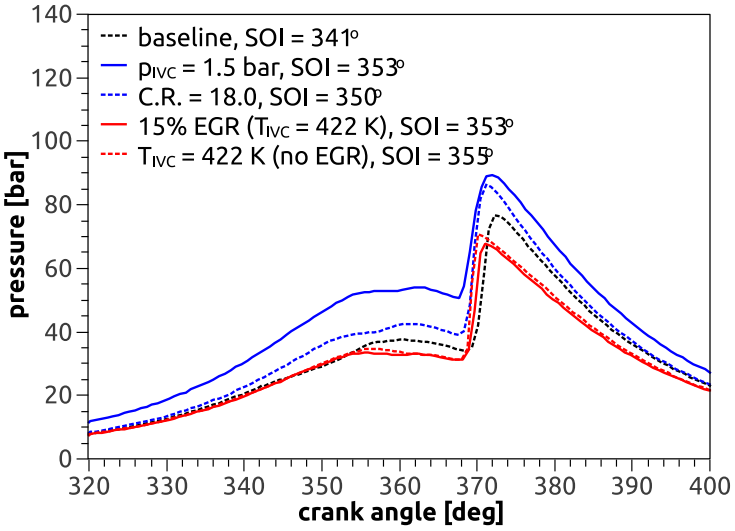

Figure 4.30: Selected SOIs targeting CA50 = 370°, and the pressure traces for different cases.

the NO_x emission [29].

As for the CO emission, two well-known mechanisms are observed in the CO-ϕ scatter plots: a) the over-rich CO due to insufficient oxygen supply; b) the over-lean CO due to low combustion temperature. Worth mentioning is the case with high compression ratio and reduced fuel quantity, which has the lowest overall ϕ among all tested cases. Comically high engine-out CO emission is predicted for this case. Such result indicates the seriousness of the potential over-lean CO in lean burn engine operation.

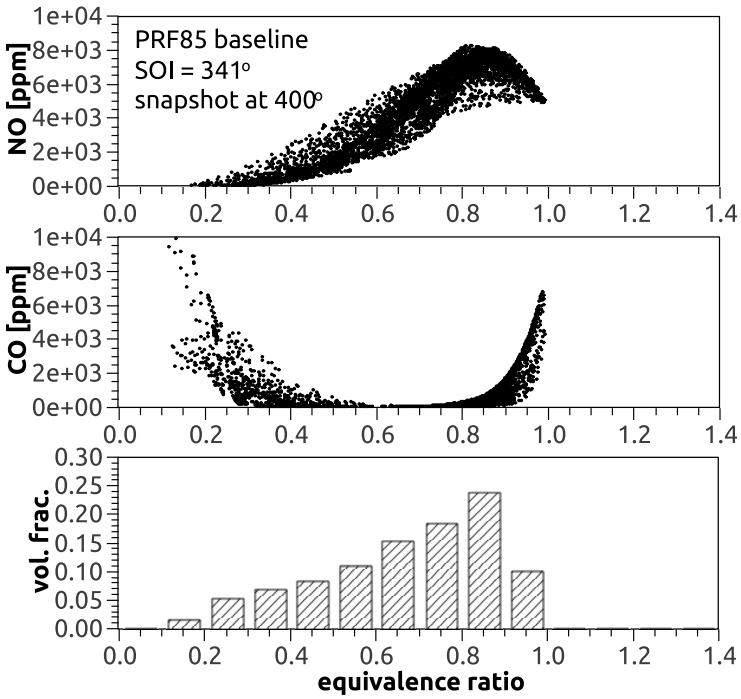

Figure 4.31: Snapshot of the baseline NO_x, CO emissions, and mixture distribution after combustion.

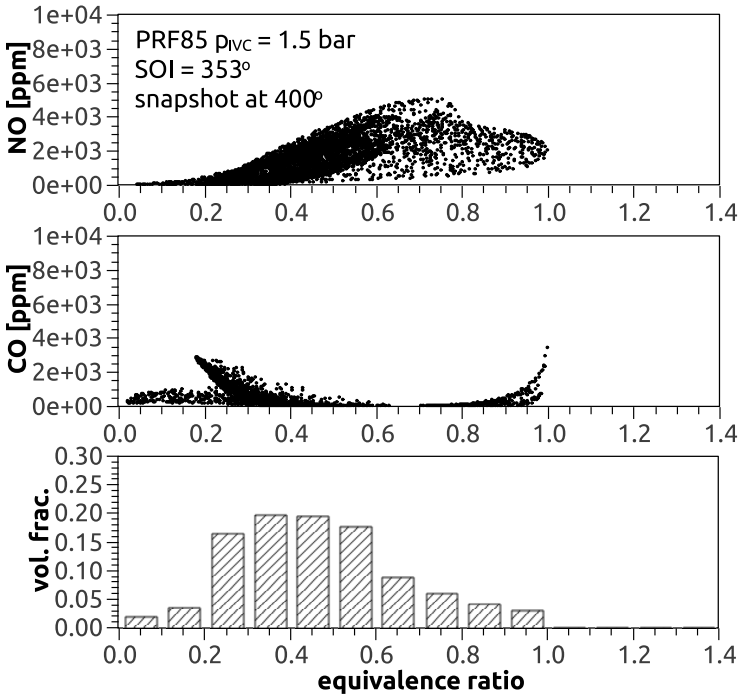

Figure 4.32: Snapshot of the boosted case NO_x, CO emissions, and mixture distribution after combustion.

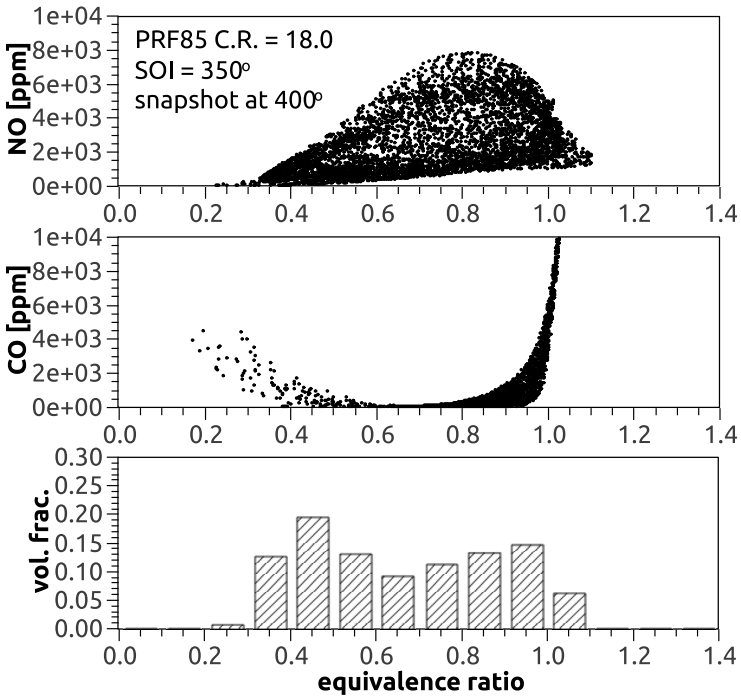

Figure 4.33: Snapshot of the high C.R. case NO_x, CO emissions, and mixture distribution after combustion.

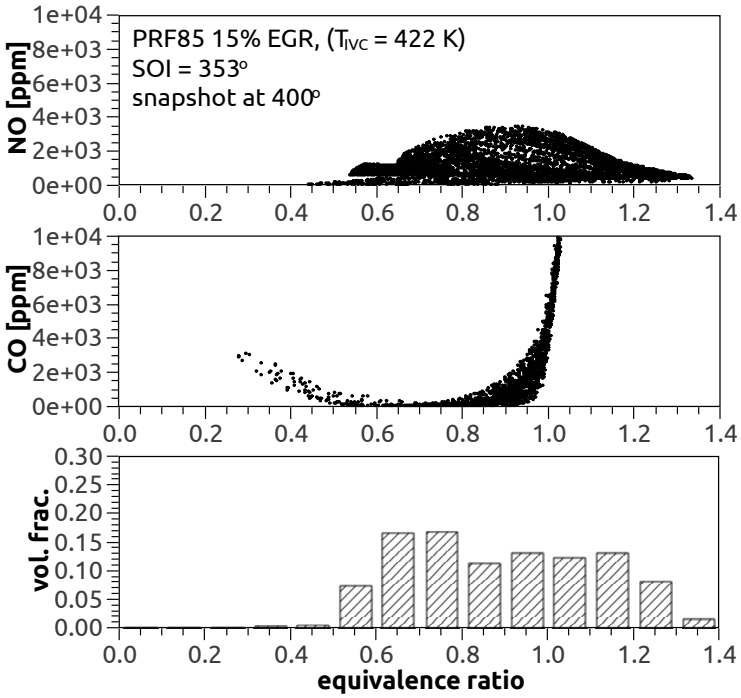

Figure 4.34: Snapshot of the warm EGR case NO_x, CO emissions, and mixture distribution after combustion.

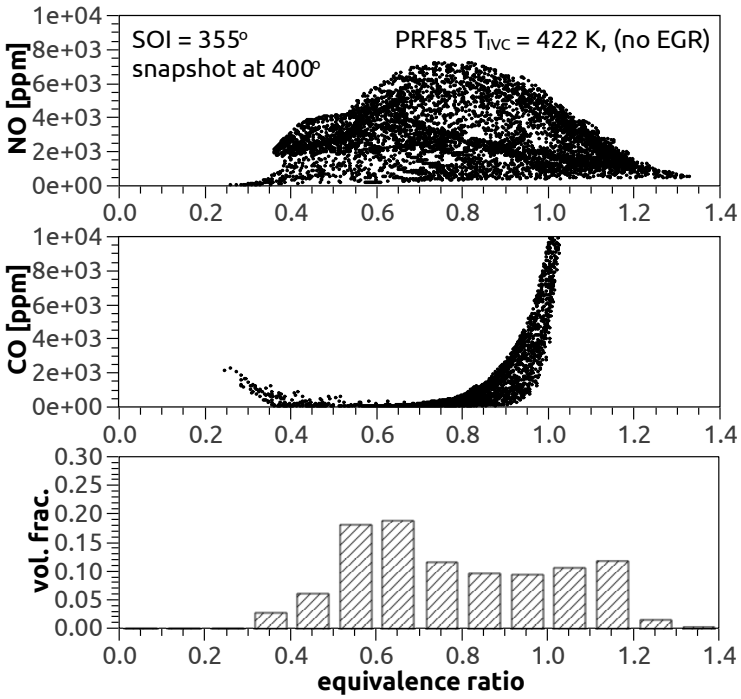

Figure 4.35: Snapshot of the heated case NO_x, CO emissions, and mixture distribution after combustion.

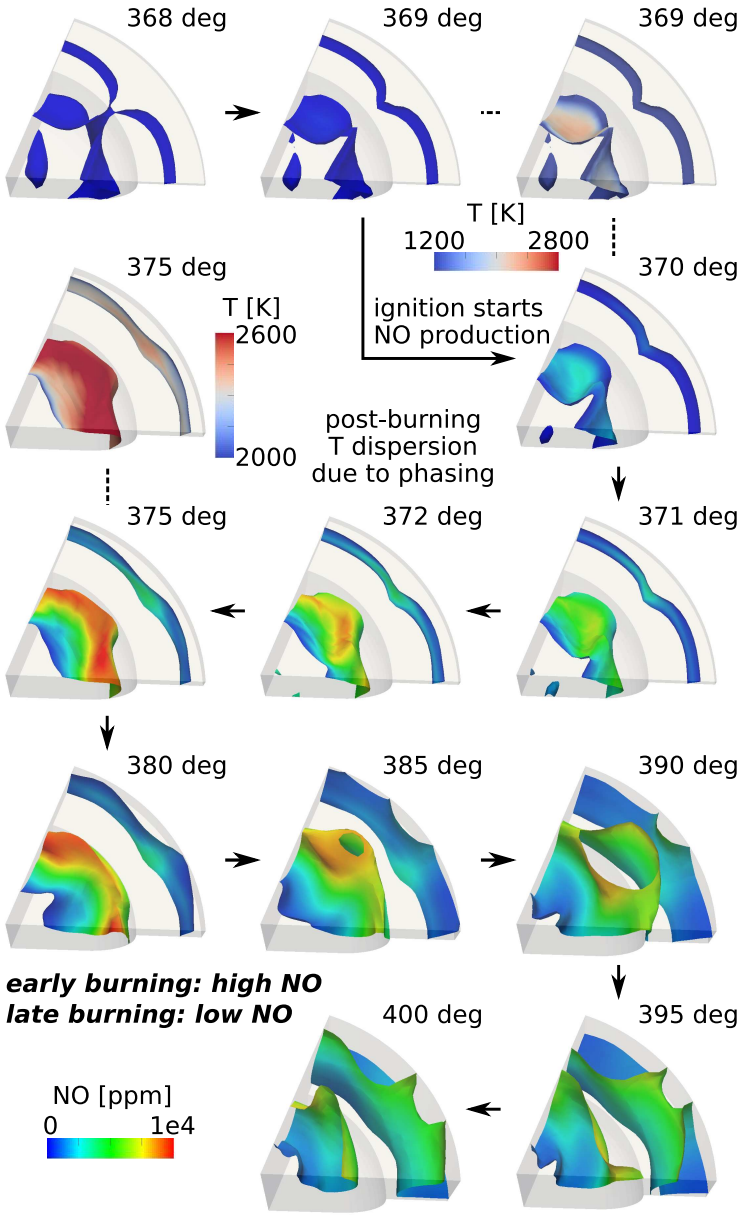

Figure 4.36: the evolution of the $\phi = 0.8$ iso-surface in the high compression ratio case with selected SOI.

4.5 Diesel - Natural Gas Dual Fuel Engine

In the present, two major technology routes exist to achieve efficient and clean internal combustion engine operation with natural gas (NG), namely, SI stoichiometric combustion and dual fuel lean combustion.

SI NG engine operates in the similar way as conventional gasoline engine does. The NG is inducted into the intake system and mixed with air before entering the combustion chamber. The spark discharge triggers the deflagration through the premixed mixture, which consumes the fuel and releases heat. The equivalence ratio of the mixture is controlled in the vicinity of stoichiometry for efficient TWC conversion of the HC, CO, and NO_x emissions. Due to the possible knock of the mixture, the compression ratio of SI NG engine is lower than the typical compression ratio of diesel engine, limiting its efficiency potential. Common approaches to elevate the knock limit include multiple spark plugs [63], pre-chamber design [3], and enhanced turbulent flow [70]. Despite of the efforts, the compression ratio of the NG SI engine still cannot be increased to the diesel level.

In diesel-NG dual fuel engine, the mixture of NG and air is ignited by diesel fuel, which is directly injected into the combustion chamber. Depending on whether the diesel is over-mixed at the ignition kernel, the dual fuel ignition is categorized into DPI and RCCI. In the current dual fuel engine concepts, the overall equivalence ratio is lean. Diesel-NG dual fuel engine has compression ratio similar to that of diesel engine, which results in high efficiency [67]. Due to the excessive oxygen in the exhaust, TWC would be ineffective in converting NO_x. And the engine requires selective catalytic reduction (SCR) or lean NO_x trap (LNT) to achieve the emission regulations such as EPA Tier-4 and Euro-VI. Efforts have been made to reduce the engine-out NO_x emission by using high EGR ratio [19]. RCCI combustion is an effective enabler for high EGR ratio beyond the flame propagation limit, but its high load adaptivity and overall effectiveness is still limited [101].

In this study, a novel concept of high compression ratio stoichiometric diesel-NG dual fuel engine is proposed and computationally demonstrated. In such concept, NG and air are mixed before entering the combustion chamber. A small amount of diesel fuel is injected directly into the combustion chamber. Either DPI or RCCI combustion is triggered by the diesel fuel. Due to the distributed ignition sources and spray-induced turbulence, the combustion is faster than that

in SI engine, effectively elevating the knock limit. Due to the absence of the knock limit from the operation envelope, the compression ratio can be as high as that in diesel engine, increasing the engine's efficiency potential.

4.5.1 Validation of the Simulation Work-Flow

Coupled with the efficient chemical kinetics solver is an in-house-developed reduced mechanism for diesel-NG dual fuel combustion [51]. The mechanism uses n-heptane as the surrogate for diesel fuel. The methane, ethane, and propane reactions are included to simulate the combustion of NG. Also included in the reduced mechanism is the 12 step NO_x model [96]. The final mechanism includes 62 species and 308 reactions. Despite of the premixed flame propagation in dual fuel engine, the CFD simulation depends on the chemical kinetics model rather than a flame propagation model to simulate the chemical reactions. Such configuration is based on the fact that the chemical kinetics dominants the combustion in dual fuel CI engine, while the burning duration is expected to be short due to the spray-induced turbulence and distributed ignition kernels. Due to the lack of the flame propagation model and insufficient grid resolution to resolve the premixed flame structure, error is expected in the predicted burning duration. The simulations performed in this project are closed-chamber simulations. All simulations start from IVC and finish at EVO.

Experimental results were previously obtained from an AVL 5402 single cylinder diesel test engine that has been modified to operate with diesel-NG dual fuel combustion [67, 68]. In this study, the experimental results are used to validate the simulation work-flow for the dual fuel combustion in the AVL 5402 test engine. The key parameters of the AVL 5402 test engine are summarized in Tab. 4.3. In the previous experiments, methane gas with purity greater than 99% was used to represent the NG fuel. The methane gas is inducted into the intake in a controlled flow rate which is determined by the target NG substitution rate. The NG substitution rate is the percentage of the fuel energy contributed by NG. In the validation of the CFD simulation, the engine speed is fixed at 1200 rpm. The total fuel energy is equivalent to 20 mg diesel per operation cycle. Two NG substitution rates, 40%, and 70%, are tested to validated the CFD simulation. For both NG substitution rates, a single diesel injection signaling at 4° BTDC is applied. In order to test the effect of SOI timing, a third operation condition is tested by moving the SOI signal from 4°

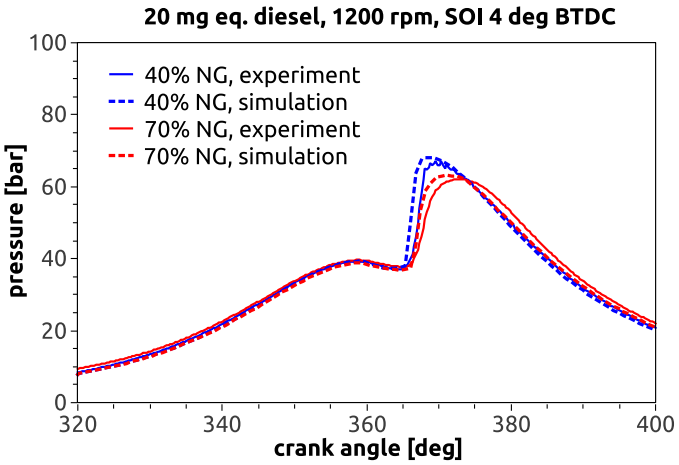

Figure 4.37: The comparison between calculated and measured cylinder pressure with different NG substitution ratios.

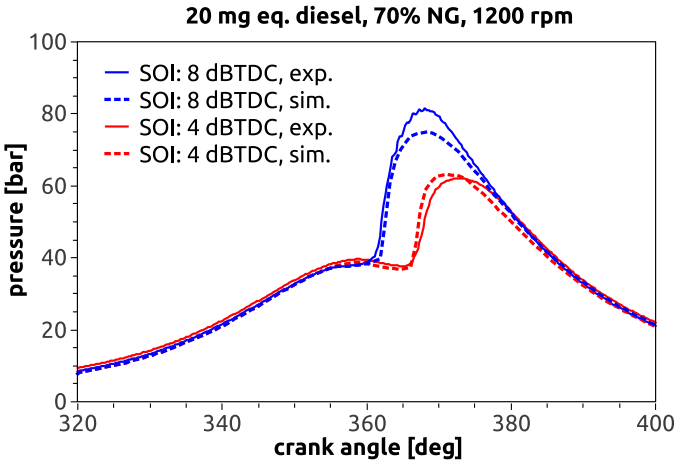

Figure 4.38: The comparison between calculated and measured cylinder pressure with different SOI timings.

to 8° BTDC, for the NG substitution rate of 70%. As shown in Fig. 4.37 and 4.38, the simulation results match reasonably well with the experimental measurements for the tested NG substitution ratios and SOI timings.

4.5.2 Stoichiometric Dual Fuel Mixture Preparation

In the numerical test of the AVL 5402 engine's stoichiometric dual fuel operation, various engine speeds and loads are covered. The tested speeds are 800, 1200, 1600, and 2000 rpm, while the tested fuel quantities are equivalent to 15, 20, 25, and 30 mg diesel fuel per cycle. All the 16

combinations of speed and load are simulated. For each of the 16 operation conditions, the overall equivalence ratio is fixed at 0.995. With the engine being naturally aspirated, the primary load variation method is tuning the EGR ratio. The EGR ratio is limited below 0.35 to guarantee reasonably robust flame propagation. For the tested load of 15 mg equivalent diesel, the EGR ratio is saturated at 0.35, and intake throttling is applied to maintain the overall equivalence ratio of 0.995. In the current research, only a single diesel DI is considered. The DI fuel quantity is fixed at 3 mg for all the operation conditions. The value of 3 mg is chosen such that: a) the spatial variation of the overall equivalence ratio is small at the moment of ignition; b) the ignition is robust; c) the injection system of the AVL 5402 engine can meter the fuel with acceptable accuracy. In the simulation, the NG is considered as the mixture consisting 70% (by volume) methane and 30% propane. With the high propane fraction, slightly higher knock tendency is expected comparing to typical commercial NG. The EGR is represented by nitrogen at the same temperature as the fresh air, allowing for convenient comparison with future experiment.

For each of the 16 operation conditions, an SOI sweep is conducted with the interval of 1° crank angle. The CA10, CA50, and CA90 of the SOI sweep for all operation conditions are plotted in Fig. 4.39. Below are some key observations and explanations of Fig. 4.39:

- The ignition delay is not changed significantly with varying the load, due to the fixed DI fuel quantity.
- The burning duration (in second) is not changed significantly by varying the speed, as oppose to SI engine, due to the fact that the turbulence is dominated by the DI spray.
- The burning duration is longer at lower load, due to higher EGR rate and lower flame temperature.

In order to compare the different operation conditions, a representative SOI is selected for each operation condition. The representative SOI is selected such that: a) for the speed of 800 and 1200 rpm, the CA50 is close to 365°; b) for the speed of 1600 and 2000 rpm, the overall combustion phase is as advanced as possible. The selected SOIs are visualized in Fig. 4.40, and are used in the analysis of performance and emissions.

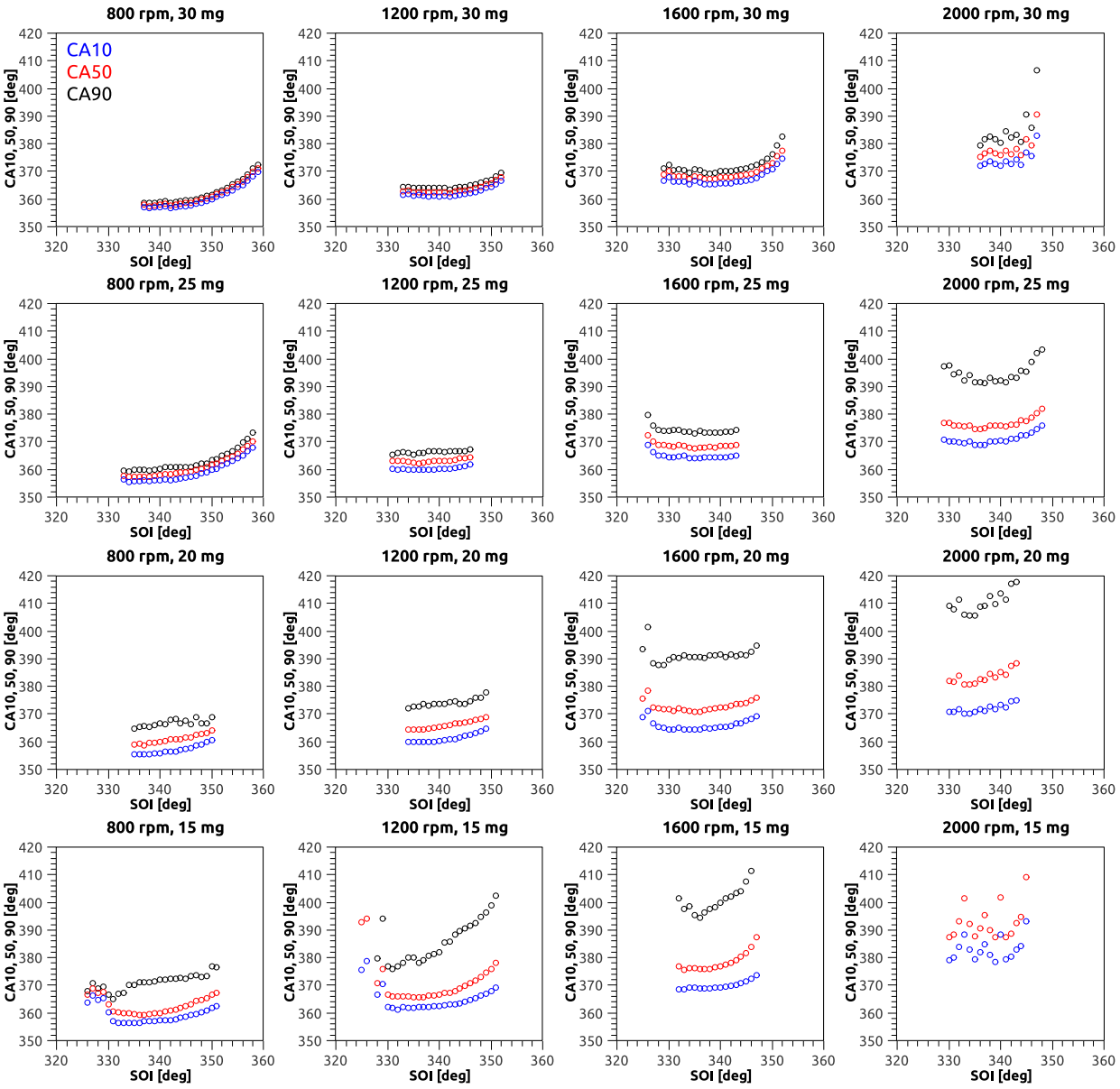

Figure 4.39: The CA10, CA50, and CA90 as functions of SOI at different operation conditions.

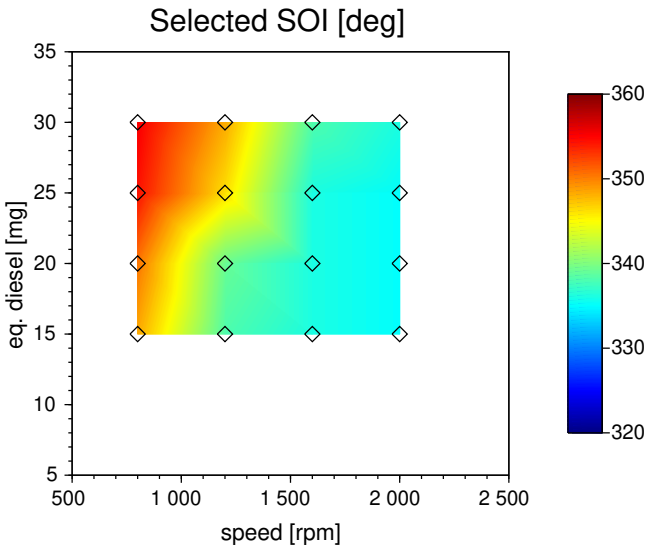

Figure 4.40: The selected SOI timing at different operation conditions.

4.5.3 Stoichiometric Dual Fuel Operation and Limitations

The simulated stoichiometric diesel-NG dual fuel operation at 1200 rpm and with fuel energy equivalent to 25 mg diesel is visualized in Fig. 4.41 to 4.45 (observing from below the piston top surface). Before the injection of diesel fuel, the NG-air mixture is homogeneous and has an equivalence ratio lower than 1. After the injection of diesel fuel, the liquid droplet rapidly evaporates, absorbing heat from the ambient gas. The diesel vapor mixes with air and quickly reduces the maximum local equivalence ratio below 2 at the moment of ignition. The high temperature ignition kernel coincides with the fuel-rich region, where most of the diesel vapor is found. Due to the insufficient oxygen in the fuel-rich region, CO are formed in such location. The ignition also activates the NO formation in the fuel-lean region, where excessive oxygen is available. As the premixed flame quickly propagating from the ignition kernel, the region of NO formation expands with the flame front. The equivalence ratio is continuously homogenized and CO is gradually consumed. Once the ignition happens and through the whole combustion process, the CO concentration closely follows the fuel-rich region. And the region of high NO concentration surrounds but not penetrates the fuel-rich region.

The indicated work from IVC to EVO and the indicated specific fuel consumption (ISFC) at different operation conditions are plotted in Fig. 4.46 and 4.47. It can be seen that fuel economy is

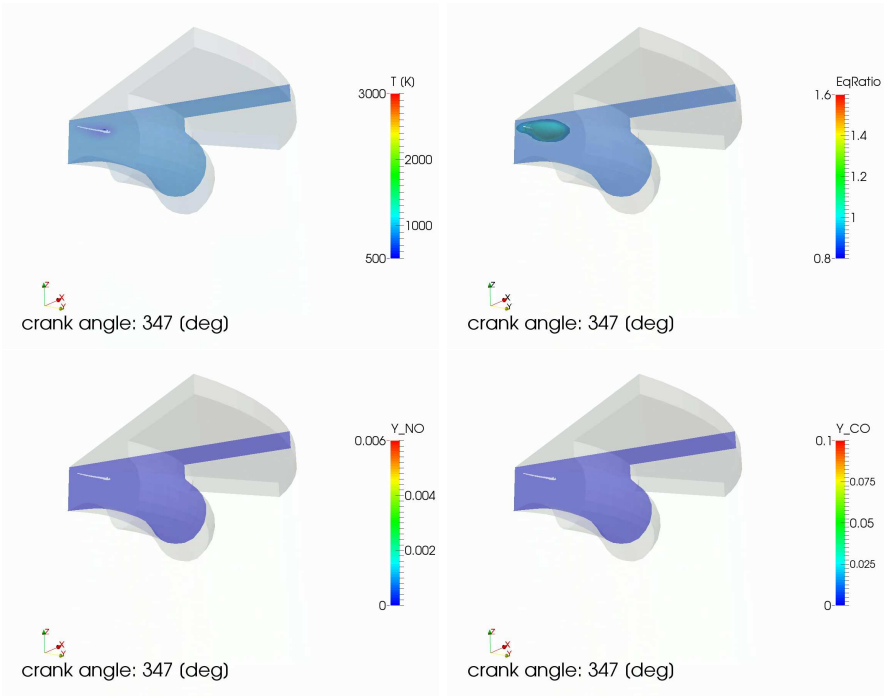

Figure 4.41: The snapshot of temperature, equivalent ratio, NO mass fraction, and CO mass fraction at crank angle of 347°. The operation condition is 1200 rpm and with 25 mg equivalent diesel.

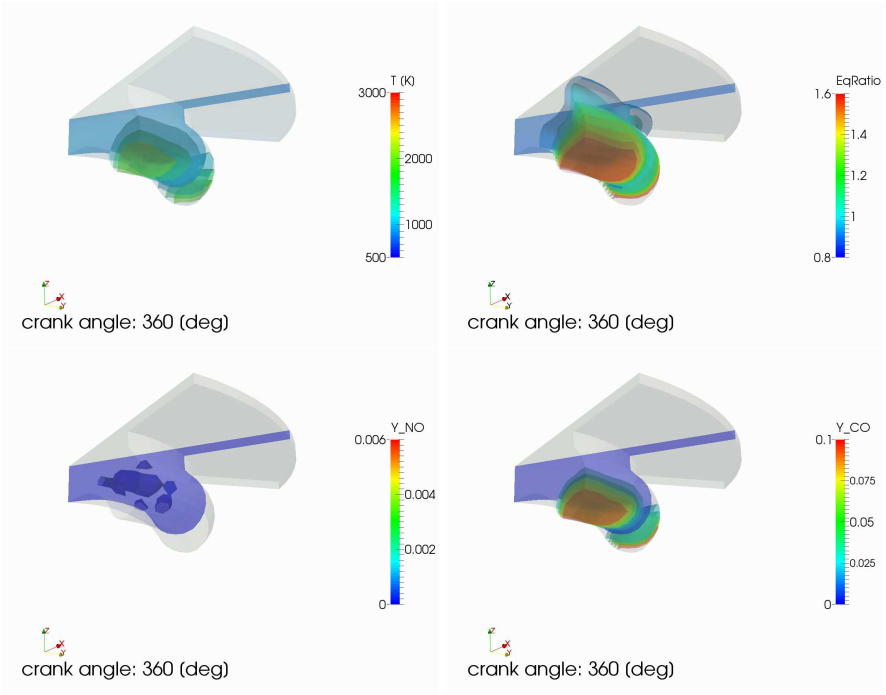

Figure 4.42: The snapshot of temperature, equivalent ratio, NO mass fraction, and CO mass fraction at crank angle of 360°. The operation condition is 1200 rpm and with 25 mg equivalent diesel.

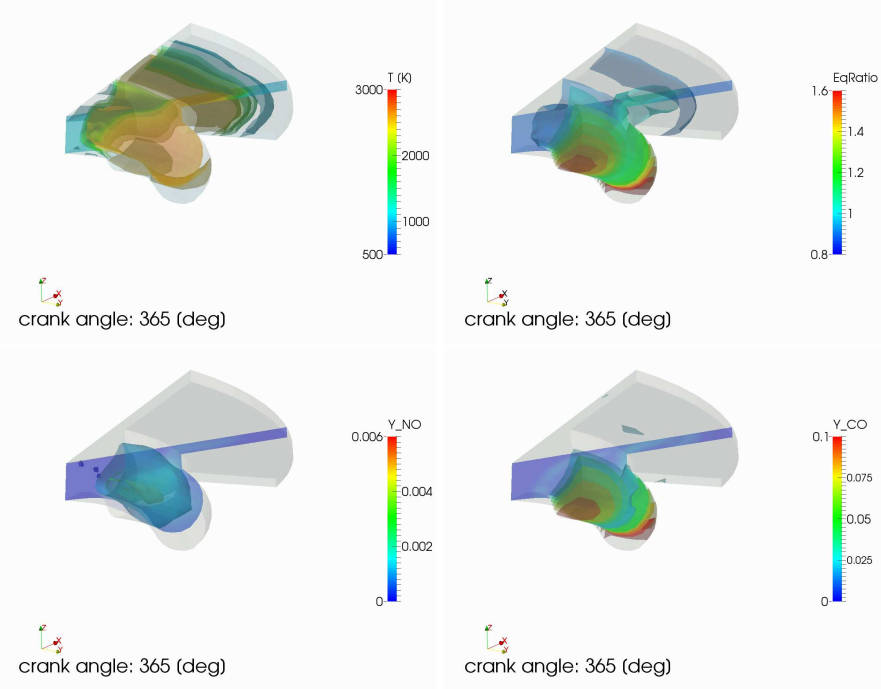

Figure 4.43: The snapshot of temperature, equivalent ratio, NO mass fraction, and CO mass fraction at crank angle of 365°. The operation condition is 1200 rpm and with 25 mg equivalent diesel.

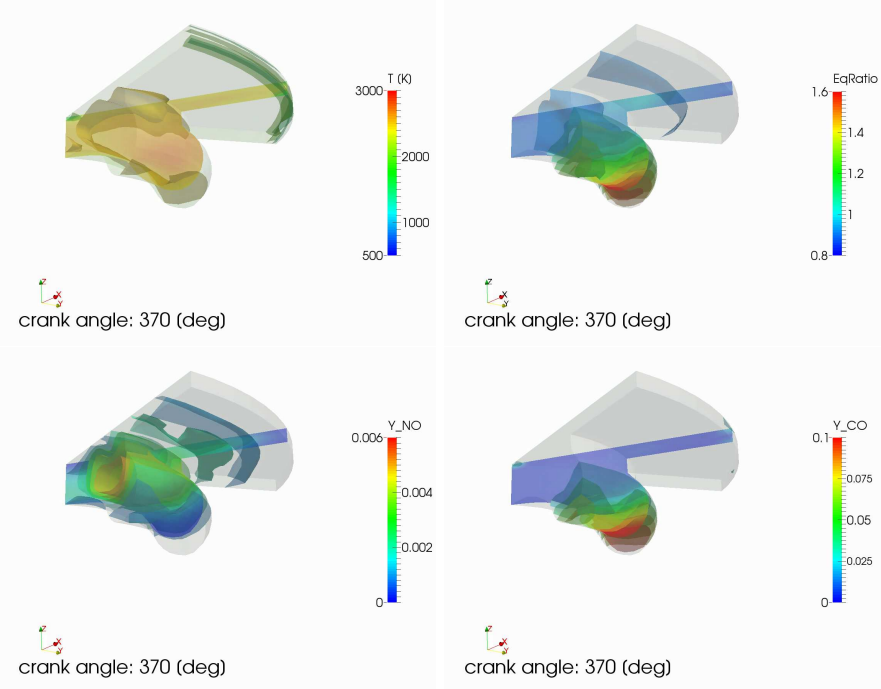

Figure 4.44: The snapshot of temperature, equivalent ratio, NO mass fraction, and CO mass fraction at crank angle of 370°. The operation condition is 1200 rpm and with 25 mg equivalent diesel.

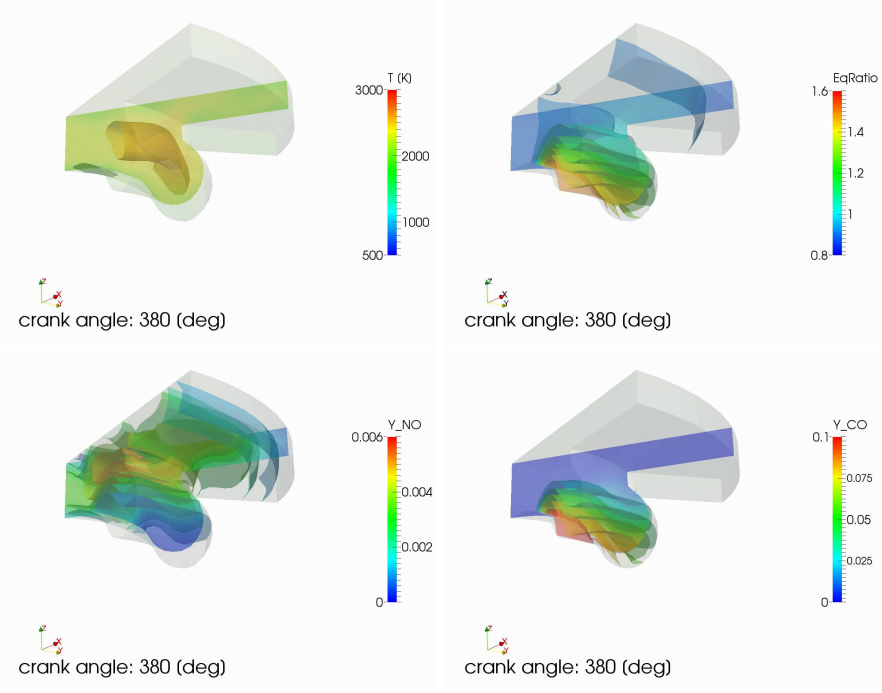

Figure 4.45: The snapshot of temperature, equivalent ratio, NO mass fraction, and CO mass fraction at crank angle of 380°. The operation condition is 1200 rpm and with 25 mg equivalent diesel.

optimal at medium and high load, due to the high flame temperature and fast flame propagation. The fuel economy is worst at high speed and low load as the flame is not robust and the available time for flame to propagate is limited. Slow heat release and incomplete combustion results in inefficient work production. Thank to the high compression ratio, the overall fuel efficiency is competitive comparing to diesel engine.

The engine-out NO_x emission at medium and high load is comparable to that of typcial SI engine. At lower load, the engine-out NO_x emission is significantly reduced due to the high EGR rate. It is possible to reduce the engine-out NO_x down to 0.4 g/kwh only at low load, where the fuel economy is not ideal. The stoichiometric combustion enables the use of TWC. Plotted in Fig. 4.49 is the required NO_x conversion efficiency of the after-treatment system such that the tailpipe NO_x emission is lowered to 0.4 g/kwh. It can be seen that the NO_x conversion requirement is safely within the capability of modern TWC system for the majority of the tested operation range.

The CO emission is due to the locally rich region generated by the diesel injection. With keeping the constant amount of DI diesel at 3 mg, the percentage of energy from diesel is higher at lower

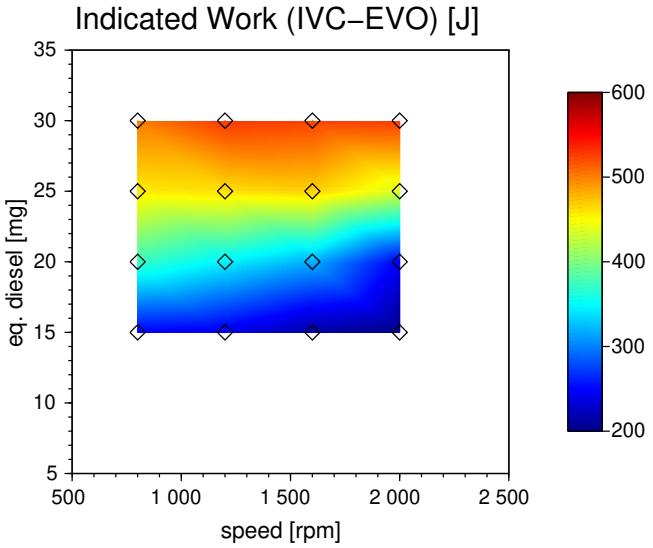

Figure 4.46: The indicated work from IVC to EVO at different operation conditions.

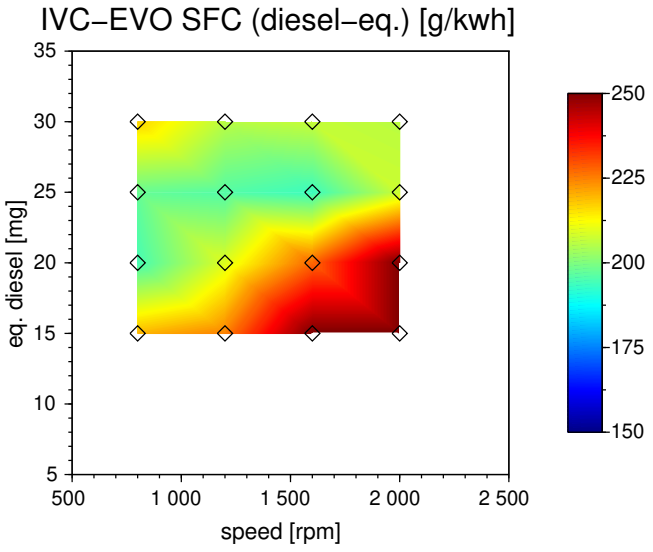

Figure 4.47: The indicated specific fuel consumption at different operation conditions.

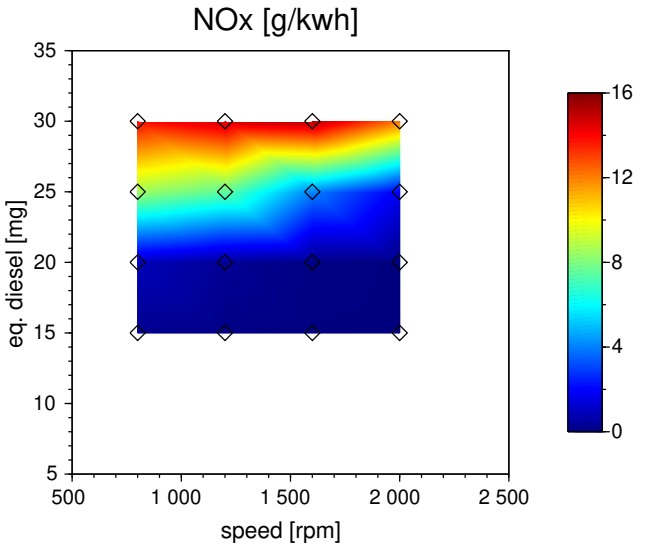

Figure 4.48: The engine-out NO_x emission at different operation conditions.

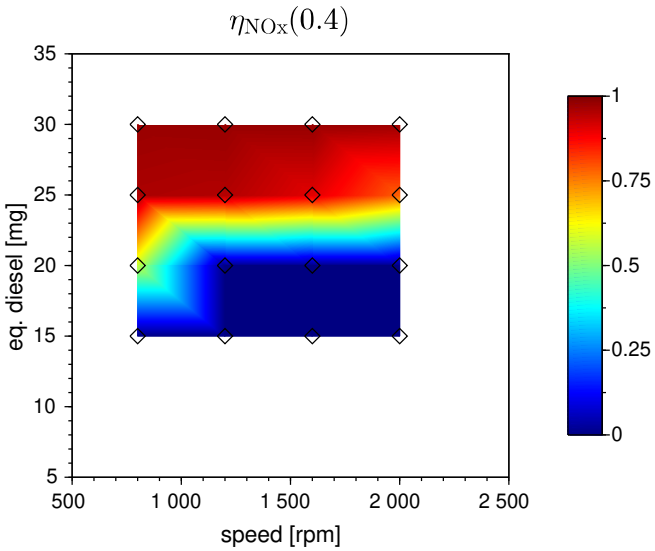

Figure 4.49: The required TWC's NO_x conversion efficiency such that the tailpipe NO_x emission is 0.4 g/kwh.

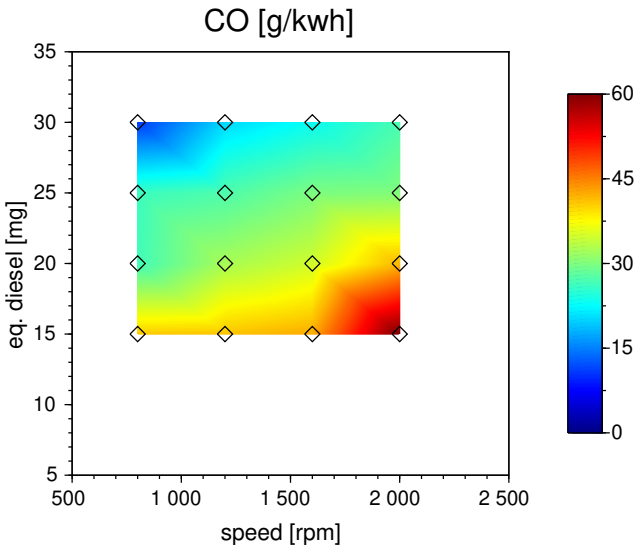

Figure 4.50: The engine-out CO emission at different operation conditions.

load. At low load, the difference between overall equivalence ratio and the equivalence ratio of the NG-air mixture is large, while at high load, the equivalence ratio of NG-air mixture is already close to 1. The higher amount of under-mixed fuel is responsible to the higher CO emission at low load, which is shown in Fig. 4.50.

Figure 4.51 shows the required CO conversion efficiency to reduce the tailpipe CO emission to 1 g/kwh. The modern TWC system is adequate to reduce the CO emission. But in order to meet the future emission regulations (*i.e.* successors of the EPA Tier-4 and Euro-VI standard), improved mixture preparation strategy is needed to reduce the under-mixed diesel vapor, hence the engine-out CO emission.

Another issue at low load is the difficulty of robust flame propagation. RCCI enables flame-less combustion but the fuel conversion is hardly complete [101]. Thus it is still desired to keep the flame temperature high enough for robust flame propagation. Both simulation- and experiment-based fine tune of the EGR upper limit is needed. The authors believe that warm EGR and internal EGR could also improve the robustness of the flame propagation at low load.

Although with a compression ratio as high as 17.1, chemically-driven spontaneous ignition of end-gas, *a.k.a.*, engine knock, is not observed even in the tested operation condition with highest load and lowest speed. This is due to the combination of multiple effects: a) distributed ignition

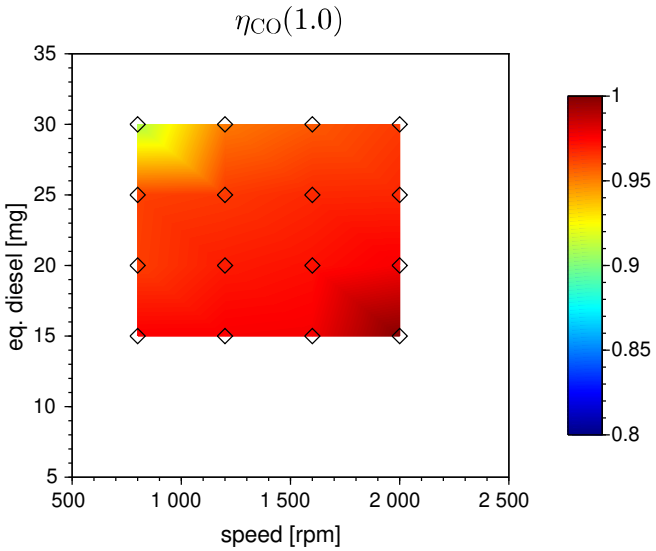

Figure 4.51: The required TWC's CO conversion efficiency such that the tailpipe CO emission is 1 g/kwh.

kernel, b) spray-enhanced turbulence, c) high anti-knock index (AKI) of NG, d) small combustion chamber size. But in engines with larger bore size, engines with boosted intake, engines run with low AKI NG, and aged engines with carbon deposit on the wall, knock is likely to happen. In case of engine knock, the operation envelope of the proposed stoichiometric dual fuel combustion is compromised at low speed.

In the case that an upper limit of the peak pressure rising rate (PPRR) needs to be enforced, the low speed and high load operation may also need be avoided, as illustrated by the Fig. 4.52.

The exhaust temperature of an engine should be confined to avoid damaging the mechanical parts, but also adequately warm to enable efficient after-treatment operation. As a consequence of stoichiometric combustion, the temperature of the combustion product is often higher than that in lean burn engine. In this research, the exhaust temperature is represented by the "blow-down" temperature T_{blow}. The "blow-down" temperature is calculated by assuming an isentropic "blow-down" to the atmospheric pressure $p_0 = 1$ bar following the EVO,

$$T_{blow} = T_{EVO} \left(\frac{p_0}{p_{EVO}} \right)^{\frac{\gamma-1}{\gamma}}, \tag{4.8}$$

where T_{EVO} and p_{EVO} are the temperature and pressure in the cylinder immediately before EVO;

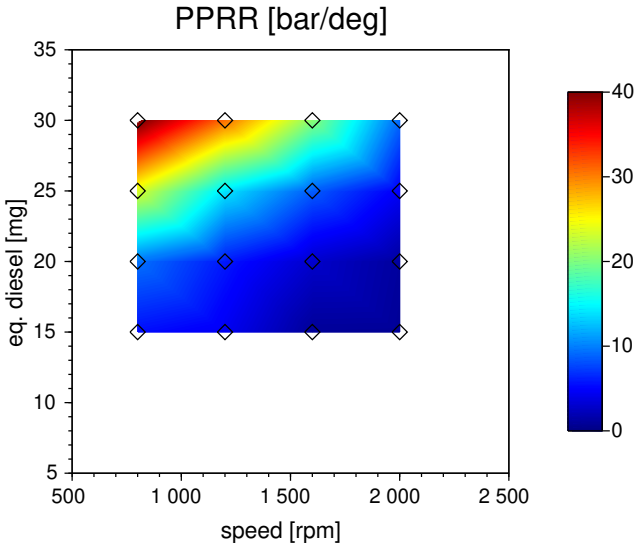

Figure 4.52: The PPRR at different operation conditions.

$\gamma = 1.3$ is the estimated ratio of heat capacities. As shown in Fig. 4.53, the T_{blow} increases with both load and speed. The low EGR rate is responsible for the high T_{blow} at high load. With increasing the engine speed, the available time for heat transfer is shorter, the overall combustion phase is delayed, peak temperature and heat transfer to wall is reduced, and work production is not efficient. All these factors result in higher T_{blow} at high speed.

The thermal load consists of two part, the heat transfer to the wall and the enthalpy flow attached to the exhaust gas. Excessive heat transfer to the wall could damage the piston top, piston rings, cylinder liner, and the exhaust port, while excessive exhaust enthalpy could damage the turbocharger. In this research, the combined thermal load $\dot{q}_{combined}$ is estimated by subtracting work output from the fuel energy input,

$$\dot{q}_{combined} = \frac{1}{2}\left(m_f Q_{LHV} - w_{IVC}^{EVO}\right) N, \tag{4.9}$$

where m_f is the equivalent diesel mass per cycle; Q_{LHV} is the lower heating value of diesel; w_{IVC}^{EVO} is the indicated work from IVC to EVO; N is the engine speed. The estimation is valid unless the combustion efficiency is far below 1. As shown in Fig. 4.54, the effect of engine speed is more pronounced comparing to Fig. 4.53. This is due to the higher fuel flow rate at higher engine speed.

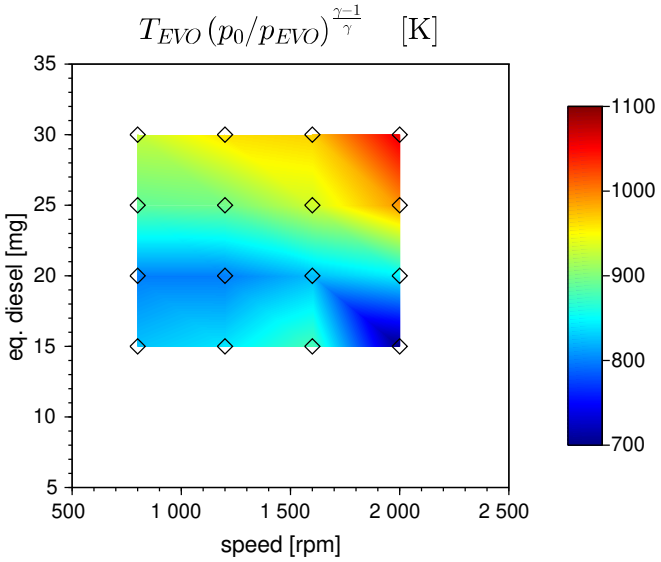

Figure 4.53: The blow-down exhaust temperature at different operation conditions.

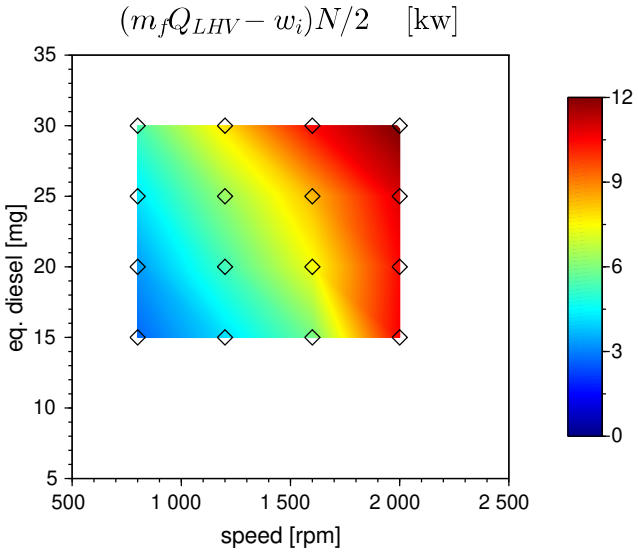

Figure 4.54: The thermal load at different operation conditions.

Chapter 5

SI Engine Simulation and Flame Propagation Model

Two major strategies exist to simulate the propagation of premixed flame in CFD. One is to resolve the flame structure from fundamental conservation laws. The other is to use a flame propagation model to mimic the premixed combustion. In the first strategy, the computational grid resolution must be sufficiently fine to capture the flame structure, which is often orders of magnitude smaller than the problem domain size. The mass and energy transport properties must also be precise due to their significant effects on the flame propagation speed and flame structure. The conservation laws must be coupled with a chemical kinetics model, often computationally expensive, to resolve the chemical behavior in both the thermal layer and the reaction layer of the premixed flame. Due to the high computational cost of the first strategy, it is often inapplicable in practical SI engine simulations. Contrary to the first strategy, the flame propagation model is more efficient. In a flame propagation model, the flame propagation speed is accurately modeled without resolving the flame structure. Thus, the grid resolution can be coarse and the accuracy of the transport properties of the fluid is less important. The chemical kinetics model is not needed, unless kinetically-controlled reactions in the burned region or chemically-driven ignition in the unburned region was of interest.

The G-equation model is a popular flame propagation model adopting the second strategy. Tan and Reitz [98] developed and implemented a straightforward G-equation model for their customized engine CFD software KIVA [2]. They validated their simulation tool against quiescent chamber SI experiment data, as well as test cell data from SI engines with pancake and bowl-in-piston combustion chamber design. It was shown that the predicted transient chamber/cylinder pressure and flame surface location agree with the measurement. Practical engine development expects not only accurate heat release prediction, but also basic information about the chemical processes from the engine CFD simulation. In order to extend the G-equation model to predict the burned region NO_x formation, Liang and Reitz [52] included a nine-reaction NO_x mechanism

in their G-equation calculation. The nine-reaction NO_x mechanism they used does not involve any of the fuel compositions and has small effect on the heat release, hence works in parallel with the G-equation model without conflict. Liang et al. [53] further extended their G-equation model for knock prediction by including chemical kinetics calculation ahead of the flame front with a 22-species reduced iso-octane reaction mechanism. The model was tested in the simulations of a high compression ratio, boosted GDI engine, and demonstrated satisfactory knock prediction capability. Unlike the thermal NO_x formation, the engine knock, *a.k.a.* the kinetics-driven spontaneous ignition of the end gas, involves the fuel species in the mixture and has dominant effect on the local heat release. Thus heterogeneous treatment is needed for the flame "band" and the unburned region. The heterogeneous treatment poses challenges in the implementation and adds complication to the model. Besides, reliable but expansive chemical kinetics calculation dose not match with the phenomenological nature of the G-equation model. A simple and effective knock prediction method without the requirement of heterogeneous treatment for the unburned region and the flame "band" is needed for the G-equation flame modeling technique.

The Livengood-Wu integral [57] is a classic and simple method to predict the kinetics-driven spontaneous ignition of fuel-air mixtures. With the Livengood-Wu integral method the ignition timing of a system undergoing temperature and pressure variation can be predicted. The Livengood-Wu method is based on the ignition delay information with constant pressure and temperature, $\tau_{ig}(p, T)$. The ignition delay under varying condition, t_{ig}, is determined by:

$$\int_0^{t_{ig}} \frac{1}{\tau_{ig}(p(t), T(t))} \, \mathrm{d}\, t = 1. \tag{5.1}$$

The simplicity and effectiveness of the Livengood-Wu integral make it a good candidate for the knock prediction capability in the G-equation model.

5.1 G-Equation Model with Knock Prediction Capability

In this study, a G-equation model is developed and implemented in the customized KIVA software. A method inspired by the Livengood-Wu integral is used to enable the knock prediction with the G-equation model. The final model [104] is capable of mimicking three kinds of combustion events:

flame propagation, diffusion-controlled combustion, and chemically-driven ignition. It should be noted that the model developed in this study is a phenomenological model. While the model predicts the heat release and pressure variation in the engine combustion chamber and provides a simple and reliable framework upon which emissions formation sub-models can operate, it cannot resolve the fundamental processes in either flame propagation or spontaneous ignition. Conclusions about the flame structure and the chemical kinetics should not be made based on any result generated by this model.

In the simulation of SI engine operation, the flame surface is defined as an iso-surface of an evolving scalar field $G(\mathbf{x}, t)$. For convenience, $G(\mathbf{x}, t) = 0$ is chosen to represent the flame surface. Now, pick a moving point $\mathbf{x}_f(t)$ that always sits on the flame surface, such that:

$$G(\mathbf{x}_f, t) = 0. \tag{5.2}$$

The instantaneous velocity of this moving point is $\frac{\mathrm{d}\,\mathbf{x}_f}{\mathrm{d}\,t}$. Because the G at $\mathbf{x}_f$ should always be 0, have:

$$\frac{\partial G}{\partial t} + \nabla G \cdot \frac{\mathrm{d}\,\mathbf{x}_f}{\mathrm{d}\,t} = 0. \tag{5.3}$$

The instantaneous velocity of $\mathbf{x}_f$ can be modeled as:

$$\frac{\mathrm{d}\,\mathbf{x}_f}{\mathrm{d}\,t} = \mathbf{u} - \frac{\nabla G}{\|\nabla G\|}\frac{\rho_u}{\rho}S_T, \tag{5.4}$$

where $\mathbf{u}$ is the local gas velocity, ρ_u is the unburned gas density, S_T is the turbulent flame speed relative to the unburned gas. Thus $\frac{\rho_u}{\rho}S_T$ is the turbulent flame speed relative to the local gas. Substitute Eq. 5.4 into Eq. 5.3, and get the governing equation for G:

$$\frac{\partial G}{\partial t} + \mathbf{u} \cdot \nabla G = \frac{\rho_u}{\rho}S_T\|\nabla G\|. \tag{5.5}$$

It should be noted that the Eq. 5.5 is not a necessary condition for correct flame propagation prediction, and it only needs to be satisfied in the vicinity of the $G = 0$ iso-surface. Deep in the burned and unburned region, arbitrary treatment of the G scalar field is valid as long as the smoothness of G and ∇G is preserved, and abnormal ignition ahead of the flame front is avoided.

In order to model the S_T in the right-hand side of the Eq. 5.5, it is needed to consider the laminar flame speed S_L of a given mixture. Metghalchi and Keck [62] developed an empirical fitting for S_L, in which the effects of fuel, diluent, temperature, and pressure were considered:

$$S_L = S_L^{ref} \max\{0, 1 - 2.1X_d\} \left(\frac{T_u}{298.15\ \text{K}}\right)^{2.18-0.8(\phi-1)} \left(\frac{p}{1\ \text{atm}}\right)^{-0.16+0.22(\phi-1)}, \tag{5.6}$$

where S_L^{ref} is the laminar flame speed of the given fuel and air mixture at 298.15 K and 1 atm, X_d is the molar fraction of diluent gas, ϕ is the equivalence ratio. The reference laminar flame speed is fitted by a quadratic curve:

$$S_L^{ref} = \max\left\{0, b_m + b_2(\phi - 1.05)^2\right\}, \tag{5.7}$$

where b_m and b_2 are fitting parameters for the given fuel. The maximum laminar flame speed locus of $\phi = 1.05$ is appropriate for most of the hydrocarbon and oxygenated fuels used in internal combustion engine. Peters [76] developed the model for turbulent flame speed in the corrugated flame regime and the thin reaction zone regime:

$$\frac{S_T}{S_L} = 1 + \frac{u'}{S_L}\left(-kDa + \sqrt{k^2Da^2 + 4kDa}\right), \tag{5.8}$$

where u' is the turbulence intensity, the constant $k = 0.195$. The Damköhler number is defined as:

$$Da = \frac{S_L l}{u' l_f}, \tag{5.9}$$

where l is the integral length scale of the turbulent flow field, l_f is the thermal layer thickness:

$$l_f = \frac{k_u/c_{p_u}}{\rho_u S_L}, \tag{5.10}$$

where $\frac{k_u}{c_{p_u}}$ can be approximated with using gram, centimeter, and second as the unit of mass, length, and time [94]:

$$\frac{k_u}{c_{p_u}} \approx 2.58 \times 10^{-4} \left(\frac{T}{298.15\ \text{K}}\right)^{0.7}. \tag{5.11}$$

Substitute the approximation into Eq. 5.10 and 5.9:

$$Da = \frac{3876 S_L^2 l \rho_u}{u' \left(\frac{T_i}{298.15 \text{ K}} \right)^{0.7}}, \tag{5.12}$$

where T_i is the flame inner layer temperature, assumed to be 1500 K [52].

The scalar field G is used to determine the local reaction advancement ξ,

$$\xi = \max \left\{ 0, \min \left\{ G/l'_f + 0.5, 1 \right\} \right\}, \tag{5.13}$$

where l'_f is a predetermined thickness. In this study, l'_f is left as a model parameter that can be set by the user. The local mass fraction Y_i is determined by ξ:

$$Y_i = \xi Y_i^b + (1 - \xi) Y_i^u, \tag{5.14}$$

where the burned gas mass fraction Y_i^b is either at the state where at least one reactant (fuel or oxygen) is depleted, or the equilibrium state. It should be noted that the flame structure from the Eq. 5.13 is not designed to represent the actual flame structure found in any premixed combustion event.

In SI engines, the fuel-air mixture is consumed by either flame propagation or chemically-driven spontaneous ignition, *a.k.a.* the SI engine knock; In CI engines, the combustion is initiated by the spontaneous ignition of fuel-air mixture and the subsequent bulk heat release from the exploding mixture. While the G-equation model simulates the flame propagation, the knock in the unburned region in SI engine as well as the spontaneous ignition in CI engine still need to be modeled. In order to construct an unified combustion model, heterogeneous treatment for the flame "band" and the unburned region must be avoided. It is maintained that the local chemical progress is determined by $G(\mathbf{x}, t)$ via Eq. 5.13 and 5.14. But the $G(\mathbf{x}, t)$ is allowed to be altered by another scalar field $H(\mathbf{x}, t)$. The scalar field $H(\mathbf{x}, t)$ is governed by the transport equation with a source term inspired by the Livengood-Wu integral:

$$\frac{\partial H}{\partial t} + \mathbf{u} \cdot \nabla H = \frac{1}{\tau_{ig}(X_f, X_{\text{O}_2}, p, T)}, \tag{5.15}$$

where X_f and X_{O_2} are the local molar fractions of fuel and oxygen, respectively. The $\tau_{ig}(X_f, X_{O_2}, p, T)$ data is generated by 0-D simulations with a detailed reaction mechanism. In the present study, the efficient chemical kinetics solver [106] presented in Chap. 4 is used to generate the ignition delay table for the given fuel. An open-source regular grid B-spline interpolation code [110] is used to calculate the continuous function $\tau_{ig}(X_f, X_{O_2}, p, T)$ at any given local state. In the simulation with the unified combustion model, $G(\mathbf{x}, t)$ and $H(\mathbf{x}, t)$ are orchestrated to calculate the local gas composition. By default, the Eq. 5.5 and 5.15 evolve independently. The interaction between G and H happens upon the ignition event. During each time step of the simulation, the unified combustion model checks whether the collection (Ψ) of igniting CFD cells is empty. The Ψ includes all cells that are: a) ignited according to H, b) away from the flame front. That is: $G(\mathbf{x}^c_{i\in\Psi}, t) < -\frac{l'_f}{2}$, and $H(\mathbf{x}^c_{i\in\Psi}, t) \geq 1$, where $\mathbf{x}^c_i$ is the centroid location of cell i. Upon ignition, i.e. $\Psi \neq \emptyset$, the G field undergoes a special operation. For the cells not in Ψ:

$$G(\mathbf{x}, t) :\leftarrow \max\left\{G(\mathbf{x}, t), -\min_{i\in\Psi}(\|\mathbf{x} - \mathbf{x}^c_i\|)\right\}. \tag{5.16}$$

For the cells in Ψ, one can simply set the G to a value between $-\frac{l'_f}{2}$ and $\frac{l'_f}{2}$. The above procedure alters the G field to initiate new ignition kernels surrounding the region that H grows beyond 1. In the vicinity of the newly-initialized ignition kernels, the G field is essentially a negative distance function to the ignition kernel.

Although the unified model is developed primarily for simulation of SI engine operation with possible knock, the model is also naturally applicable for CI engine simulation. In CI engine simulation, the ignition delay is captured by the Livengood-Wu integral. After ignition, the "burned region" expands quickly, and the diffusion-controlled combustion in the "burned region" is simulated equivalent to assuming the Burke-Schumann limit. Such simulation method is specifically appropriate for CI combustion with considerable premixed flame propagation, as in the advanced PPC and RCCI concepts.

5.2 Premixed Flame Propagation in a Constant Volume Chamber

In order to test the unified combustion model, the simulation is compared with an SI combustion experiment in a constant volume chamber.

The primary functionality of this constant volume chamber is to conduct spray combustion study. In order to mimic the high-temperature and high-pressure in-cylinder condition of a heavy duty diesel engine, SI premixed combustion of acetylene is used to elevate the in-cylinder temperature and pressure in prior to the liquid fuel injection. In the operation of the constant volume chamber, acetylene, oxygen, and nitrogen are premixed and inducted into the constant volume chamber; The spark plug discharges and initiates the premixed combustion of acetylene, elevating the pressure and temperature. Once the pressure and temperature drop to the predetermined spray combustion initial condition by the heat transfer, the liquid fuel injection is triggered, and the spray combustion data is recorded. In this study, the pressure trace during the acetylene combustion phase is used to validate the G-equation flame propagation simulation result.

The constant volume chamber is of cylindrical shape. Its diameter is 110 mm and its height is 65 mm. The spark plug is mounted on the side wall at the height of the 32.5 mm, half of the total height. The single-block full-chamber computational grid for the constant volume chamber has 51480 cells, not nearly enough to resolve the flame structure, but adequate for the unified combustion model developed in this study. The computational grid and the spark location is shown in Fig. 5.1. The initial mass fraction of acetylene, oxygen, and nitrogen of the fresh mixture are $Y_{C_2H_2} = 0.0265$, $Y_{O_2} = 0.3321$, and $Y_{N_2} = 0.6414$, respectively. In prior to the spark plug discharge, the quiescent mixture has a pressure of 15.5 bar and a temperature of 378 K. In the simulation, the proposed combustion model extracts turbulence intensity and length scale from the RNG k-ϵ turbulence model [32].

The comparison between the predicted pressure trace and the measured pressure traces is shown in Fig. 5.2. As clearly shown, the predicted burning duration matches well with the measured burning duration. The PPRR in the simulation happens approximately from 80 to 100 ms after the spark discharge, and is slightly higher than the PPRR measured from the experiments. The

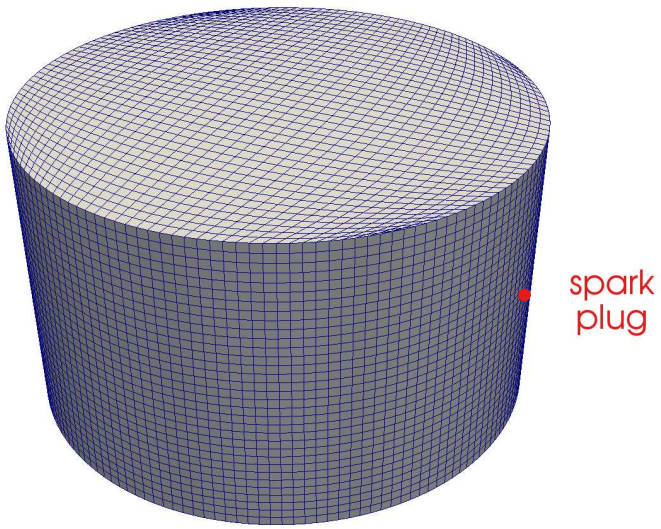

Figure 5.1: The computational grid of the constant volume chamber and the location of the spark plug.

evolution of the $G = 0$ iso-surface, i.e. the center of the artificial flame, is visualized in Fig. 5.3. At 40 ms after the spark discharge, the pressure rise is still small, but the size of the burned region is already significant. This phenomenon is due to the vast density difference between the burned gas and the unburned gas, and was also observed previously by Schlieren visualization technique [49]. Also shown in Fig. 5.3 is the temperature profile on a horizontal and a vertical cross section. It can be seen that a noticeable temperature difference exists between the earlier-burned gas and the later-burned gas, although the mixture is perfectly homogeneous before combustion. Such temperature difference is due to the sequence of the local heat releasing and the local compression. With the almost-instantaneous local heat releasing being in the earlier phase of the relatively slower pressure rising and local compression, a higher final temperature can be reached upon the completion of the flame propagation.

The comparison between the predicted and measured SI premixed combustion demonstrates the capability of the G-equation model in simulating flame propagation with reasonable accuracy.

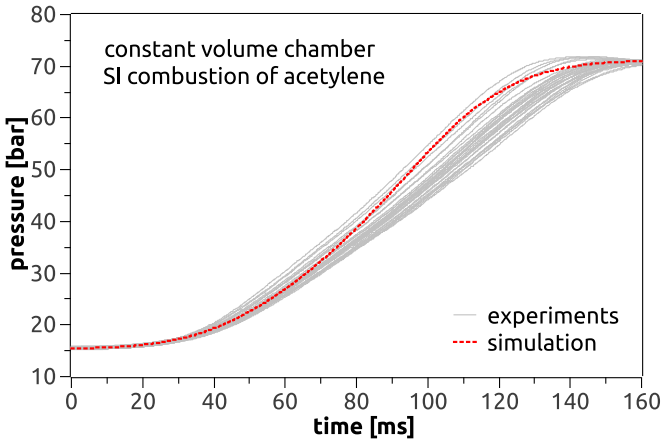

Figure 5.2: The predicted and measured pressure variation in the constant volume chamber during acetylene SI combustion event.

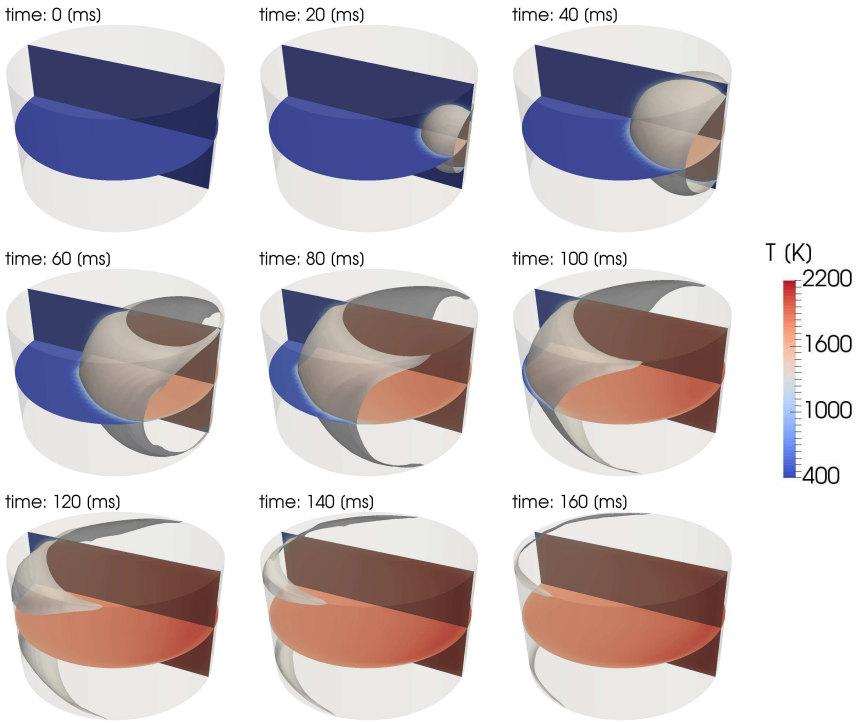

Figure 5.3: The predicted temperature on the cross sections and the $G = 0$ iso-surface during acetylene SI combustion event.

5.3 Swirl-Dominant GDI Engine

Comparing to the gasoline SI engine with PFI mixture preparation method, GDI engine has advantages such as accurate cycle-by-cycle fuel metering, effective and clean cold start, strong spray cooling effect, low octane requirement, *etc.* In the present study, the unified flame propagation and spontaneous ignition model is used to simulate the operation of a high compression ratio, swirl-dominant GDI SI engine. The tested engine is a high compression ratio GDI engine derived from Ford's small bore diesel engine platform, *a.k.a.* DIATA (direct-injection, aluminum, through-bolt assembly). The key parameters of the tested GDI engine are listed in Tab. 5.1. As most of the small bore diesel engines, the DIATA engine has a swirl-dominant flow configuration, which generates rotational in-cylinder fluid motion in the horizontal plane. The swirl-dominant in-cylinder flow pattern at the moment of IVC can be fitted by a function in the radial direction, which enables the use of closed-chamber CFD computation. While the multi-hole injector is mounted at the center of the cylinder, the spark plug needs to be offset. As the consequence of the off-centered spark location, sector computational grid cannot be used. In the present study, the closed-chamber simulation uses a full-chamber grid (shown in Fig. 5.4), and runs from the moment of IVC to the moment of EVO.

The baseline operation condition of the GDI engine test has the rotational speed of 1200 rpm and the nominal IMEP (indicated mean effective pressure) of 5 bar. In the experiment, the pressure of the intake manifold is slightly throttled down to 12 psi. Such baseline configuration represents a typical freeway cruising operation condition of a down-speed, down-size GDI engine. In the baseline simulation, the ignition delay data of PRF95 fuel (95% iso-octane, 5% n-heptane, by liquid volume) is supplied to the unified flame propagation and spontaneous ignition model to predict the potential

Table 5.1: Key parameters of the single cylinder swirl-dominant GDI test engine.

bore [mm]	70.0	nozzle diameter [mm]	0.10
stroke [mm]	78.0	fuel delivery type	common rail
compression ratio	16.0	rail pressure [bar]	200
IVC angle [°]	200	intake type	naturally aspirated, throttled
injector type	multi-hole	swirl ratio	1.5
number of nozzles	6	EGR type	not mounted
distribution cone angle [°]	148	spark offset [mm]	14

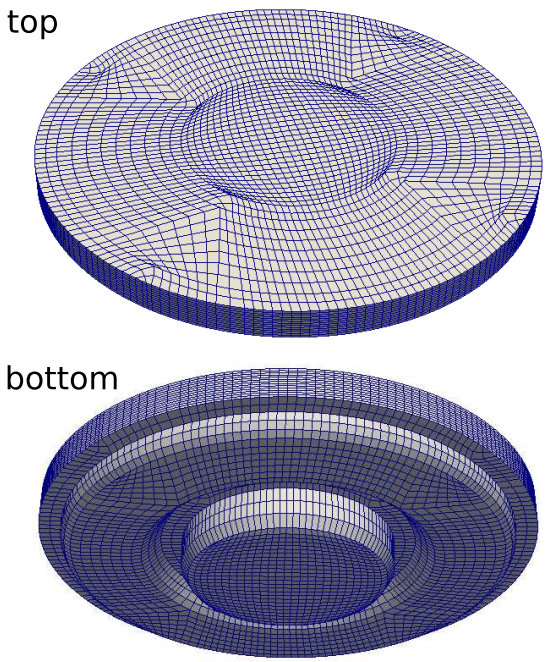

Figure 5.4: The computational grid of the tested GDI engine, looking from the top and the bottom.

knocking of the engine operation. The ignition delay data is evaluated prior to the engine simulation using a reduced PRF mechanism [102]. The tabulated ignition delay is visualized in Fig 5.5 and 5.6 for the constant pressure of 20 and 40 bar, which are approximately the pre-ignition in-cylinder pressure and the and post-combustion (pre-knock, if any) in-cylinder pressure, respectively.

In the baseline test, a single gasoline injection is applied at 210° crank angle (10° after IVC). The spark signal is triggered at 335° crank angle in the experiment. In the simulation, the SOC (start of combustion) timing is set at 344° crank angle according to the measured pressure trace. It should be noted that the electronic response of the actual ignition system, as well as the development of the electric discharge in the gas medium are responsible for the delay between the spark signal and the SOC, and are out of the scope of the present model. The measured and predicted baseline pressure traces are plotted in Fig. 5.7. It is noticeable that the predicted peak pressure and post-combustion pressure are higher than those from the measurement. This is due to the fact that the measurement is performed in an optical engine that has compromised sealing performance between the piston ring and the cylinder liner. It is expected that the gas blow-by in the optical engine operation reaches the level of 10% of the total mass, while this value of a well functioning

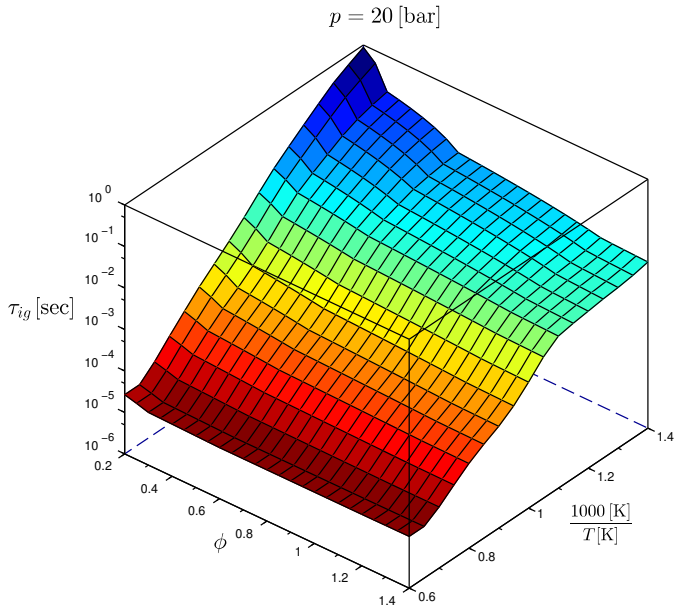

Figure 5.5: The ignition delay data of PRF95 visualized at a constant pressure of 20 bar.

production engine is at the level of 1%.

Both the predicted and the measured baseline operation show smooth combustion and pressure rise that is free of knock. In order to test the knock prediction capability of the unified combustion model, variations of the baseline case are generated by swapping the PRF95 ignition delay data with that of PRF90 and PRF85. The transient variation of the $G = 0$ iso-surface, *i.e.* the flame surface, and the volume rendering of the scalar field H in the unburned region are visualized in Fig. 5.8 for the simulations with the three octane ratings. It is found that the three octane ratings result in similar combustion process except near the end of the combustion, when knock happens in the case with the ignition delay data of PRF85. Before the crank angle of 364°, the location of the $G = 0$ iso-surface propagates in the same pace for the three cases, consuming most of the mixture in the combustion chamber; The level of H accumulates noticeably faster with lowering the octane rating, without affecting the evolution of G. At the crank angle of 365°, a new ignition kernel is generated in the case of PRF85 as the H rises above 1, indicating the spontaneous ignition of the end-gas, *a.k.a.* knocking. For the case with PRF90, although no additional ignition kernel is developed before the end of the flame propagation, the H does rise to a dangerous level close to 1. In the reality, where cycle-to-cycle variation occur, frequent knocking is still expected with

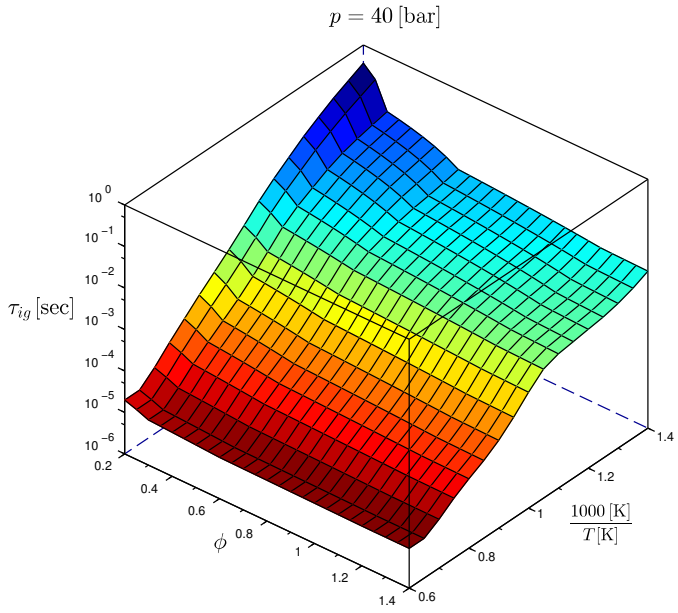

Figure 5.6: The ignition delay data of PRF95 visualized at a constant pressure of 40 bar.

PRF90, despite of the knock-free simulation result. For the case with PRF95, the H is well below 1 upon the end of the combustion, indicating low knock risk.

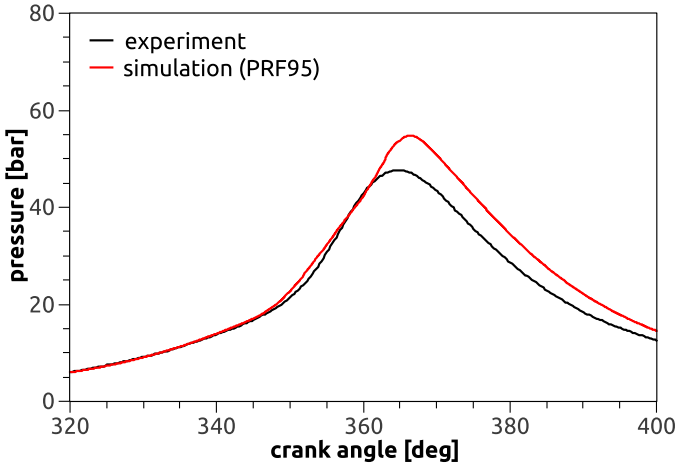

Figure 5.7: The predicted (with PRF95) and measured pressure trace of the tested GDI engine.

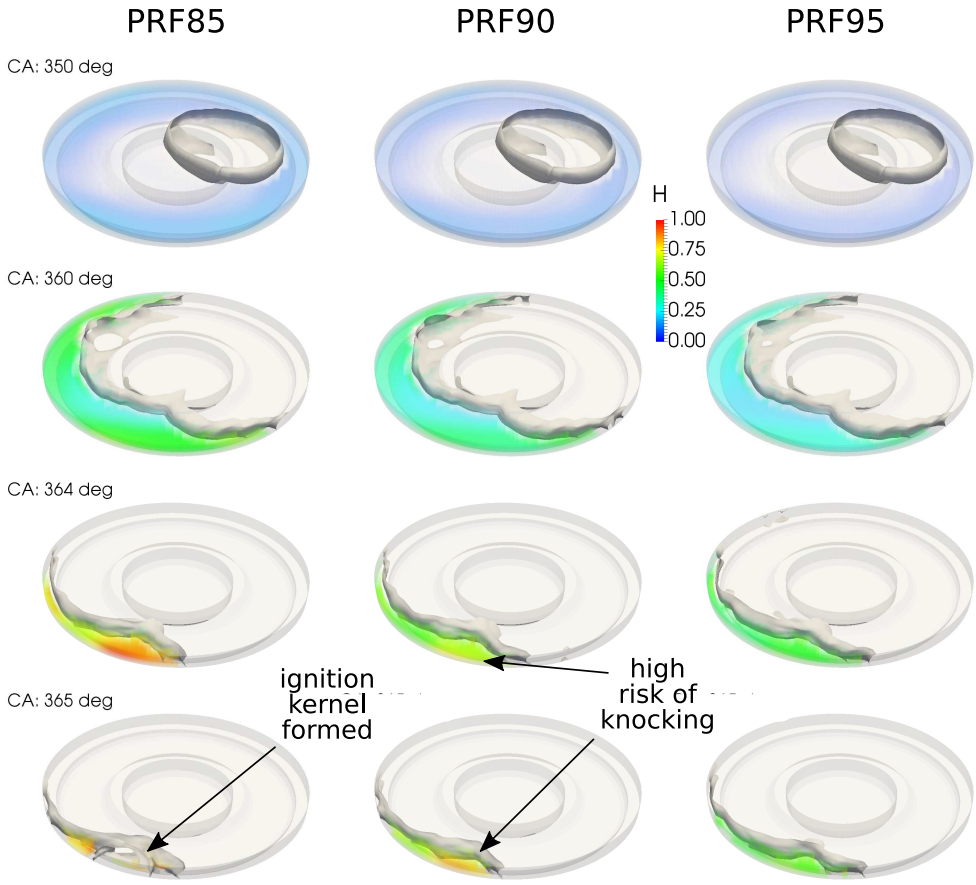

Figure 5.8: The $G = 0$ iso-surface and the volume rendering of H during the operation of the tested GDI engine with reference fuels of different octane ratings.

Chapter 6

Summary and Future Works

This dissertation describes the computational studies conducted by the author on the mixture preparation in internal combustion engines. The studies cover both development of CFD sub-models for mixture preparation and combustion, as well as the application of these models in CI engine study and innovation. The major accomplishments and discoveries are summarized in this chapter. The recommendations for the future research directions are also provided.

6.1 Model Development

In the present work, a droplet evaporation model is developed. The evaporation model adopts sophisticated and proven methods to evaluate the thermal properties and transport properties of non-ideal multi-component fluids. A new VLE solver is included to resolve the state at droplet surface. The efficient quasi 1-D method is retained from the previous model to resolve the problem of liquid phase transport. Classic gas phase transport models are selected for efficient evaluation of mass and heat transfer rate. The droplet evaporation computation is validated by existing experimental results of suspending, floating, and multi-component droplets. The effect of relative motion between gas and droplet is verified against a classic empirical correlation. The droplet evaporation model is implemented with modern software engineering practices, and is integrated in the KIVA CFD program. The new code is used to simulate the standard Spray G experiment. The predicted vapor and liquid penetration of Spray G agrees with those from measurements. The result from the new code shows level of fuel mass fraction the same as that by ANL's LES result. The new droplet evaporation model is readily applicable in spray and engine simulations. Future improvements of the model may focus on the efficiency of the arithmetics and the performance of the code.

The new droplet breakup model developed in the present study achieved seamless integration of two interacting and competing droplet breakup modes: aerodynamic breakup and flashing breakup. The sub-models for bubble nucleation and bubble growth, which are essential processes for flashing droplet, are added to the existing TAB model, an aerodynamic breakup model. The existence of the internal bubbles affects the behavior of the TAB model, as it alters the overall size and dynamic properties of the droplet. A void fraction criterion for flashing breakup is added to the model and competes with the TAB's droplet deformation criterion. Upon breakup due to either criterion, unified computation method based on conservation laws is used to determine the state and quantity of the secondary droplets. Single droplet breakup computations are used to illustrate the behavior of the unified aerodynamic and flashing breakup model. The new breakup model is integrated into the KIVA program and is used to simulate a superheated spray experiment. The predicted result is validated against experimental observations. The unified breakup model provides the essential tool for the future discovery of flash-boiling-enhanced mixture preparation technologies that can potentially generate mixture with superior homogeneity.

In the present study, an efficient chemical kinetics solver is developed to solve the local chemical kinetics problem in CI engine CFD simulation. A semi-analytical evaluation of the Jacobian matrix is derived for the initial value problem of the local chemical kinetics. The approximate Jacobian matrix is either solved by a direct linear solver or used to construct the preconditioner for the Krylov subspace method. The two strategies are systematically tested using reaction mechanisms of different sizes, and with different initial conditions. The new method shows superior performance with appropriate strategy selection comparing to the existing code. A guideline is provided for the problem-size-based selection of the solver strategy. The presented methods are implemented in the KIVA code for the simulation of CI engine operation. Simulations of a diesel engine are conducted to demonstrate the performance and accuracy of the new code. Future improvements of the solver may focus on the tabulation and reusing of the Jacobian matrix and preconditioning matrix (and its factorization), over the FVM cell boundary and through the time steps.

For the simulation of SI engine, an unified phenomenological model is developed to mimic the flame propagation and the engine knock in the combustion process. The model combines a G-equation flame propagation model with a knock prediction model inspired by the Livengood-Wu

integral. Both sub-models and their interactions are described in detail. The local value of G is connected with the advancement of the chemical reaction to determine the local gas composition in both burned and unburned region. The unified combustion model is implemented on the KIVA platform and is used in a demonstrative simulation of a GDI engine's knock-free operation. The knock prediction capability is tested by reducing the octane rating of the surrogate fuel, based on which the ignition delay data is generated. In order to further extend the usefulness of the unified combustion model, future efforts may focus on the improvement of flame speed correlations, the expansion of the flame speed data collection, development of a detailed spark discharge model, *etc.*

6.2 CI Engine Study and Innovation

As an effort to understand the interaction between the chemical kinetics and the fuel-air mixing in CI engine, the concept of ignition phase curve is proposed based on a simple single injection scheme. 3-D CFD simulation with the new chemical kinetics solver is used to generate the ignition phase curve covering the PPC regime and DICI regime. The effects of the combustion chamber geometry, the gas temperature, the engine load, and the overall equivalence ratio are studied by numerical simulation. The major conclusions and discoveries based on the study are:

- The onset of the cool flame takes place in the lean region, which is not significantly altered by SOI variation in the PPC regime; The high temperature ignition happens in the near stoichiometric and rich region, which shrinks with advancing SOI timing in the PPC regime. These cause the PPC's stable cool flame onset timing, as well as its strong and inverted SOI control authority over high temperature ignition timing.

- Due to the existence of the most rapidly igniting equivalence ratio regardless of the SOI timing, the SOI's control authority over the combustion phasing disappears in the PPC operation under high load.

- The combustion chamber geometry has considerable effects on the ignition phase curve. It is found that the ignition phasing is delayed in case with either significant spray penetration on solid wall or heat loss in the squish region. While the ignition is enhanced with ineffective mixing near the fuel-rich stagnation point.

- Ignition is more sensitive to the intake temperature in the PPC mode than in conventional DICI mode. Within the PPC mode, it is more sensitive to intake temperature with deeply advanced SOI than with moderately advanced SOI.

- The PPC heat release duration is longer in low load operation where the mixture has low energy density and combustion temperature. The kinetics-controlled reactions are not fully activated due to the low combustion temperature. The DICI operation has longer heat release duration under high load where the reaction is limited by the slow mixing of fuel and air.

- Over-lean operation has low combustion efficiency in both the PPC and DICI regime, due to the low combustion temperature; While the survival of locally rich region through the combustion event compromises the combustion efficiency at higher load.

The new chemical kinetics solver is also used in the study of GDCI engine operation where the GDCI operation is compared with the common diesel-fueled engine operation. Simulations are conducted to study the combustion's sensitivity to intake temperature, boost pressure, compression ratio, and warm EGR ratio. Recommendations are provided to achieve the diesel-like controllability in GDCI engine. The pollutants emissions are correlated to the instantaneous parameters of the mixture at the moment of ignition, providing insights about the fundamental mechanisms of the emission reduction by adopting GDCI combustion. Major conclusions include:

- In case that diesel-like ignition characteristics are desired, the authors suggest apply boost, and increase the IVC temperature by applying warm EGR, while maintain a moderate compression ratio (*i.e.* 16.0).

- The existence of the signature inverse SOI-ignition relation of the PPC regime depends on the effectiveness of over-mixing in reducing the maximum ϕ in the combustion chamber over a range that ignition has sufficient ϕ-sensitivity.

- Apart from NO_x's well-known dependency on the overall T, ϕ distribution, and dilution, the local burning timing relative to the overall combustion process is also important. With the same local ϕ, mixture burned earlier generates more NO_x than the later-burned mixture.

A first-of-its-kind stoichiometric dual fuel CI engine is studied with the KIVA CFD program with the new chemical kinetics solver. The present study proposes the concept of high compression ratio stoichiometric diesel - natural gas dual fuel engine. The concept developed in this work uses distributed diesel ignition source to initiate knock-free combustion under high compression ratio. EGR and throttling are applied to generate stoichiometric mixture under different loads. Stoichiometric combustion enables the use of the maintenance-free TWC instead of more complicated after-treatment systems. 3-D CFD computations are conducted to demonstrate the usefulness of the proposed concept at a wide range of operation conditions. The limitations confining the operation envelope of the proposed concept are identified and explained. Preliminary results of the new engine concept show that:

- Comparing to the existing lean burn dual fuel engines, the proposed technology is able to satisfy the stringent emission regulation with TWC after-treatment system. Comparing to the existing SI natural gas engines, the proposed technology operates with higher compression ratio and has greater efficiency potential.
- The stoichiometric dual fuel operation is deteriorated at low load with high CO emission and low flame propagation robustness.
- At low speed and high load, the operation is limited by the PPRR, as well as the potential engine knock, which is not encountered in the present study due to the test engine's small combustion chamber and fast flame propagation.
- At high speed and high load, the operation is limited by the thermal load and exhaust temperature.

Future efforts in the following directions are believed by the author to be able to improve and extend the stoichiometric dual fuel operation:

- To reduce the under-mixing CO emission by splitting the diesel injection and improving the gas flow strategy.
- To extend the operation envelope toward lower load by applying warm EGR or internal EGR.
- To study the potential of stoichiometric dual fuel operation with boosted intake.

References

[1] B. Abramzon and W.A. Sirignano. Droplet vaporization model for spray combustion calculations. *International Journal of Heat and Mass Transfer*, 32(9):1605 – 1618, 1989.

[2] Anthony A Amsden. Kiva-3v, release 2, improvements to kiva-3v. *Los Alamos National Laboratory, Los Alamos, NM, Report No. LA-UR-99-915*, 1999.

[3] William P. Attard, Elisa Toulson, Andrew Huisjen, Xuefei Chen, Guoming Zhu, and Harold Schock. Spark ignition and pre-chamber turbulent jet ignition combustion visualization. In *SAE Technical Paper*. SAE International, 04 2012.

[4] Jennifer C. Beale and Rolf D. Reitz. Modeling spray atomization with the kelvin-helmholtz/rayleigh-taylor hybrid model. *Atomization and Sprays*, 9(6):623–650, 1999.

[5] G. Black, H.J. Curran, S. Pichon, J.M. Simmie, and V. Zhukov. Bio-butanol: Combustion properties and detailed chemical kinetic model. *Combustion and Flame*, 157(2):363 – 373, 2010.

[6] Stephen Busch, Kan Zha, Alok Warey, Francesco Pesce, and Richard Peterson. On the reduction of combustion noise by a close-coupled pilot injection in a small-bore di diesel engine. In *ASME 2015 Internal Combustion Engine Division Fall Technical Conference*, pages V002T06A003–V002T06A003. American Society of Mechanical Engineers, 2015.

[7] Kyungchan Chae and Angela Violi. Mutual diffusion coefficients of heptane isomers in nitrogen: a molecular dynamics study. *The Journal of chemical physics*, 134(4):044537, 2011.

[8] Dar-Lon Chang and Chia-Fon F. Lee. Development of a simplified bubble growth model for flash boiling sprays in direct injection spark ignition engines. *Proceedings of the Combustion Institute*, 30(2):2737 – 2744, 2005.

[9] C Chauveau, F Halter, A Lalonde, and I Gokalp. An experimental study on the droplet vaporization: effects of heat conduction through the support fiber. In *Proc. of 22 nd Annual Conference on Liquid Atomization and Spray Systems (ILASS Europe 2008)*, 2008.

[10] Steve T. Chin and Chia-Fon F. Lee. Numerical investigation of the effect of wall wetting on hydrocarbon emissions in engines. *Proceedings of the Combustion Institute*, 29(1):767 – 773, 2002. Proceedings of the Combustion Institute.

[11] P. L. Chueh and J. M. Prausnitz. Vapor-liquid equilibria at high pressures: Calculation of partial molar volumes in nonpolar liquid mixtures. *AIChE Journal*, 13(6):1099–1107, 1967.

[12] Sung Sik Chung and O. Kawaguchi. An experimental study on the evaporation of freely falling droplet under high temperature and high pressure gas stream. *KSME Journal*, 4(2):172–177, 1990.

[13] Ting Horng Chung, Mohammad Ajlan, Lloyd L. Lee, and Kenneth E. Starling. Generalized multiparameter correlation for nonpolar and polar fluid transport properties. *Industrial & Engineering Chemistry Research*, 27(4):671–679, 1988.

[14] Ting Horng Chung, Lloyd L. Lee, and Kenneth E. Starling. Applications of kinetic gas theories and multiparameter correlation for prediction of dilute gas viscosity and thermal conductivity. *Industrial & Engineering Chemistry Fundamentals*, 23(1):8–13, 1984.

[15] Stephen Ciatti, Michael Johnson, Bishwadipa Das Adhikary, Rolf D. Reitz, and Aaron Knock. Efficiency and emissions performance of multizone stratified compression ignition using different octane fuels. In *SAE Technical Paper*. SAE International, 04 2013.

[16] Stephen Ciatti and Swami Nathan Subramanian. An experimental investigation of low-octane gasoline in diesel engines. *Journal of Engineering for Gas Turbines and Power*, 133(9):092802, 2011.

[17] Scott D Cohen and Alan C Hindmarsh. CVODE, a stiff/nonstiff ode solver in C. *Computers in physics*, 10(2):138–143, 1996.

[18] Elizabeth F. Cooper and Abdul Fattah A. Asfour. Densities and kinematic viscosities of some c6-c16 n-alkane binary liquid systems at 293.15 k. *Journal of Chemical & Engineering Data*, 36(3):285–288, 1991.

[19] Yasuhiro Daisho, Toru Yaeo, Takahisa Koseki, Takeshi Saito, Ryoji Kihara, and Edwin N. Quiros. Combustion and exhaust emissions in a direct-injection diesel engine dual-fueled with natural gas. In *SAE Technical Paper*. SAE International, 02 1995.

[20] Timothy A. Davis. Algorithm 832: Umfpack v4.3—an unsymmetric-pattern multifrontal method. *ACM Trans. Math. Softw.*, 30(2):196–199, June 2004.

[21] Rapier Dawson, Fouad Khoury, and Riki Kobayashi. Self-diffusion measurements in methane by pulsed nuclear magnetic resonance. *AIChE Journal*, 16(5):725–729, 1970.

[22] John E. Dec. A conceptual model of di diesel combustion based on laser-sheet imaging. In *SAE Technical Paper*. SAE International, 02 1997.

[23] John E. Dec and Magnus Sjöberg. Isolating the effects of fuel chemistry on combustion phasing in an hcci engine and the potential of fuel stratification for ignition control. In *SAE Technical Paper*. SAE International, 03 2004.

[24] M Defoort, D Olsen, and B Willson. The effect of air-fuel ratio control strategies on nitrogen compound formation in three-way catalysts. *International Journal of Engine Research*, 5(1):115–122, 2004.

[25] Adam B Dempsey, Scott J Curran, and Robert M Wagner. A perspective on the range of gasoline compression ignition combustion strategies for high engine efficiency and low nox and soot emissions: Effects of in-cylinder fuel stratification. *International Journal of Engine Research*, 2016.

[26] D. E. Diller. Measurements of the viscosity of compressed gaseous and liquid nitrogen + methane mixtures. *International Journal of Thermophysics*, 3(3):237–249, 1982.

[27] ECN. Engine combustion network "spray g", 1 2017.

[28] J. M. N. A. Fareleira, S. F. Y. Li, and W. A. Wakeham. The thermal conductivity of liquid mixtures at elevated pressures. *International Journal of Thermophysics*, 10(5):1041–1051, 1989.

[29] Suya Gao, Mianzhi Wang, and Chia-Fon Lee. Nox reduction in compression-ignition engine by inverted ignition phi-sensitivity. In *SAE Technical Paper*. SAE International, 04 2017.

[30] Hojat Ghassemi, Seung Wook Baek, and Qasim Sarwar Khan. Experimental study on binary droplet evaporation at elevated pressures and temperatures. *Combustion Science and Technology*, 178(6):1031–1053, 2006.

[31] DG Goodwin. An open-source, extensible software suite for CVD process simulation. *Chemical Vapor Deposition XVI and EUROCVD*, 14(40):2003–08, 2003.

[32] Zhiyu Han and Rolf D Reitz. Turbulence modeling of internal combustion engines using rng κ-ε models. *Combustion science and technology*, 106(4-6):267–295, 1995.

[33] Zhiyu Han, Rolf D. Reitz, Peter J. Claybaker, Christopher J. Rutland, Jialin Yang, and Richard W. Anderson. Modeling the effects of intake flow structures on fuel/air mixing in a direct-injected spark-ignition engine. In *SAE Technical Paper*. SAE International, 05 1996.

[34] Zhiyu Han, Rolf D. Reitz, Jialin Yang, and Richard W. Anderson. Effects of injection timing on air-fuel mixing in a direct-injection spark-ignition engine. In *SAE Technical Paper*. SAE International, 02 1997.

[35] Joseph O Hirschfelder, Charles F Curtiss, Robert Byron Bird, and Maria Goeppert Mayer. *Molecular theory of gases and liquids*, volume 26. Wiley New York, 1954.

[36] Ming Huo, Mianzhi Wang, and Chia-Fon Lee. Computational study of the equivalence ratio distribution from a diesel pilot injection with different piston geometry, injection timing and velocity initialization in a hsdi engine. In *SAE Technical Paper*. SAE International, 04 2014.

[37] Lama Itani and Lyle M. Pickett. Spray g gasoline direct-injection: Spray mixing experiments and modeling. In *ECN4 Proceedings*. Engine Combustion Network, September 2015.

[38] Dong-Syau Jan, Horng-Yang Shiau, and Fuan-Nan Tsai. Vapor-liquid equilibria of n-hexane + cyclohexane + n-heptane and the three constituent binary systems at 101.0 kpa. *Journal of Chemical & Engineering Data*, 39(3):438–440, 1994.

[39] J. D. Jin and G. L. Borman. A model for multicomponent droplet vaporization at high ambient pressures. In *SAE Technical Paper*. SAE International, 02 1985.

[40] Gautam Kalghatgi, Leif Hildingsson, and Bengt Johansson. Low nox and low smoke operation of a diesel engine using gasolinelike fuels. *Journal of Engineering for Gas Turbines and Power*, 132(9):092803, 2010.

[41] Ghazi A Karim. The dual fuel engine. In *Automotive engine alternatives*, pages 83–104. Springer, 1987.

[42] Daisuke Kawano, Yuichi Goto, Matsuo Odaka, and Jiro Senda. Modeling atomization and vaporization processes of flash-boiling spray. In *SAE Technical Paper*. SAE International, 03 2004.

[43] Shuji Kimura, Osamu Aoki, Hiroshi Ogawa, Shigeo Muranaka, and Yoshiteru Enomoto. New combustion concept for ultra-clean and high-efficiency small di diesel engines. In *SAE Technical Paper*. SAE International, 10 1999.

[44] Robert Kiplimo, Eiji Tomita, Nobuyuki Kawahara, Shiyu Zhou, and Sumito Yokobe. Effects of injection pressure, timing and egr on combustion and emissions characteristics of diesel pcci engine. In *SAE Technical Paper*. SAE International, 08 2011.

[45] Janardhan Kodavasal, Yuanjiang Pei, Kevin Harms, Stephen Ciatti, Al Wagner, Peter Senecal, Marta Garca, and Sibendu Som. Global sensitivity analysis of a gasoline compression ignition engine simulation with multiple targets on an ibm blue gene/q supercomputer. In *SAE Technical Paper*. SAE International, 04 2016.

[46] S L Kokjohn, R M Hanson, D A Splitter, and R D Reitz. Fuel reactivity controlled compression ignition (rcci): a pathway to controlled high-efficiency clean combustion. *International Journal of Engine Research*, 12(3):209–226, 2011.

[47] Sanghoon Kook, Choongsik Bae, Paul C. Miles, Dae Choi, and Lyle M. Pickett. The influence of charge dilution and injection timing on low-temperature diesel combustion and emissions. In *SAE Technical Paper*. SAE International, 10 2005.

[48] Sanghoon Kook, Seik Park, and Choongsik Bae. Influence of early fuel injection timings on premixing and combustion in a diesel engine. *Energy & Fuels*, 22(1):331–337, 2007.

[49] K Kozuka, T Ozasa, T Fujikawa, and A Saito. Schlieren observation of spark-ignited premixed charge combustion phenomena using a transparent collimating cylinder engine. *Journal of engineering for gas turbines and power*, 125(1):336–343, 2003.

[50] Juncheng Li, Chia fon Lee, Zhiyu Han, Cai Shen, and Mianzhi Wang. A study on biodiesel nox emission control with the reduced chemical kinetics model. *Procedings of the ASME 2013 International Combustion Engine Division Fall Technical Conference*, (ICEF2013-19205), 2013.

[51] Menghan Li. private communication, 2016.

[52] Long Liang and Rolf D. Reitz. Spark ignition engine combustion modeling using a level set method with detailed chemistry. In *SAE Technical Paper*. SAE International, 04 2006.

[53] Long Liang, Rolf D. Reitz, Claudia O. Iyer, and Jianwen Yi. Modeling knock in spark-ignition engines using a g-equation combustion model incorporating detailed chemical kinetics. In *SAE Technical Paper*. SAE International, 04 2007.

[54] Long Liang, John G. Stevens, and John T. Farrell. A dynamic adaptive chemistry scheme for reactive flow computations. *Proceedings of the Combustion Institute*, 32(1):527 – 534, 2009.

[55] Yeong-Cheng Lien. *Bubble growth rates at reduced pressure.* PhD thesis, Massachusetts Institute of Technology, 1969.

[56] P.J. Linstrom and W.G. Mallard, editors. *NIST Chemistry WebBook*. Number 69 in NIST Standard Reference Database. National Institute of Standards and Technology, Gaithersburg MD, 20899.

[57] J.C. Livengood and P.C. Wu. Correlation of autoignition phenomena in internal combustion engines and rapid compression machines. *Symposium (International) on Combustion*, 5(1):347 – 356, 1955.

[58] T. Lu, Y. Ju, and C.K. Law. Complex csp for chemistry reduction and analysis. *Combustion and Flame*, 126(1-2):1445–1455, 2001. cited By (since 1996)98.

[59] Tianfeng Lu and Chung K. Law. A directed relation graph method for mechanism reduction. *Proceedings of the Combustion Institute*, 30(1):1333 – 1341, 2005.

[60] U. Maas and S.B. Pope. Simplifying chemical kinetics: Intrinsic low-dimensional manifolds in composition space. *Combustion and Flame*, 88(3-4):239–264, 1992.

[61] Marco Mehl, William J. Pitz, Charles K. Westbrook, and Henry J. Curran. Kinetic modeling of gasoline surrogate components and mixtures under engine conditions. *Proceedings of the Combustion Institute*, 33(1):193 – 200, 2011.

[62] Mohamad Metghalchi and James C. Keck. Burning velocities of mixtures of air with methanol, isooctane, and indolene at high pressure and temperature. *Combustion and Flame*, 48(0):191 – 210, 1982.

[63] Roy C Meyer, David P Meyers, Steven R King, and William E Liss. Effects of spark plug number and location in natural gas engines. *Journal of engineering for gas turbines and power*, 114(3):475–479, 1992.

[64] B.B Mikic, W.M Rohsenow, and P Griffith. On bubble growth rates. *International Journal of Heat and Mass Transfer*, 13(4):657 – 666, 1970.

[65] James W. Moore and Robert M. Wellek. Diffusion coefficients of n-heptane and n-decane in n-alkanes and n-alcohols at several temperatures. *Journal of Chemical & Engineering Data*, 19(2):136–140, 1974.

[66] PD Neufeld, AR Janzen, and RA Aziz. Use approximation to determine value for collision integral. *J. Chem. Phys*, 57:1100–1102, 1972.

[67] Karthik Nithyanandan. Diesel-like efficiency using cng/diesel dual-fuel combustion. In *ASME 2015 Internal Combustion Engine Division Fall Technical Conference*. American Society of Mechanical Engineers, 2015.

[68] Karthik Nithyanandan, Jiaxiang Zhang, and Yuqiang Li. private communication, 2015.

[69] Hiroshi Nomura, Yasushige Ujiie, Hans J. Rath, Jun'ich Sato, and Michikata Kono. Experimental study on high-pressure droplet evaporation using microgravity conditions. *Symposium (International) on Combustion*, 26(1):1267 – 1273, 1996.

[70] Krister Olsson and Bengt Johansson. Combustion chambers for natural gas si engines part 2: Combustion and emissions. In *SAE Technical Paper*. SAE International, 02 1995.

[71] Richard Opat, Youngchul Ra, Manuel A. Gonzalez D., Roger Krieger, Rolf D. Reitz, David E. Foster, Russell P. Durrett, and Robert M. Siewert. Investigation of mixing and temperature effects on hc/co emissions for highly dilute low temperature combustion in a light duty diesel engine. In *SAE Technical Paper*. SAE International, 04 2007.

[72] Peter J. O'Rourke and Anthony A. Amsden. The tab method for numerical calculation of spray droplet breakup. In *SAE Technical Paper*. SAE International, 11 1987.

[73] Amar Patel, Song-Charng Kong, and Rolf D. Reitz. Development and validation of a reduced reaction mechanism for hcci engine simulations, 03 2004.

[74] Ding-Yu Peng and Donald B Robinson. A new two-constant equation of state. *Industrial Engineering Chemistry Fundamentals*, 15(1):59–64, 1976.

[75] Federico Perini, Emanuele Galligani, and Rolf D. Reitz. An analytical jacobian approach to sparse reaction kinetics for computationally efficient combustion modeling with large reaction mechanisms. *Energy & Fuels*, 26(8):4804–4822, 2012.

[76] N. Peters. The turbulent burning velocity for large-scale and small-scale turbulence. *Journal of Fluid Mechanics*, 384:107–132, 1999.

[77] M. S. Plesset and S. A. Zwick. The growth of vapor bubbles in superheated liquids. *Journal of Applied Physics*, 25(4):493–500, 1954.

[78] B. Poling, J. Prausnitz, and J.O. Connell. *The Properties of Gases and Liquids*. McGraw Hill professional. McGraw-Hill Education, 2000.

[79] Youngchul Ra, Jeong Eui Yun, and Rolf D. Reitz. Numerical parametric study of diesel engine operation with gasoline. *Combustion Science and Technology*, 181(2):350–378, 2009.

[80] A.L. Randolph, A. Makino, and C.K. Law. Twenty-first symposuim (international on combustion) liquid-phase diffusional resistance in multicomponent droplet gasification. *Symposium (International) on Combustion*, 21(1):601 – 608, 1988.

[81] WE Ranz and WR Marshall. Evaporation from drops. *Chemical Engineering Progress*, 48(3):141446, 1952.

[82] H. H. Reamer, B. H. Sage, and W. N. Lacey. Phase equilibria in hydrocarbon systems. volumetric and phase behavior of the propane-carbon dioxide system. *Industrial & Engineering Chemistry*, 43(11):2515–2520, 1951.

[83] Rolf D. Reitz and R. Diwakar. Structure of high-pressure fuel sprays. In *SAE Technical Paper*. SAE International, 02 1987.

[84] Mohammad R. Riazi and Curtis H. Whitson. Estimating diffusion coefficients of dense fluids. *Industrial & Engineering Chemistry Research*, 32(12):3081–3088, 1993.

[85] M. F. Russell. Automotive diesel engine noise and its control. In *SAE Technical Paper*. SAE International, 02 1973.

[86] Y. Saad and M. Schultz. GMRES: A generalized minimal residual algorithm for solving nonsymmetric linear systems. *SIAM Journal on Scientific and Statistical Computing*, 7(3):856–869, 1986.

[87] S. Mani Sarathy, Stijn Vranckx, Kenji Yasunaga, Marco Mehl, Patrick Owald, Wayne K. Metcalfe, Charles K. Westbrook, William J. Pitz, Katharina Kohse-Hinghaus, Ravi X. Fernandes, and Henry J. Curran. A comprehensive chemical kinetic combustion model for the four butanol isomers. *Combustion and Flame*, 159(6):2028 – 2055, 2012.

[88] Shizuo Sasaki, Daisaku Sawada, Takanori Ueda, and Hiroyuki Sami. Effects of egr on direct injection gasoline engine. *JSAE Review*, 19(3):223 – 228, 1998.

[89] Mark Sellnau, Wayne Moore, James Sinnamon, Kevin Hoyer, Matthew Foster, and Harry Husted. Gdci multi-cylinder engine for high fuel efficiency and low emissions. *SAE Int. J. Engines*, 8:775–790, 04 2015.

[90] Mark C. Sellnau, James Sinnamon, Kevin Hoyer, and Harry Husted. Full-time gasoline direct-injection compression ignition (gdci) for high efficiency and low nox and pm. *SAE Int. J. Engines*, 5:300–314, 04 2012.

[91] Jiro Senda, Yoshiyuki Hojyo, and Hajime Fujimoto. Modeling on atomization and vaporization process in flash boiling spray. *JSAE Review*, 15(4):291 – 296, 1994.

[92] P.K Senecal, D.P Schmidt, I Nouar, C.J Rutland, R.D Reitz, and M.L Corradini. Modeling high-speed viscous liquid sheet atomization. *International Journal of Multiphase Flow*, 25(6-7):1073 – 1097, 1999.

[93] W. J. S. Smith, L. D. Durbin, and Riki Kobayashi. Thermal conductivity of light hydrocarbons and methane-propane mixtures at low pressures. *Journal of Chemical & Engineering Data*, 5(3):316–321, 1960.

[94] Mitchell D Smooke. Reduced kinetic mechanisms and asymptotic approximations for methane-air flames: a topical volume. In *Reduced Kinetic Mechanisms and Asymptotic Approximations for Methane-Air Flames*, volume 384, 1991.

[95] Hadeel Solaka, Martin Tuner, and Bengt Johansson. Analysis of surrogate fuels effect on ignition delay and low temperature reaction during partially premixed combustion. In *SAE Technical Paper*. SAE International, 04 2013.

[96] Y. Sun. *Diesel combustion optimization and emissions reduction using adaptive injection strategies (AIS) with improved numerical models*. University of Wisconsin–Madison, 2007.

[97] C.J. Sung, B. Li, H. Wang, and C.K. Law. Structure and sooting limits in counterflow methane/air and propane/air diffusion flames from 1 to 5 atmospheres. *Symposium (International) on Combustion*, 27(1):1523 – 1529, 1998. Twenty-Seventh Sysposium (International) on Combustion Volume One.

[98] Zhichao Tan and Rolf D. Reitz. Modeling ignition and combustion in spark-ignition engines using a level set method. In *SAE Technical Paper*. SAE International, 03 2003.

[99] Mario F Trujillo and F Lee Chia-fon. Modeling film dynamics in spray impingement. *Journal of fluids engineering*, 125(1):104–112, 2003.

[100] Sjoerd Van Stralen and Robert Cole. *Boiling phenomena: physicochemical and engineering fundamentals and applications*, volume 1. Hemisphere, 1979.

[101] N Ryan Walker, Flavio DF Chuahy, and Rolf D Reitz. Comparison of diesel pilot ignition (dpi) and reactivity controlled compression ignition (rcci) in a heavy-duty engine. In *ASME 2015 Internal Combustion Engine Division Fall Technical Conference*, pages V001T03A016–V001T03A016. American Society of Mechanical Engineers, 2015.

[102] Hu Wang, Mingfa Yao, and Rolf D. Reitz. Development of a reduced primary reference fuel mechanism for internal combustion engine combustion simulations. *Energy & Fuels*, 27(12):7843–7853, 2013.

[103] M. Wang and C. F. Lee. Compression-ignition combustion phase by a single fuel injection. Draft, 2017.

[104] Mianzhi Wang, Suya Gao, and Chia-Fon Lee. An efficient and unified combustion model for cfd of si and ci engine operation. In *SAE Technical Paper*. SAE International, 04 2017.

[105] Mianzhi Wang, Suya Gao, and Chia-fon F Lee. Computational investigation of combustion phasing and emissions for gdci engine operations. In *ASME 2017 Internal Combustion Engine Division Fall Technical Conference*. American Society of Mechanical Engineers, 2017.

[106] Mianzhi Wang and Chia-fon F Lee. Efficient computation methods for combustion reaction kinetics. In *ASME 2014 Internal Combustion Engine Division Fall Technical Conference*. American Society of Mechanical Engineers, 2014.

[107] Mianzhi Wang, Zhengxin Xu, Menghan Li, and Chia-Fon Lee. Numerical study and parameter optimization on a diesel - natural gas dual fuel engine. In *SAE Technical Paper*. SAE International, 04 2016.

[108] Mianzhi Wang, Zhengxin Xu, Saifei Zhang, and Chia-fon F Lee. Different diesel engine ignition regimes with a single injection. In *ASME 2015 Internal Combustion Engine Division Fall Technical Conference*. American Society of Mechanical Engineers, 2015.

[109] Russell A Whitesides, Matthew J McNenly, and Daniel L Flowers. Optimizing time integration of chemical-kinetic networks for speed and accuracy. *8th US Nat Combust Meet*, (070RK-0363), 2013.

[110] Jacob Williams. Bspline-fortran: Multidimensional b-spline interpolation of data on a regular grid. https://github.com/jacobwilliams/bspline-fortran, 2015-2016.

[111] Zhengxin Xu, Zhichao Zhao, Juncheng Li, Mianzhi Wang, Jingping Liu, Chia-Fon Lee, Wayne Chang, and Jie Hou. A reduced chemical kinetic mechanism of toluene reference fuel (toluene/n-heptane) for diesel engine combustion simulations. In *SAE Technical Paper*. SAE International, 04 2015.

[112] Junhao Yan, Karthik Nithyanandan, Timothy Lee, and Robert Donahue. High speed images of a hollow-cone pfi spray under flashing and non-flashing conditions. private communication, 2015.

[113] Jeng-Renn Yang and Shwin-Chung Wong. On the discrepancies between theoretical and experimental results for microgravity droplet evaporation. *International Journal of Heat and Mass Transfer*, 44(23):4433 – 4443, 2001.

[114] Yangbing Zeng. *MODELING OF MULTICOMPONENT FUEL VAPORIZATION IN INTERNAL COMBUSTION ENGINES*. PhD thesis, University of Illinois at Urbana-Champaign, 2000.

[115] Yangbing Zeng and Chia-fon Lee. Modeling of spray vaporization and air-fuel mixing in gasoline direct-injection engines. In *SAE Technical Paper*. SAE International, 03 2000.

[116] Yangbing Zeng and Chia-Fon Lee. Multicomponent-fuel film-vaporization model for multidimensional computations. *Journal of Propulsion and Power*, 16(6):964–973, 2000.

[117] Yangbing Zeng and Chia-fon Lee. An atomization model for flash boiling sprays. *Combustion Science and Technology*, 169(1):45–67, 2001.

[118] Yangbing Zeng and Chia-Fon Lee. A model for multicomponent spray vaporization in a high-pressure and high-temperature environment. *Journal of engineering for gas turbines and power*, 124(3):717–724, 2002.

Appendix A

Mixture Viscosity and Thermal Conductivity

The viscosity and thermal conductivity are calculated using the method developed by Chung *et al.* [14] and Chung *et al.* [13]. For a gaseous or condensed mixture of known compositions, the viscosity is estimated in the unit of micro-Poise ($1\ \mu\text{P} = 10^{-7}\ \text{Pa}\cdot\text{s}$):

$$\eta = \eta^* \frac{36.344(M_m T_{cm})^{1/2}}{V_{cm}^{2/3}}, \tag{A.1}$$

where M_m is the mean molecular weight (g/mol); T_{cm}, and V_{cm} are the mean critical temperature (K) and mean critical specific volume (cm^3/mol). The η^*:

$$\eta^* = \frac{\sqrt{T_m^*}}{\Omega_v}[F_c(G_2^{-1} + E_6 y)] + \eta^{**}, \tag{A.2}$$

$$\eta^{**} = E_7 y^2 G_2 \exp\left[E_8 + \frac{E_9}{T_m^*} + \frac{E_{10}}{T_m^{*\,2}}\right], \tag{A.3}$$

$$\begin{aligned}\Omega_v = {} & 1.16145 T_m^{*\,-0.14874} + 0.52487\exp(-0.77320 T_m^*) + 2.16178\exp(-2.43787 T_m^*) \\ & - 6.435\times 10^{-4} T_m^{*\,0.14874}\sin\left[(18.0323 T_m^{*\,-0.76830} - 7.27371)\frac{\pi}{180}\right],\end{aligned} \tag{A.4}$$

where:

$$y = \frac{\rho V_{cm}}{6}, \tag{A.5}$$

$$G_1 = \frac{1 - 0.5y}{(1-y)^3}, \tag{A.6}$$

$$G_2 = \frac{E_1[1-\exp(-E_4 y)]/y + E_2 G_1 \exp(E_5 y) + E_3 G_1}{E_1 E_4 + E_2 + E_3}, \tag{A.7}$$

and the ρ is the molar density (mol/cm^3) of the mixture. The constants E_is are evaluated by mean accentric factor ω_m, mean dipole moment μ_m (debye), and mean hydrogen bounding correction

Table A.1: Constants in Eq. A.8 for viscosity.

i	a_i	b_i	c_i	d_i
1	6.32402	50.4119	-51.6801	1189.02
2	1.2102e-3	-1.1536e-3	-6.2571e-3	0.037283
3	5.28346	254.209	-168.481	3898.27
4	6.62263	38.0957	-8.46414	31.4178
5	19.7454	7.63034	-14.3544	31.5267
6	-1.89992	-12.5367	4.98529	-18.1507
7	24.2745	3.44945	-11.2913	69.3466
8	0.79716	1.11764	0.012348	-4.11661
9	-0.23816	0.067695	-0.8163	4.02528
10	0.068629	0.34793	0.59256	-0.72663

factor κ_m:

$$E_i = a_i + b_i\omega_m + c_i{\mu_{rm}}^4 + d_i\kappa_m, \tag{A.8}$$

where the mean relative dipole moment:

$$\mu_{rm} = 131.3\frac{\mu_m}{\sqrt{V_{cm}T_{cm}}}, \tag{A.9}$$

and the constants a_is, b_is, c_is, and d_is are listed in Tab. A.1.

The mixing rules for the mean properties $(\cdot)_m$ is based on the molar fraction X_i:

$$V_{cm} = (\sigma_m/0.809)^3, \tag{A.10}$$

$$T_{cm} = 1.2593\frac{\epsilon_m}{k}, \tag{A.11}$$

$$M_m = \left[\frac{\sum_i\sum_j X_iX_j(\epsilon_{ij}/k)\sigma_{ij}^2\sqrt{M_{ij}}}{(\epsilon_m/k)\sigma_m^2}\right]^2, \tag{A.12}$$

$$\omega_m = \frac{\sum_i\sum_j X_iX_j\omega_{ij}\sigma_{ij}^3}{\sigma_m^3}, \tag{A.13}$$

$$\mu_m^4 = \sigma_m^3\sum_i\sum_j\frac{X_iX_j\mu_i^2\mu_j^2}{\sigma_{ij}^3}, \tag{A.14}$$

$$\kappa_m = \sum_i\sum_j X_iX_j\kappa_{ij}, \tag{A.15}$$

where,

$$\sigma_m^3 = \sum_i \sum_j X_i X_j \sigma_{ij}^3, \tag{A.16}$$

$$T_m^* = \frac{T}{\epsilon_m/k}, \tag{A.17}$$

$$\frac{\epsilon_m}{k} = \frac{\sum_i \sum_j X_i X_j (\epsilon_{ij}/k)\sigma_{ij}^3}{\sigma_m^3}, \tag{A.18}$$

and,

$$\sigma_{ii} = \sigma_i = 0809 V_{ci}^{1/3}, \tag{A.19}$$

$$\sigma_{ij} = \sqrt{\sigma_i \sigma_j}, \tag{A.20}$$

$$\frac{\epsilon_{ii}}{k} = \frac{\epsilon_i}{k} = \frac{T_{ci}}{1.2593}, \tag{A.21}$$

$$\frac{\epsilon_{ij}}{k} = \sqrt{\frac{\epsilon_i}{k}\frac{\epsilon_j}{k}}, \tag{A.22}$$

$$\omega_{ij} = \frac{\omega_i + \omega_j}{2}, \tag{A.23}$$

$$\kappa_{ij} = \sqrt{\kappa_i \kappa_j}, \tag{A.24}$$

$$M_{ij} = \frac{2 M_i M_j}{M_i + M_j}. \tag{A.25}$$

The thermal conductivity (W/m·K) of a mixture in condensed phase or gaseous phase:

$$\lambda = \frac{31.2 \eta^\circ \Psi}{0.001 M_m}(G_2^{-1} + B_6 y) + q B_7 y^2 T_r^{1/2} G_2, \tag{A.26}$$

where,

$$q = 3.586 \times 10^{-3} \sqrt{\frac{T_{cm}}{0.001 M_m}} V_{cm}^{-2/3}. \tag{A.27}$$

The y, G_1, and G_2 follow Eq. A.5 to A.8, with replacing the constants listed in Tab. A.1 with those in Tab. A.2. The η° is a reference viscosity (Pa $\cdot$ s) at the low pressure limit:

$$\eta^\circ = \frac{26.69 \times 10^{-7} F_{cm} \sqrt{M_m T}}{\sigma_m^2 \Omega_v}, \tag{A.28}$$

Table A.2: Constants in Eq. A.8 for thermal conductivity.

i	a_i	b_i	c_i	d_i
1	2.41657	7.4824e-1	-9.1858e-1	1.21721e2
2	-5.0924e-1	-1.50936	-4.99912e1	6.99834e1
3	6.61069	5.62073	6.47599e1	2.70389e1
4	1.45425e1	-8.91387	-5.63794	7.43435e1
5	7.9274e-1	8.2019e-1	-6.9369e-1	6.31734
6	-5.8634	1.28005e1	9.58926	-6.55292e1
7	9.1089e1	1.2811e2	-5.4217e1	5.2381e2

where,

$$F_{cm} = 1 - 0.2756\omega_m + 0.059035\mu_{rm}^4 + \kappa_m. \tag{A.29}$$

And the Ψ_v:

$$\Psi_v = 1 + \alpha \frac{0.215 + 0.28288\alpha - 1.061\beta + 0.26665Z}{0.6366 + \beta Z + 1.061\alpha\beta}, \tag{A.30}$$

where,

$$\alpha = \frac{C_{v,ig,m}}{R} - 1.5, \tag{A.31}$$

$$\beta = 0.7862 - 0.7109\omega_m + 1.3168\omega_m^2, \tag{A.32}$$

$$Z = 2 + 10.5\left(\frac{T}{T_{cm}}\right)^2. \tag{A.33}$$

The $C_{v,ig,m} = \sum_i X_i C_{v,ig,i}$ is the mean constant-volume ideal gas thermal capacity, and R is the ideal gas constant with the matching unit. Other mixing rules follow those for the viscosity.

Appendix B

Mixture-Averaged Diffusivity

Riazi and Whitson [84] proposed a method to estimate the mixture-averaged diffusivity using binary diffusivity model [35, 66]. At the low pressure limit, the product of molar density (mol/m^3) and mixture-averaged diffusivity (m^2/s) of a multi-component system:

$$(\rho D_{im})^\circ = \frac{0.0266\sqrt{T\frac{M_i^{-1}+M_m^{-1}}{2}}}{R\left(\frac{\sigma_i+\sigma_m}{2}\right)^2\Omega_{di}}, \tag{B.1}$$

where,

$$\Omega_{di} = \frac{1.06036}{T_i^{*0.15610}} + \frac{0.19300}{\exp(0.47635T_i^*)} + \frac{1.03587}{\exp(1.52996T_i^*)} + \frac{1.76474}{\exp(3.89411T_i^*)}, \tag{B.2}$$

$$T_i^* = \frac{T}{\sqrt{\frac{\epsilon_i}{k}\frac{\epsilon_m}{k}}}, \tag{B.3}$$

$$\frac{\epsilon_i}{k} = \frac{T_{ci}}{1.2593}, \quad \frac{\epsilon_m}{k} = \sum_i X_i\frac{\epsilon_m}{k}, \tag{B.4}$$

$$\sigma_i = 0.809V_{ci}^{1/3}, \quad \sigma_m = \sum_i X_i\sigma_i. \tag{B.5}$$

An empirical correction [21, 84] based on the reduced density of the mixture is used to estimate the mixture-averaged diffusivity of gaseous phase and condensed phase:

$$D_{im} = (1.0664 - 0.1228\rho_{ri} - 0.1118\rho_{ri}^2 + 0.01983\rho_{ri}^3)(\rho D_{im})^\circ V, \tag{B.6}$$

where,

$$\rho_{ri} = \frac{X_i V_{ci}^{5/3} + (1 - X_i) V_{cm}^{5/3}}{(X_i V_{ci}^{2/3} + (1 - X_i) V_{cm}^{2/3}) V}, \tag{B.7}$$

$$V_{cm} = \sum_i X_i V_{ci}. \tag{B.8}$$